

See discussions, stats, and author profiles for this publication at: <https://www.researchgate.net/publication/373768167>

# MESSENGER Reverse Engineering Analysis

Technical Report · June 2023

DOI: 10.13140/RG.2.2.12351.69289

---

CITATIONS  
0

READS  
191

---

6 authors, including:



Luca Sportelli  
Politecnico di Milano

7 PUBLICATIONS 0 CITATIONS

[SEE PROFILE](#)



Luigi Marchese  
Politecnico di Milano

6 PUBLICATIONS 0 CITATIONS

[SEE PROFILE](#)



Matteo Rossi  
Politecnico di Milano

6 PUBLICATIONS 0 CITATIONS

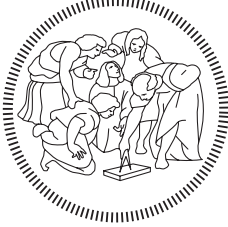
[SEE PROFILE](#)



Léo Bougault  
Politecnico di Milano

3 PUBLICATIONS 0 CITATIONS

[SEE PROFILE](#)



POLITECNICO DI MILANO

SPACE SYSTEM ENGINEERING AND OPERATIONS (A.Y. 2022/23)

TEAM 24

## MESSENGER Reverse Engineering Analysis

Bougault Léo	Marchese Luigi	Rossi Matteo	Sportelli Luca
10905813	10674110	10674801	10652027
219001	214724	214345	214389
Zito Giuseppe Antonio		Vacca Francesco	
	10641684		10707604
	215055		225181

June 2023

## Abstract

NASA's MESSENGER (Mercury Surface, Space ENvironment, GEochemistry, and Ranging) mission lasted from 2004 to 2015. MESSENGER follows the Mariner 10 mission, which flew in the '70s and managed to perform flybys of Mercury. Therefore, MESSENGER has been the first S/C to orbit the planet Mercury and its measurements allowed scientists to understand better how the terrestrial planets formed and evolved. Different features of the planet have been analyzed throughout the mission, such as the chemical composition, the global geological history and the magnetic field. The aim of this report is to perform a reverse engineering analysis of this mission in order to see how the selected design of the S/C addressed the problems that arose and to understand how the subsystems have been sized to achieve the goals.

## Index

List of figures	IV
List of tables	IV
List of symbols	V
List of acronyms	VI
<b>1 Mission Analysis</b>	<b>1</b>
1.1 Mission high-level goals . . . . .	1
1.2 Mission Drivers . . . . .	1
1.3 Functional Analysis . . . . .	2
1.4 Mission Phases & ConOps . . . . .	2
1.4.1 Mission Phases . . . . .	2

1.4.2	Concept of Operations . . . . .	3
1.5	On-board scientific instruments . . . . .	3
1.5.1	P/Ls overview . . . . .	3
1.5.2	Mission goals - P/Ls functions correlation . . . . .	4
1.5.3	P/Ls - ConOps/phases correlation . . . . .	5
1.6	Mission Analysis . . . . .	5
1.6.1	Trajectory Design . . . . .	5
1.6.1.1	Mission phases and trajectory . . . . .	5
1.6.1.2	Functionalities and Trajectory Design . . . . .	6
1.6.1.3	$\Delta V$ budget justification for each phases and retrieval . . . . .	7
<b>2</b>	<b>Propulsion Subsystem</b>	<b>9</b>
2.1	Introduction . . . . .	9
2.2	Propulsion Architecture . . . . .	9
2.2.1	Hydraulic schematic . . . . .	9
2.2.2	Tanks . . . . .	9
2.2.2.1	Main propellant tank . . . . .	10
2.2.2.2	Auxiliary tank . . . . .	10
2.2.2.3	Pressurant tank . . . . .	10
2.2.3	S/C adapter . . . . .	10
2.2.4	Thrusters . . . . .	10
2.2.4.1	Primary propulsion - orbital changes and corrections . . . . .	11
2.2.4.2	Secondary propulsion - SK and attitude . . . . .	11
2.3	Propulsion System Phases and ConOps . . . . .	12
2.3.1	Propulsion Maneuvers Breakdown . . . . .	12
2.4	Preliminary Sizing . . . . .	13
2.4.1	Propellant selection and masses . . . . .	13
2.4.2	Tanks sizing . . . . .	14
2.4.3	Pressurant gas selection and masses . . . . .	14
2.4.3.1	Pressure fed . . . . .	14
2.4.3.2	Blowdown . . . . .	15
2.4.4	Feeding lines selection . . . . .	15
<b>3</b>	<b>TTMTC Subsystem</b>	<b>16</b>
3.1	Introduction . . . . .	16
3.2	TTMTC architecture . . . . .	16
3.3	TTMTC subsystem design rationale . . . . .	17
3.3.1	Antennas selection, polarization and positioning . . . . .	17
3.3.2	Ground station selection . . . . .	17
3.3.3	TTMTC-OBDH interface . . . . .	18
3.3.4	Frequency and band selection . . . . .	18
3.4	TTMTC operations . . . . .	18
3.4.1	Transmission operations . . . . .	18
3.4.2	Transmission per mode . . . . .	19
3.4.3	Tracking operations . . . . .	19
3.5	Preliminary sizing . . . . .	19
3.5.1	Space segment . . . . .	19
3.5.2	Ground segment . . . . .	20
3.5.3	Losses . . . . .	20
3.5.4	Downlink results . . . . .	20
3.5.5	Uplink results . . . . .	21
<b>4</b>	<b>ADCS Subsystem</b>	<b>22</b>
4.1	Introduction . . . . .	22
4.2	ADCS architecture . . . . .	22
4.2.1	Attitude determination . . . . .	22
4.2.1.1	Sensors . . . . .	22
4.2.1.2	Attitude Determination Algorithm . . . . .	23
4.2.2	Attitude Control . . . . .	23
4.2.2.1	Actuators . . . . .	23

4.2.2.2	Attitude Control Algorithm . . . . .	24
4.3	Attitude control modes . . . . .	24
4.3.1	Pointing constraints . . . . .	24
4.3.2	Attitude pointing and control modes . . . . .	25
4.3.3	Pointing budget and performance parameters . . . . .	26
4.3.4	Transition between modes . . . . .	27
4.4	Preliminary sizing . . . . .	27
4.4.1	Perturbations . . . . .	27
4.4.2	Reaction wheels design . . . . .	27
4.4.3	Thrusters design . . . . .	28
<b>5</b>	<b>TCS Subsystem</b>	<b>30</b>
5.1	Introduction . . . . .	30
5.2	TCS Architecture . . . . .	30
5.2.1	Passive control . . . . .	30
5.2.1.1	Sunshade . . . . .	30
5.2.1.2	MLI and radiators . . . . .	30
5.2.1.3	Material and configuration solutions . . . . .	30
5.2.2	Active control . . . . .	31
5.2.2.1	Heaters . . . . .	31
5.2.2.2	Diode heat pipes . . . . .	31
5.2.2.3	Attitude control . . . . .	31
5.3	Thermal environment analysis per phase . . . . .	32
5.3.1	External heat fluxes . . . . .	32
5.3.2	Internal heat fluxes . . . . .	33
5.4	Components thermal control and temperature limits . . . . .	33
5.5	Preliminary sizing . . . . .	34
5.5.1	Mononodal analysis . . . . .	34
5.5.2	Multinodal analysis . . . . .	35
<b>6</b>	<b>EPS Subsystem</b>	<b>36</b>
6.1	Introduction . . . . .	36
6.2	EPS Architecture . . . . .	36
6.3	Power Budget . . . . .	38
6.4	Operational profiles and available sources . . . . .	38
6.5	Preliminary sizing . . . . .	40
6.5.1	Solar array sizing . . . . .	40
6.5.2	Battery sizing . . . . .	41
6.5.3	EPS mass, power and data budgets . . . . .	41
6.5.4	Positioning of components and pointing requirements . . . . .	41
<b>7</b>	<b>Configuration</b>	<b>43</b>
7.1	Introduction . . . . .	43
7.2	Vehicle shape and appendages distribution . . . . .	43
7.3	Configuration inside the fairing and launcher interface . . . . .	43
7.4	External configuration . . . . .	43
7.4.1	Propulsion Subsystem . . . . .	44
7.4.2	Tracking Telemetry & Telecommand Subsystem . . . . .	44
7.4.3	Electric Power Subsystem . . . . .	44
7.4.4	Thermal Control Subsystem . . . . .	44
7.4.5	Attitude Determination & Control Subsystem . . . . .	44
7.5	Internal configuration . . . . .	45
<b>8</b>	<b>On-Board Data Handling subsystem</b>	<b>46</b>
8.1	Introduction . . . . .	46
8.2	OBDH Architecture . . . . .	46
8.2.1	On-board computer and OBDH adopted bus . . . . .	46
8.2.2	Data handling strategy . . . . .	47
8.2.3	Data flow architecture . . . . .	48
8.3	OBDH reverse sizing . . . . .	48
8.3.1	OBC sizing . . . . .	48

## List of figures

1	Functional analysis.	2
2	Mission Conceptual Operations.	3
3	P/L location in the S/C [1].	4
4	DSM-1 Arc $\Delta V$ estimation and comparison.	8
5	Hydraulic schematic.	9
6	Tanks arrangement.	9
7	MPS thruster configuration.	11
8	MESSENGER S/C antennas location in body frame.	16
9	TTMTC architecture block diagram.	17
10	BER and $\frac{E_b}{N_0}$ with different encodings.	20
11	MESSENGER Guidance and Control Sensors.	23
12	MESSENGER Actuators.	24
13	Torque for the slew maneuver as a function of time required.	28
14	N. orbits to desaturate based on $c_s - c_g$ .	28
15	MESSENGER S/C with thermal control design highlights [2].	30
16	Solar panel temperatures as function of the tilt angle.	34
17	Overview of the Simulink model.	35
18	Nodes modelization in Simulink.	35
19	EPS architecture block diagram [3].	36
20	Solar panel power over voltage characteristic curve normalized at 28°C [3].	39
21	Battery SoC evolution during and after eclipse [4].	39
22	Available and requested power during the mission [4].	39
23	Limitations and operational zone of Sun offset angle with mission timeline [4].	39
24	Required area as a function of $\theta$ .	40
25	View of the S/C bottom deck, including the launch adapter ring.	43
26	S/C axes and sensors position.	45
27	IEM architecture and interfaces [5].	46
28	MESSENGER instrument data flow with corresponding mirrored CFDP and file storage [6].	48
29	Functions for every S/S.	48
30	Calculation of KIPS and words of memory needed by both analysed modes.	49

## List of tables

1	Guiding questions mapped into science objectives.	1
2	Mission goals correlated to the measurements of the P/Ls.	5
3	Phases/ConOps correlated to the P/Ls.	5
4	Sequence of flybys.	6
5	Functionalities and trajectory design correlation.	6
6	Scientific objectives correlated to the orbit design choices.	7
7	Justification and $\Delta V$ .	7
8	Comparison between real maneuvers and estimated ones.	8
9	Thrusters used to generate a needed force.	11
10	Thrusters used to generate a needed torque.	11
11	Maneuvers and Propulsion Modes during Operations.	13
12	Restriction in burn directions.	13
13	Propellant masses comparison.	13
14	Tanks properties.	14
15	Pressure fed pressurizing system parameters.	15
16	Blowdown pressurizing system parameters.	15
17	Data rates and data volumes per phase.	18
18	Space segment parameters for science downlink.	20
19	Ground segment parameters.	20
20	Losses.	20

21	TTMTC requirements . . . . .	21
22	Science Downlink Link Budget . . . . .	21
23	Uplink Link Budget . . . . .	21
24	Attitude constraints and effect on ADCS . . . . .	25
25	Pointing budget per mode and subsystem in Orbital phase . . . . .	26
26	Disturbances overview . . . . .	27
27	RW parameters . . . . .	28
28	Thruster sizing results . . . . .	29
29	Power budget as internal heat dissipation per phase . . . . .	33
30	Temperature limits and performances per component . . . . .	33
31	Heat sources in hot and cold case . . . . .	34
32	Parameters in hot case . . . . .	34
33	Parameters in cold case . . . . .	34
34	Results for both the hot and cold cases . . . . .	35
35	Power budget per phase in Watt [7] . . . . .	38
36	Results of preliminary solar array sizing . . . . .	40
37	Battery sizing results . . . . .	41
38	Refined battery sizing results . . . . .	41
39	RAD 6000 Specifications . . . . .	49
40	Reverse sizing results for both modes . . . . .	49
41	SSR reverse sizing . . . . .	49

## List of symbols

$\Delta V$	Delta velocity	$V_{tank}$	Tank volume
$d_{ox}$	Diameter of oxidizer feeding line	$D_{DSN}$	Deep Space Network Diameter
$d_f$	Diameter of fuel feeding line	$\frac{E_b}{N_0}$	Minimum Error per bit to Noise density
$g_0$	Acceleration of gravity on Earth	$\frac{E_b}{N_0 \min}$	Error per bit to Noise density
$h_{tank}$	Tank height	$EIRP_{half}$	Half array Effective Isotropical Radiated Power
$I_s$	Gravimetric specific impulse	$EIRP_{full}$	Full array Effective Isotropical Radiated Power
$m_{final}$	Spacecraft final mass	$\eta$	Efficiency coefficient
$m_{fuel}$	Fuel mass	$G$	Gain
$m_{initial}$	Spacecraft initial mass	$G_{tx}$	Transmission gain
$m_{oxidizer}$	Oxidizer mass	$\lambda$	Wavelength
$m_{press}$	Pressurizer mass	$L_{atm}$	Atmospheric losses
$m_{prop}$	Propellant mass	$L_{cable}$	Cable losses
$m_{tank}$	Tank mass	$L_{point}$	Misalignment losses
$P_{tank}$	Tank pressure	$L_{space}$	Space losses
$P_{press_{in}}$	Initial pressurizer pressure	$P_{in}$	Input power to the amplifier
$r_{tank}$	Tank radius	$P_{tx}$	Transmitted power
$t_{dome}$	Dome thickness	$P_{rx}$	Received power
$t_{cyl}$	Cylinder thickness	$SNR_{min}$	Minimum Signal to Noise Ratio
$V_{press}$	Pressurizer volume	$\theta$	Beamwidth
$V_{press_{in}}$	Initial pressurizer volume	$F_{desat}$	Force needed to desaturate
$V_{press_{fin}}$	Final pressurizer volume	$F_{slew}$	Force needed to perform the slew manoeuvre
		$h_{max}$	Maximum momentum storage of RW
		$m_{desat}$	Propellant mass needed to desaturate
		$m_{slew}$	Propellant mass needed for the slew

$m_{tot}$	Total propellant mass needed by ADCS system
$T_{aero}$	Torque due to aerodynamic drag
$T_{GG}$	Torque due to GG
$T_{magnetic}$	Torque due to magnetic fields
$T_{max}$	Maximum torque given by RW
$T_{SRP}$	Torque due to SRP
$\alpha$	Absorptivity
$\varepsilon$	Emissivity
$q_{sun}$	Solar flux
$q_{IR}$	Infrared flux
$q_{albedo}$	Albedo flux
$Q_{internal}$	Intern power consumption
$T_{S/C}$	Temperature of the S/C
$A_{radiators}$	Radiators area
$Q_{heaters}$	Heaters Power
$T_{sunshade}$	Temperature of the sunshade
$T_{arrays}$	Temperature of the solar arrays
$X_e$	Line efficiency in eclipse
$X_d$	Line efficiency in daylight
$\epsilon_{BOL}$	Efficiency in begin of light
$dpy$	Annual degradation
$I_D$	Inherent degradation factor
$P_{req}$	Power requested
$A_{SA}$	Area of solar array
$A_{SA_{real}}$	Real area of solar array according to papers
$m_{SA}$	Mass of solar array
$m_{SA_{real}}$	Real mass of solar array according to papers
$m_{batt}$	Mass of the battery
$C_{batt}$	Capacity of the battery
$V_{batt}$	Volume of the battery
$C_{batt_{refined}}$	Capacity of the battery with a refined sizing
$N_{series}$	Number of cells in series
$N_{parallel}$	Number of strings in parallel

## List of acronyms

<b>ADCS</b>	Attitude Determination and Control Subsystem
<b>AMD</b>	Autonomous momentum dump
<b>AU</b>	Astronomical Unit
<b>CMD</b>	Commanded momentum dump
<b>DLA</b>	Declination of Launch Asymptote
<b>DSM</b>	Deep Space Manoeuvre
<b>DSN</b>	Deep Space Network
<b>EPPS</b>	Energetic Particle and Plasma Spectrometer
<b>EPS</b>	Energetic Particle Spectrometer
<b>FIPS</b>	Fast Imaging Plasma Spectrometer
<b>GRNS</b>	Gamma-Ray and Neutron Spectrometer
<b>GRS</b>	Gamma-Ray Spectrometer
<b>LEOP</b>	Launch and Early Phase Operations
<b>MAG</b>	Magnetometer
<b>MASCS</b>	Mercury Atmospheric and Surface Composition Spectrometer
<b>MDIS</b>	Mercury Dual Imaging System
<b>MESSENGER</b>	Mercury Surface, Space ENvironment, GEochemistry, and Ranging
<b>MLA</b>	Mercury Laser Altimeter
<b>MOI</b>	Mercury Orbital Insertion
<b>MXU</b>	Mercury X-ray unit
<b>NAC</b>	Narrow Angle Camera
<b>OCM</b>	Orbital Correction Manoeuvre
<b>P/L</b>	Payload
<b>RS</b>	Radio Science
<b>S/C</b>	Spacecraft
<b>SRP</b>	Solar Radiation Pressure
<b>TCM</b>	Trajectory Correction Manoeuvre
<b>TCS</b>	Thermal Control Subsystem
<b>ToF</b>	Time of Flight
<b>UVVS</b>	UltraViolet Visible Spectrometer
<b>VIRS</b>	Visible Infrared Spectrometer
<b>WAC</b>	Wide Angle Camera
<b>XRS</b>	X-Ray Spectrometer
<b>ACS</b>	Attitude Control System

<b>AV</b>	Velocity Adjust	<b>GG</b>	Gravity Gradient
<b>CoM</b>	Center of Mass	<b>HEO</b>	Highly Elliptical Orbit
<b>LVA</b>	Large Velocity Adjust	<b>HPKO</b>	"Hot Pole" Keep-out
<b>MPS</b>	MESSENGER Propulsion Subsystem	<b>HRG</b>	Hemispherical resonance gyroscopes
<b>MR</b>	Mixture Ratio	<b>IMU</b>	Inertial Measurement Unit
<b>NEAR</b>	Near Earth Asteroid Rendezvous	<b>LH</b>	Local Horizontal
<b>NTO</b>	Nitrous Tetroxide	<b>MP</b>	Main Processor
<b>O/F</b>	Oxidizer to Fuel ratio	<b>PID</b>	Proportional–Integral–Derivative
<b>PMD</b>	Propellant Management Device	<b>SADA</b>	Solar Array Drive Mechanism
<b>STA</b>	Solution-Treated and Aged	<b>SKI</b>	Sun Keep-In
<b>TVC</b>	Thrust Vector Control	<b>SkiBox</b>	An end-to-end automated science planning and commanding system
<b>BER</b>	Bit Error Rate	<b>S-SIRU</b>	Scalable Space Inertial Reference Unit
<b>EIRP</b>	Effective Isotropically Radiated Power	<b>TCM</b>	Trajectory Correction Maneuver
<b>GS</b>	Ground Station	<b>EPS</b>	Electric Power Subsystem
<b>HGA</b>	High Gain Antenna	<b>IR</b>	Infrared
<b>ITU</b>	International Telecommunication Union	<b>IBS</b>	In-Bound Season
<b>LGA</b>	Low-Gain Antenna	<b>MLI</b>	Multi-Layer Insulation
<b>MGA</b>	Medium-Gain antenna	<b>OSR</b>	Optical Solar Reflectors
<b>OBDH</b>	On Board Data Handling	<b>PC</b>	Printed Circuit
<b>PAA</b>	Phased-Array Antenna	<b>PDU</b>	Power Distribution Unit
<b>QPSK</b>	Quadrature Phase Shift Keying	<b>PSE</b>	Power System Electronics
<b>RF</b>	Radio Frequency	<b>SAJB</b>	Solar Array Junction Box
<b>SDST</b>	Small Deep Space Transponders	<b>S/S</b>	Subsystem
<b>SNR</b>	Signal to Noise Ratio	<b>AOCS</b>	Altitude and Orbit Control Subsystem
<b>SSPA</b>	Solid-State Power Amplifiers	<b>BOL</b>	Beginning-Of-Life
<b>TTMTC</b>	Tracking Telemetry and Telecommand Subsystem	<b>C</b>	Charge
<b>AKE</b>	Absolute Knowledge Error	<b>C/D</b>	Charge-to-Discharge
<b>APE</b>	Absolute Performance Error	<b>CMG</b>	Curb Mount Glass
<b>BRV</b>	Body Roll Vector	<b>CPV</b>	Common Pressure Vessel
<b>DSS</b>	Digital Sun Sensors	<b>DOD</b>	Depth-of-Discharge
<b>DSSE</b>	Digital Sun Sensor Electronics	<b>EOL</b>	End-Of-Life
<b>DSSH</b>	Digital Sun Sensor Heads	<b>GaAs</b>	Gallium arsenide
<b>ERRV</b>	External Roll Reference Vector	<b>IEM</b>	Integrated Electronic Module
<b>FOV</b>	Field Of View	<b>MOSFET</b>	Metal Oxide Semiconductor Field Effect Transistor
<b>FPA</b>	Front Phased Array Antennas	<b>Ni-H2</b>	Nickel–Hydrogen
<b>G&amp;C</b>	Guidance and Control	<b>PPT</b>	Peak Power Tracking
		<b>PS</b>	Propulsion Subsystem

**S/A** Solar Array

**SoC** State-of-Charge

**TIMED** Thermosphere Ionosphere Mesosphere Energetics  
and Dynamics

**V/T** Temperature-compensated Voltage

**BC** Bus Controller

**BM** Bus Monitor

**CCSDS** Consultative Committee for Space Data Systems

**CFDP** CCSDS File Delivery Protocol

**CM** Center of Mass

**CTE** Coefficient of Thermal Expansion

**DH** Data Handling

**DC** Direct Current

**DCB** Data Collection Buffer

**DPU** Data Processing Unit

**EEPROM** Electrically Erasable Programmable Read-  
Only Memory

**FPP** Fault Protection Processor

**FTP** File Transfer Protocol

**HK** Housekeeping

**KIPS** Kilo-instructions Per Second

**Mb** Megabyte

**OBC** On-Board Computer

**OBSW** On-Board Software

**OCXO** Oven-Controlled Crystal Oscillator

**PCI** Peripheral Component Interconnect

**RAM** Random-Access Memory

**ROM** Read Only Memory

**RT** Remote Terminal

**RW** Reaction wheels

**SDRAM** Synchronous Dynamic Random-Access Memory

**SSR** Solid State Recorders

# 1 Mission Analysis

## 1.1 Mission high-level goals

Being the MESSENGER the first Mercury orbiter, the high-level goals are many and diversified. This mission was designed to address six key scientific questions that represent the major scientific goals. The latter are then translated into measurement objectives to be accomplished by the S/C. In Table 1, the guiding questions are mapped into science objectives.

Guiding Questions	Science Objectives
What planetary formation processes led to Mercury's high ratio of metal to silicate?	Map the elemental mineralogical composition of Mercury's surface
What is the geological history of Mercury?	Image globally the surface
What are the nature and the origin of Mercury's magnetic field?	Determine the structure of the planet's magnetic field
What are the structure and the state of Mercury's core?	Measure the libration amplitude and gravitational field structure
What are the radar-reflective materials at Mercury's poles?	Determine the composition of the radar-reflective materials at Mercury's poles
What are the important volatile species and their sources and sinks on and near Mercury?	Characterize exosphere neutrals and accelerated magnetosphere ions

**Table 1:** Guiding questions mapped into science objectives.

In section 1.5.2, it can be seen how the science goals will be accomplished by one or more of the P/Ls.

## 1.2 Mission Drivers

The drivers of a mission are critical requirements that lead completely or partly the design process of one or more subsystems. For the MESSENGER mission, the following drivers have been recognized:

### 1. Surviving in the harsh environment at Mercury

The MESSENGER orbited Mercury, the closest planet to the Sun. The direct solar intensity is nearly 11 times the one felt at 1 AU and the heat reflected off the planet is 4 times that at Earth. It has been thought that the TCS was the most critical subsystem. As a matter of fact, the physical layout of the MESSENGER was dominated by the large ceramic cloth sunshade. The sunward side routinely experienced temperatures in excess of 300°C, while the elements harbored behind it operated at approximately room temperature. The Mission Analysis and the ADCS have been considered the most affected. As a matter of fact, all S/C operations are constrained by the fact that the body of the S/C must be protected from the Sun to avoid overheating, therefore the sun-shield shall always point towards the Sun.

### 2. Achieving orbit around Mercury

One of the main difficulties for an interplanetary transfer towards the inner part of the solar system is the complexity of lowering the energy to get to a planet. Since Mercury is the innermost planet, the S/C velocity would grow significantly throughout the trajectory, thus performing an orbital insertion would be too expensive. As a consequence, an intricate trajectory had been designed, which required a lightweight vehicle with a substantial amount of propellant to provide the necessary propulsive  $\Delta V$ . In order to save mass, a composite structure was chosen over a less expensive conventional aluminum design. The use of the ceramic-cloth sunshade avoided the need for a heavy, complex, active cooling system. A novel high-gain antenna was used to obviate the need for a heavy gimbaled parabolic dish. The trajectory, flybys and maneuvers leading to an acceptable  $\Delta V$  budget will be deeply analyzed in section 1.6.1.

### 3. Returning all collected science data to Earth

Mission success also required collecting and safely transmitting back to Earth the science data. MESSENGER used X-band antennas, communicating through the Deep Space Network ground stations. A novel electronically steerable phased-array antenna was used for high-gain downlink to Earth. The antenna had no moving parts and was capable of operating in the extreme temperature and radiation of direct sunlight on the front of the vehicle's sunshade. Furthermore, a simple and robust strategy was developed to ensure vehicle safety in case of onboard faults. Faults were classified as recoverable, serious or critical. Recoverable faults were addressed autonomously by the S/C allowing uninterrupted data collection. Serious faults caused the interruption of science operations by establishing an Earth communication configuration in order to allow a speedy fault diagnosis and recovery by ground operators. This mode was called *safe-hold mode*. Critical faults were addressed by relying only on a very onboard robust system to ensure safety while the S/C slowly reestablished a communication link to Earth. The name of this mode was *Earth-acquisition mode*[1]. This self-preservation was crucial to ensure the S/C's survival because communication delays with the ground

station coupled with S/C's vicinity to the Sun could lead to overheating of components before ground operators could even know that there was a problem.

### 1.3 Functional Analysis

In Figure 1, the functional analysis of the mission is shown.

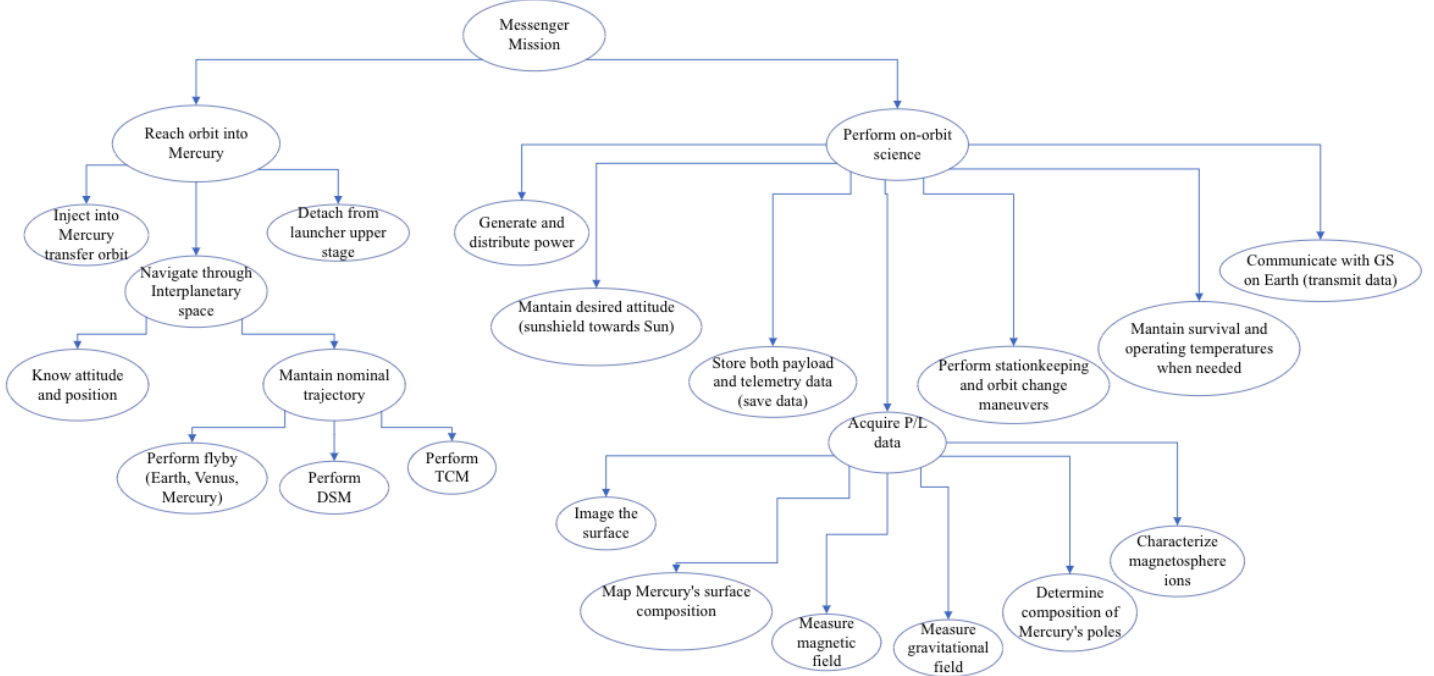


**Figure 1:** Functional analysis.

### 1.4 Mission Phases & ConOps

#### 1.4.1 Mission Phases

The MESSENGER mission was divided into four main phases: LEOP, Cruise Phase, Orbit Phase and Disposal.

**LEOP:** The launch took place on August 3, 2004. The S/C exited the eclipse after more than 20 minutes with its solar panels in their stowed positions. The solar panels were deployed 37 minutes later after the S/C separated from the third stage. The S/C separated from the upper stage after the first telemetry was received from the DSN. The main steps of this phase were the separation of the S/C, the deployment of the solar panels and the detumbling phase.

**Cruise Phase:** At the beginning of this phase, the S/C was injected in an interplanetary trajectory with the aim of reaching Mercury. The cruise had a duration of six years and eight months during which several flybys were performed. All maneuvers will be better described in section 1.6.1.1. The cruise phase included also instrument testing, calibration and verification to ensure the scientific instruments were functioning properly and ready for use during the mission. In addition, the maneuver called flip-flop was executed. It consisted in pointing the sunshade toward the Sun as the S/C approached the inner solar system and in pointing the S/C's unprotected side squarely toward the Sun in order to offer appropriate warmth at lower power levels while farther away [8].

**Orbit Phase:** A large Mercury orbit-insertion maneuver in 2011 marked the transition from the "cruise phase" to the "orbit phase" of the mission, which consisted in mapping the planet's surface and studying its atmosphere, geology and magnetic field by exploiting all P/Ls. This activity was performed in a store-and-forward manner. Typically each 24-hour period (two orbits) was composed of a 16-hour data collection period followed by an 8-hour data downlink period [9]. Although the mission was designated to last for one year, it was extended twice.

**Disposal:** In the final phase of the mission, the S/C performed a series of low orbits in order to collect the latest scientific data. The end of the mission consisted of an orbit decay and a controlled crash of the S/C on the Mercury's surface on April 30, 2015. Planetary protection guidelines[10] suggest avoiding the impact of the S/C on the planet's surface to prevent possible organic contamination. Nevertheless, it must be noted that Mercury is in Category I, in fact, this planet is not of direct interest for chemical evolution or the origin of life. Therefore, no planetary protection is required.

### 1.4.2 Concept of Operations

The mission conceptual operations are summarized in Figure 2. Orbital, Flip-Flop, correction maneuvers and all communications were not continuous operations, therefore Figure 2 shows the period in which they could have been carried out.

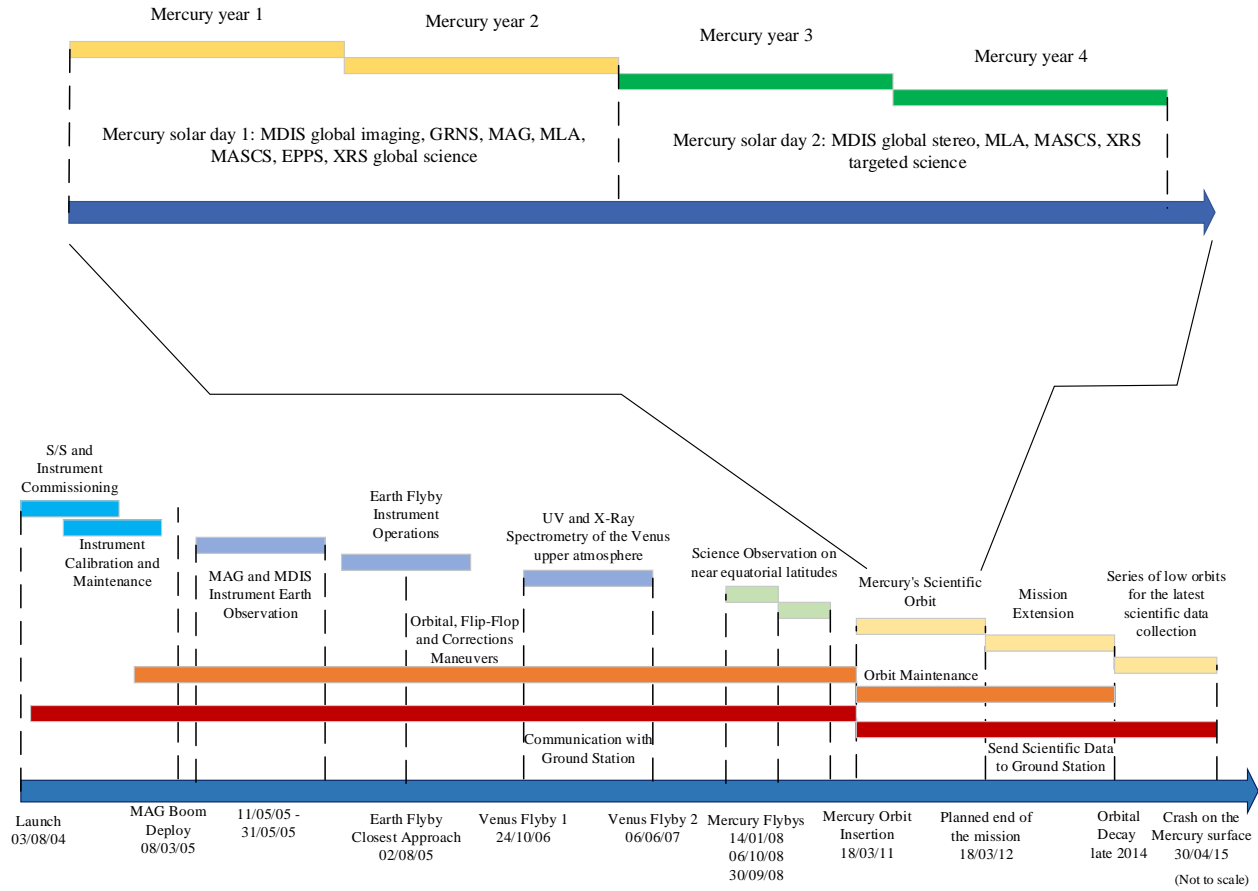


Figure 2: Mission Conceptual Operations.

## 1.5 On-board scientific instruments

### 1.5.1 P/Ls overview

With the aim of fulfilling the mission goals, the MESSENGER was equipped with seven scientific instruments and a Radio Science (RS). the total mass of those instruments, taking into account mounting hardware and captive thermal control components, was 47.2 kg [11].

**Mercury Dual Imaging System (MDIS):** It included both a wide-angle camera (WAC), which had a 10.5° field of view, and a narrow-angle camera (NAC) with a 1.5° field of view. The WAC and NAC were mounted on opposite sides of a pivoting platform to provide for optical navigation and planetary mapping during the Mercury flybys. It returned stereo imaging for high-resolution topography.

**Gamma-Ray and Neutron Spectrometer (GRNS):** It included two sensors, a Gamma-Ray Spectrometer (GRS) and a Neutron Spectrometer (NS). The GRS was a cryocooled, high-purity germanium detector with an active shield and measured abundances of O, Si, S, Fe, H, K, Th and U. The GRNS could also detect low-energy neutrons produced by cosmic ray bombardment and moderated by collisions with hydrogen-rich material. This instrument allowed the production of global compositional maps and the characterization of the chemical composition and geologic history of Mercury, other than the determination of the volatile inventory at the poles.

**X-Ray Spectrometer (XRS):** The planet-viewing portion of the instrument, which was the Mercury X-ray Unit (MXU), was mounted on the lower S/C deck, whereas the Sun-viewing portion was mounted on the S/C sunshade. The detectors covered the energy range from 1 to 10 keV. This instrument helped answer questions about the nature and composition of Mercury's crust, tectonic history, the structure of the atmosphere and magnetosphere, and the nature of the polar caps by measuring X-Ray emissions induced by the incident solar flux.

**Magnetometer (MAG):** It was a three-axis, ring-core, fluxgate magnetometer. The MAG sensor head was located on a lightweight, 3.6 m carbon-fiber boom extending in the anti-sunward direction to avoid disturbances with the onboard electronics. The sensor had its own sunshade because it could protrude from the shadow of the S/C when the pointing was close to the allowable off-Sun limits. This P/L measured the magnetic field of Mercury and helped in determining both its origin and its structure.

**Mercury Laser Altimeter (MLA):** It included a laser transmitter operating at 1,064 nm wavelength and four receiver telescopes. MLA was mounted on the S/C lower deck. MLA operated for about 30 minutes around the periapsis of each orbit because of MESSENGER's elliptical orbit at Mercury. It helped to retrieve the distance from the surface to the planet's center of mass. It also contributed to characterizing Mercury's geologic history and the size of the core, other than getting pieces of information on Mercury's global shape, spin axis, and libration.

**Mercury Atmospheric and Surface Composition Spectrometer (MASCS):** A moving-grating Ultraviolet-Visible Spectrometer (UVVS) observed emissions from the Mercury exosphere during limb scans, while a Visible-Infrared Spectrograph (VIRS) observed the planetary surface. The instrument was mounted on the lower S/C deck. It has been useful to characterize the composition of the surface, the geologic history, and the nature of the exosphere.

**Energetic Particle and Plasma Spectrometer (EPPS):** It consisted of an Energetic Particle Spectrometer (EPS) and a Fast Imaging Plasma Spectrometer (FIPS). EPS was mounted on the rear deck of the S/C, whereas FIPS was located on the side of the S/C. This instrument studied the exosphere and magnetosphere of Mercury, measuring ions from about 10 keV to 5 MeV and electrons from about 20 to 700 keV.

**Radio Science (RS):** The radio frequency (RF) telecommunications system has been used to conduct radio science as well as communicate with the MESSENGER. Using the S/C's positioning and velocity data, this device contributed to determining Mercury's gravitational field, providing improvements to the planet's orbital ephemeris and sharpening knowledge of the planet's rotation state, including obliquity and forced physical libration.

In Figure 3, the placement of the P/Ls can be appreciated.

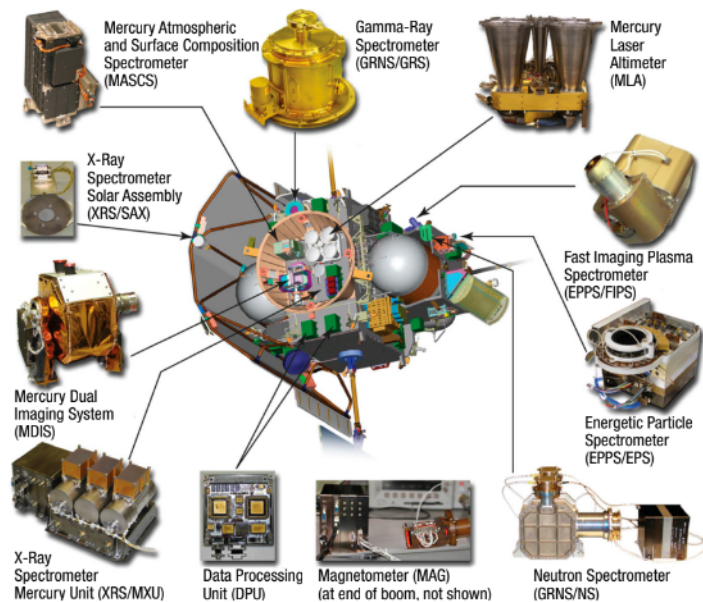


**Figure 3:** P/L location in the S/C [1].

### 1.5.2 Mission goals - P/Ls functions correlation

The questions in Table 1 have been answered by the observations and measurements from two or more P/Ls. Furthermore, the observations from each instrument addressed multiple questions, as shown in Table 2.

Science Objectives	Measurement Objectives
Map the elemental and mineralogical composition of Mercury's surface	Surface element abundances: GRNS and XRS Spectral measurements of surface: MASCS
Image globally the surface at a resolution of hundreds of meters or better	Global imaging in color: MDIS Targeted high-resolution imaging: MDIS Global stereo: MDIS Spectral measurements of geological units: MASCS Northern hemisphere topography: MLA
Determine the structure of the planet's magnetic field	Mapping of the internal field : MAG Magnetospheric structure: MAG, EPPS
Measure the libration amplitude and gravitational field structure	Gravity field, global topography, obliquity, libration amplitude: MLA, RS
Determine the composition of the radar-reflective materials at Mercury's poles	Composition of polar deposits: GRNS Polar exosphere: MASCS Polar ionized species: EPPS Altimetry of polar craters: MLA
Characterize exosphere neutrals and accelerated magnetosphere ions	Neutral species in exosphere: MASCS Ionized species in magnetosphere: EPPS Solar wind pick-up ions: EPPS Elemental abundances of surface sources: GRNS, XRS

**Table 2:** Mission goals correlated to the measurements of the P/Ls.

### 1.5.3 P/Ls - ConOps/phases correlation

A high-level correlation between P/Ls and phases/ConOps is outlined in Table 3.

Phase/ConOps	Payload
LEOP	Instrument digital powered unit, MAG and GRNS powered; all the subsystems were tested one and a half months after the launch; a special test of GRNS (full cooldown) was carried out
After first flip / before Earth flyby	Deployment of the MAG
Earth Flyby	Testing of MLA; MDIS shot images of Earth and Moon; MASCS realized lunar and Earth hydrogen corona observation; several flip/flops for selected instrument operations
First Venus flyby	No payload usage due to solar conjunction
Second Venus flyby	All instruments used to be prepared for the following Mercury encounter, in particular Ultraviolet and X-Ray spectrometries of upper atmosphere were recorded
Mercury flybys	Science observation on near equatorial latitudes at altitudes not reached during the orbital phase
First Mercury solar day	MDIS global imaging, GRNS, MAG, MLA, MASCS, EPPS, XRS global science
Second Mercury solar day	MDIS global stereo, MLA, MASCS, XRS targeted science

**Table 3:** Phases/ConOps correlated to the P/Ls.

## 1.6 Mission Analysis

### 1.6.1 Trajectory Design

In this section, the S/C trajectory will be correlated to the mission phases and to the functionalities outlined in section 1.3. Justification and retrieval of maneuver cost in terms of  $\Delta V$  per each phase of the mission will be provided.

#### 1.6.1.1 Mission phases and trajectory

Each phase described in section 1.4.1 is characterized by multiple trajectory features and maneuvers in order to satisfy all the mission's goals. The designed trajectory can be subdivided according to the mission phases in the following way [12].

**LEOP:** Launched 3 August 2004 aboard a Delta II 7925H from Cape Canaveral Air Force Station, with departure from Earth orbit with  $16.388 \text{ km}^2/\text{s}^2$  launch energy at a  $-32.66^\circ$  declination of launch asymptote (DLA) relative to the Earth mean equator at the standard J2000 epoch. The launch date was the third and last opportunity of 2004, because of delays in the availability of the launch facility, leading to a longer Cruise Phase duration with a similar total  $\Delta V$ .

**Cruise Phase:** Interplanetary transfer duration of 6 years and 8 months, comprehensive of six gravity-assist fly-bys (one on Earth, two on Venus and three on Mercury) and five DSMs for planet phasing. On 18 March 2011, Mercury Orbit Insertion (MOI) maneuver was performed during the fourth Mercury encounter. Flyby sequence is shown in Table 4.

Orbital Event	Date	Trajectory Design
Earth fly-by	2 August 2005	Perihelion lowered to 0.6 AU, argument of perihelion moved 60° closer to the one of Mercury.
Venus fly-by 1	24 October 2006	Inclination increased to 7.9° and orbital period reduced to have a second flyby exactly after one revolution of Venus, e.g. 1:1 Venus-S/C resonance.
Venus fly-by 2	6 June 2007	Aphelion lowered and perihelion lowered to allow Mercury fly-by.
Mercury fly-by 1	14 January 2008	Orbit shape rotated and changed in order to make it similar to Mercury's one. Mercury-S/C resonance 2:3 obtained.
Mercury fly-by 2	6 October 2008	Orbit shape rotated and changed in order to make it similar to Mercury's one. Mercury-S/C resonance 3:4 obtained.
Mercury fly-by 3	30 September 2009	Rotation and change in orbit shape towards Mercury's one completed. Mercury-S/C resonance 5:6 was obtained, enabling a feasible MOI.

**Table 4:** Sequence of flybys.

**Orbit phase:** The scientific orbit had an 80° ( $\pm 2^\circ$ ) inclination relative to Mercury's equator, 200 km ( $\pm 25$  km) periapsis altitude, 12 h ( $\pm 1$  min) orbit period, 118.4° argument of periapsis (60°N periapsis latitude, with 56°N-62°N acceptable), and a 348° (169–354 deg) longitude of ascending node. A pair of Orbital Correction Maneuvers (OCMs) approximately every 88 days returned the perturbed orbit to the initial parameters. The mission was extended two times, and the last OCM was performed on 21 January 2015.

**Disposal:** Orbit decay due to perturbations (Solar pressure, variations in Mercury's gravity, solar gravity, end-of-life sunshade surface reflectance and Mercury surface albedo) after complete depletion of propellant, continuing the scientific phase until it crashed on Mercury. The impact was close to 54.4° N latitude and 149.9° W longitude.

#### 1.6.1.2 Functionalities and Trajectory Design

The functionalities having an impact on trajectory design and the orbital conditions influencing the system functionalities [12] [13] are analyzed in Table 5.

S/C Functionality	Correlated trajectory design feature
The necessity of a robust thermal protection system, including a ceramic cloth sunshade	Minimum distance from the Sun of 0.31 AU to reach and orbit Mercury.
Determination of Solar Panels tilting angle for Solar Radiation Pressure computation to control S/C attitude	Due to 0.31 AU distance from the Sun, the significant perturbing contribution of SRP
Battery capacity for power availability during eclipses	Consideration of maximum eclipse duration in choice of scientific orbit periapsis latitude
Ability to communicate and receive commands from the ground	Solar Conjunctions events are an obstacle to communications: no maneuvers are planned during these periods
Sunshade pointing for thermal control	Thrusters pointing to perform OCMs: maneuver execution limited to twice every 88 days
Highly accurate orbit knowledge for precise scientific data acquisition	Maximization of time between OCMs to once every 88 days to avoid introducing uncertainty into orbit determination

**Table 5:** Functionalities and trajectory design correlation.

In Table 6, the scientific objectives of the mission are mapped into Mercury orbit design [13].

Mission Objectives	Mission Design requirements	Orbit design
Surface imaging at 250 m resolution	Provide two Mercury solar days for stereo-imaging of the entire surface, near-polar orbit for full coverage	Orbital phase lasting one Earth year (longer than two Mercury days), periapsis altitude 200-500 km, 80° inclination
1. Mercury magnetic field structure determination 2. Simplify operations 3. Map surface composition	1. Minimize periapsis and maximize altitude-range coverage 2. Orbital period of 24, 12 or 8 hours 3. Maximize time at low altitudes	Periapsis altitude 200-500 km. Apoapsis altitude 15200 km for 12 hours orbital period
1. Libration amplitude and gravitational field structure 2. Composition of radar-reflective materials at the poles	1. Minimize thrusting events 2. Inclination of 80°, latitude of periapsis 60°N	Inclination drift from 80° to 82°, periapsis latitude from 60°N to 72°N, two OCMs every 88 days (30 hours apart)
Exosphere neutrals and accelerated magnetosphere ions characterization	Coverage of magnetosphere, which includes: bow shock, magnetopause and upstream solar wind	Wide altitude conditions and visibility under different lighting conditions

**Table 6:** Scientific objectives correlated to the orbit design choices.

#### 1.6.1.3 $\Delta V$ budget justification for each phases and retrieval

Justification and cost of each maneuver are outlined in Table 7 according to three different  $\Delta V$  budgets:

- The **allocated  $\Delta V$**  budget [12] in design phase;
- The  **$\Delta V$  budget reallocated** during operations [13] at 35% completed heliocentric transfer;
- The  **$\Delta V$  budget actually performed** [14] during execution of maneuvers;

Maneuver	Justification	$\Delta V$ allocated [m/s]	$\Delta V$ reallocated at 35% [m/s]	$\Delta V$ executed [m/s]
DSMs	DSM-1 for Earth–Venus phasing and DSM-2 for Venus–Mercury phasing. DSM-3-4-5 for moving the successive Mercury encounter closer to Mercury’s location at MOI.	1008	1032	1040
Launch Vehicle and navigation errors (99%)	The totality of TCMs includes correcting launcher dispersion, fly-by B-plane targeting and 20-30 statistical TCMs for navigation errors. Commanded momentum dumps, mass adjustment and autonomous momentum dumps are included.	121	115	69.5
MOI	Decrease in relative velocity with respect to Mercury with an apse line rotation to end at 60°N periapsis latitude (MOI 1), and adjustment of orbital parameters by periapsis burn (MOI 2).	867	862	861.7
OCMs	Two OCMs will return the S/C to the initial primary science orbit’s size and shape approximately every 88 days. OCM 1 is performed to transfer orbit to adjust apoapsis altitude, OCM 2 to adjust periapsis altitude and orbital period at 12 h.	85	84	83.1 (242.1 after mission extension)
Contingency		169	136	
Total		2250	2229	2054.3 (2213.3 after mission extension)

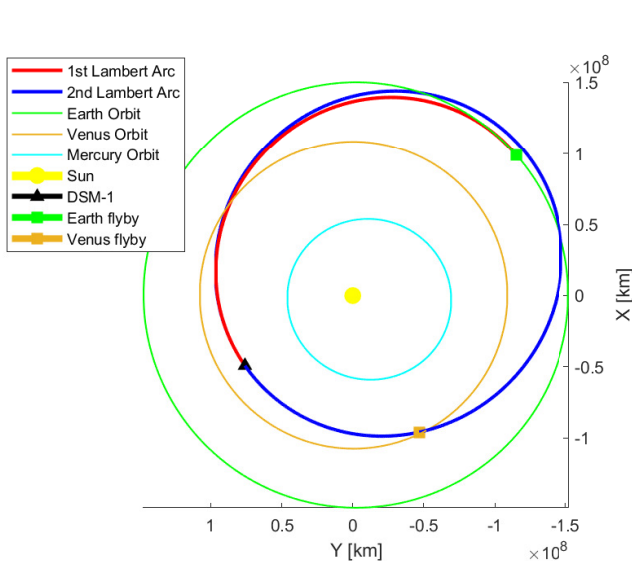
**Table 7:** Justification and  $\Delta V$ .

The allocated  $\Delta V$  in the design phase does not include maneuvers from OCM 6 up to the last OCM 18, which were executed during the extension period of the mission [14]. The reallocation of the budget with the 21 m/s reduction in total  $\Delta V$

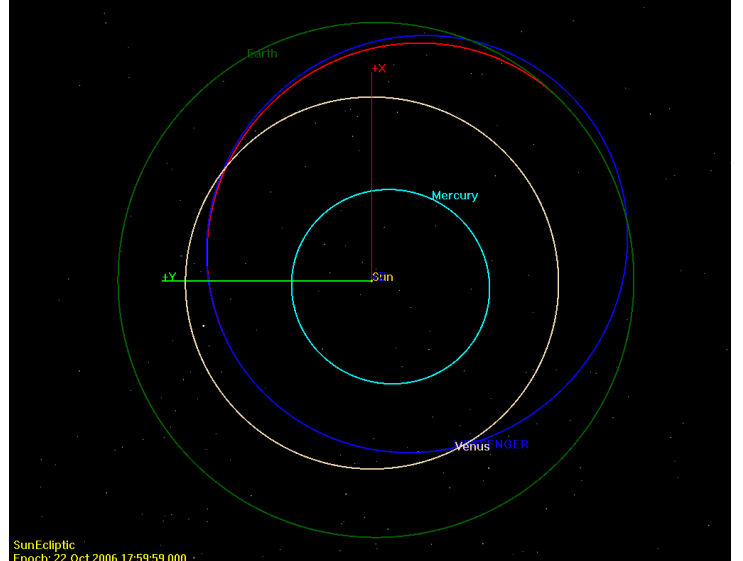
capability since launch is attributable to increases in corrections after the first Venus flyby, propulsion system performance updates, and a six-day shift in DSM-2. Particularly for the latter, placement of DSM-2 7.5 days before solar conjunction entry provided an opportunity for recovery from either delays or errors other than limiting direct sunlight exposure on the LVA thruster [15]. As it can be noted in Table 7, the deterministic maneuvers don't have any additional margin apart from the Contingency  $\Delta V$ , which corresponds to around 8 % of the sum. The launch vehicle and navigation error section contain mainly stochastic maneuvers (with exception of two deterministic small TCMs) being the 99th percentile value derived from Monte Carlo Analysis. The residual  $\Delta V$  is spent during the extension of the mission. For reverse engineering purposes, the current standardized ESA  $\Delta V$  margin philosophy [16] for chemical propulsion to the executed maneuvers (considering that MESSENGER is a NASA mission) has been applied. It has been included a 5% margin on deterministic (DSM, MOI, OCM) and a 100% margin on stochastic (TCMs, CMDs, AMDs, etc.). A total of 2223.36 m/s has been obtained, comparable with the two allocated total  $\Delta V$ . Additionally, an estimation of some maneuvers has been performed to confirm the values reported inside the budget using basic Keplerian orbit theory according to available data [17]. They are compared in Table 8, showing a close similarity. In particular, an estimation for DSM-1  $\Delta V$  has been computed using a Multiple Revolutions Lambert arc solver between the positions of the S/C at the Earth and Venus flybys and maneuvering location, by exploiting MESSENGER ephemerides [14]. A visualization of DSM-1 is presented in Figure 4.

Maneuver	Value executed	Value estimated	Relative Error
OCM 1	4.22 m/s	4.13 m/s	1.45 %
OCM 2	26.35 m/s	25.97 m/s	2.14 %
MOI 2	49.7 m/s	49.45 m/s	0.5 %
DSM 1	315 m/s	330 m/s	4.57 %

**Table 8:** Comparison between real maneuvers and estimated ones.



(a) DSM-1 arc propagated on MATLAB.



(b) DSM-1 arc plotted ephemerides on GMAT.

**Figure 4:** DSM-1 Arc  $\Delta V$  estimation and comparison.

Lastly, the ToF was roughly estimated using a Hohmann transfer with an additional revolution on the transfer orbit, without taking into account the phasing of planets and maneuvers [17]. The value retrieved was 442.75 days against the actual ToF being 445.75 days, thus with a relative error of 0.67%.

## 2 Propulsion Subsystem

### 2.1 Introduction

The MESSENGER propulsion system was a pressurized bipropellant, dual-mode system, using Hydrazine ( $N_2H_4$ ) and nitrogen tetroxide ( $N_2O_4$ ) as bipropellants, whereas  $N_2H_4$  was used as a monopropellant. The main purposes of the MPS were the reaction wheel off-loading, imparting  $\Delta V$  during orbital maneuvers and providing a backup attitude control system in the event of multiple wheel failures. In this report, the adopted solutions for primary and secondary propulsion will be described and analyzed. Thereafter, a preliminary sizing of the main features of the propulsion system will be carried out.

### 2.2 Propulsion Architecture

Propellant and pressurant storage was provided by three main propellant tanks, a refillable auxiliary fuel tank, and a helium pressurant tank. These tanks could hold approximately 231 kg of oxidizer and 368 kg of fuel for use as propellant. Both propellant and pressurant tanks will be better described in section 2.2.2. Moreover, there were a total of 17 thrusters in the MPS. All kinds of thrusters and their configuration will be analyzed in section 2.2.4.

#### 2.2.1 Hydraulic schematic

The pressurization system, fuel/oxidizer feed system, and thrusters were the four primary components of the hydraulic schematic presented in Figure 5[7], followed by secondary structures, electrical and thermal management subsystem.

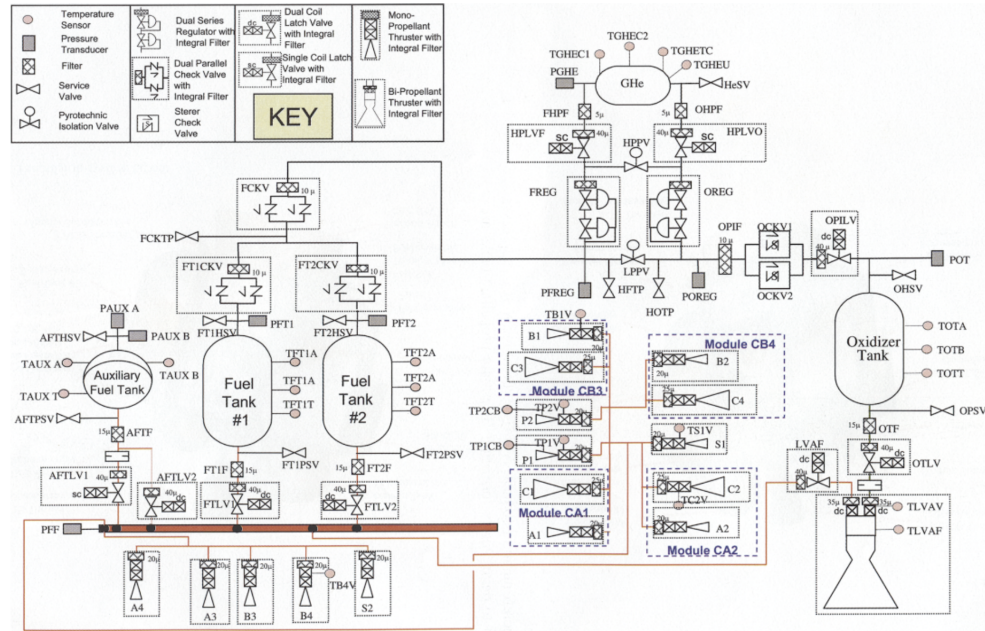


Figure 5: Hydraulic schematic.

#### 2.2.2 Tanks

A simplified sketch of the configurations of all tanks is depicted in Figure 6[18].

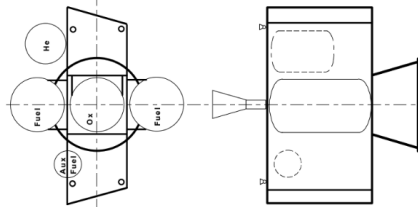


Figure 6: Tanks arrangement.

### 2.2.2.1 Main propellant tank

The S/C had three large propellant tanks installed along its  $y$  axis, with the  $+y$  and  $-y$  tanks storing fuel and the tank situated at the origin of the  $xyz$  coordinate frame containing the oxidizer. The axes are those in Figure 7. A helium pressurization system controlled the pressure in these three tanks. They each had two ring baffles but no diaphragms, allowing the propellant to freely travel within the tanks. Since the tanks lacked diaphragms, the main tanks could only be utilized for maneuvers with acceleration in the  $+z$  direction, as the tanks' outlet was placed at the  $-z$  end. To guarantee that the propellant was settled at the outlet end of the tank, all main tank burns began with a short "settling burn" to force the propellant to the outlet end of the tank. Furthermore, each tank outlet had a 6A1-4V-titanium vortex suppressor to prevent vortex formation. It has been thought that the main propellant tanks were symmetrically positioned about the centerline of the S/C in order to keep the S/C's center of mass under control during fuel expulsion in flight. Tank lateral support was provided by four titanium struts, two of which were boss mounted and two of which were side mounted. The justification for the propellant selection and masses, other than the size of the main tanks, will be discussed in sections 2.4.1 and in section 2.4.2.

### 2.2.2.2 Auxiliary tank

A small 6A1-4V titanium auxiliary tank was a hazardous-leak-before-burst design. For use in minor burns (such as attitude control, precision velocity adjustment, and settling burns), it included an internal diaphragm that enabled positive expulsion of propellant. A tank large enough to hold all of the propellant required for these mission functions was considered, but it was determined to be exceedingly heavy. As a result, according to operational studies of the propulsion system, the auxiliary tank was decided to be operated in the blowdown mode between 1.93 and 0.76 MPa during settling and attitude control burns and then periodically refilled from the main fuel tanks during the flight. As a result, the auxiliary tank was substantially smaller and more mass-efficient. On the bottom left of Figure 5, the auxiliary tank is visible.

### 2.2.2.3 Pressurant tank

The helium tank was a composite over-wrapped leak-before-burst pressure vessel with a titanium lining that was based on the flight-tested A2100 helium tank. The existing helium tank was given a second exit, as shown in Figure 5, to enable dual pressurization of the fuel and oxidizer main tanks. In section 2.4.3, through reverse engineering, the justification for the pressurant's selection, mass, and operating pressure will be provided.

### 2.2.3 S/C adapter

Initially, the LVA thruster was mounted on the top deck of the S/C, which produced a compact, mass-efficient S/C adapter. After that, the S/C adapter was relocated, creating a handy mounting deck for most of the S/C's instruments. The in-flight propulsion system had to be launched in the "upside down" position as a result of this arrangement. This orientation required the propellant tank outlets to be located in an upward position during launch, as the pressurant would have been close to the tank outlet. As a result, the main tanks were not equipped with screen-type propellant management devices (PMDs). During the mission, a different method for supplying gas-free propellant was needed. To tackle the problem, a positive expulsion diaphragm tank paired with monopropellant settling thrusters was designed. Monopropellant thrusters could be used to settle the propellant in the main tanks using the diaphragm tank as the propellant source. The auxiliary tank was better described in section 2.2.2. Moreover, the tank loads were transferred through the side panel, into the S/C square-to-round adapter, and to the Delta II interface ring, resulting in an acceptable launch load distribution at the Delta II interface ring.

### 2.2.4 Thrusters

As mentioned earlier, there were a total of 17 thrusters in the MPS. The necessary S/C forces were provided by three distinct types of thrusters placed in five different thruster module configurations. To support thrusters, fill and drain valves, and electrical interface connectors, the MPS had additional structures and brackets. Most of these secondary structures were created using magnesium, and the intention was reportedly to minimize mass. To operate individual propulsion components, the MPS had a dual-string electrical system with harnesses, diode terminal boards, and connectors. 12 electrical connectors connected the MPS to the S/C. To keep the MPS thermal system operating at suitable temperatures, heaters were used. Heaters were employed to maintain propellant temperatures during the cruise phase and to pre-heat the thrusters prior to operation during the operational stages. The total power for these heaters was 143 W. The thruster valves, valve panel, fill and drain valve bracket, and different propellant manifolds all had cruise-phase heaters attached. The propellant and pressurant tanks also had heaters on them. The cruise-phase heaters on helium and primary propellant tanks were controlled by S/C software, and the other cruise-phase heaters were controlled by mechanical thermostats. Monopropellant thruster catalyst bed heaters and the LVA flange heater were operational-phase heaters, which were used when the MPS was in use. When activated, the LVA flange heater was regulated by mechanical thermostats, whereas all catalyst bed heaters were time controlled. The maximum power of operational-phase heaters was 69 W.

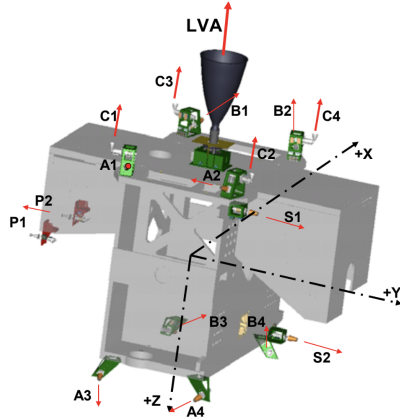


**Figure 7:** MPS thruster configuration.

Force direction	Thruster used
+X	A1A2A3A4
-X	B1B2B3B4
+Y	A2A4B2B4
+Y	P1P2
-Y	A1A3B1B3
-Y	S1S2
+Z	A1A2B1B2
+Z	C1C2C3C4
-Z	A3A4B3B4

**Table 9:** Thrusters used to generate a needed force.

Control axis	A Thrusters	B Thrusters	C Thrusters
+ Around Y	A3A4	B1B2	C1C2
- Around Y	A1A2	B3B4	C3C4
+ Around Z	A1A3	B2B4	-
- Around Z	A2A4	B1B3	-
+ Around X	A2A3	B2B3	C2C4
- Around X	A1A4	B1B4	C1C3

**Table 10:** Thrusters used to generate a needed torque.

Figure 7[19] depicts the MPS thruster configuration, which is further described in section 2.2.4.1 and section 2.2.4.2.

#### 2.2.4.1 Primary propulsion - orbital changes and corrections

For use as the LVA thruster, two bipropellant thrusters were evaluated. The better-performing, lower-thrust Leros-1c was traded against the worse-performing, higher-thrust Leros-1b. When gravity losses during the MOI burn were taken into account, the model with the higher thrust traded more favorably, and the Leros-1b was chosen. The Leros-1b also had a larger and more thermally resistant operational box. Therefore, the flight-tested Leros-lb thruster, supplied by Atlanta Research Corporation–United Kingdom Division (ARC UK), was the large velocity adjustment thruster. The LVA had a nominal mixture ratio (MR) of 0.85, a thrust output of at least 667 N, and a specific impulse of 316 s. The Leros-1b was certified to run on fuel and oxidizer inlet pressures up to 1.999 MPa, which was necessary to account for the S/C's thermal conditions as well as some potential feed system failures (for example, the failure of one segment of a pressure regulator) and/or subtle changes in component flow characteristics over time. Large maneuvers, like the five DSMs and the MOI burn, required the  $\Delta V$  that the LVA offered. The LVA thruster was used at least six times during the mission. For a dual-mode propulsion system, this directly influenced the propulsion system fuel and oxidizer system pressurization strategy and its capacity to limit the diffusion of nitrogen tetroxide ( $N_2O_4$  or NTO). Long-duration missions must account for NTO diffusion. The accumulation of NTO in the fuel pressurization system as a result of NTO vapor migration could cause an energetic reaction and hardware failure. The MESSENGER propulsion system configuration required to account for this possibility. Four 22-N, monopropellant LVA-thrust vector control (TVC) thrusters (also known as C-thrusters) provided primary propulsion for some of the smaller velocity adjustment maneuvers as well as thrust vector guiding forces during main thrust burns. The C-thrusters were flight-proven Aerojet P/N MR-106Es. In both the pressurized and blow-down modes, they were supplied with  $N_2H_4$ . Their specific impulse was 234 s.

#### 2.2.4.2 Secondary propulsion - SK and attitude

12 monopropellant thrusters provided 4.4 N of thrust at an average specific impulse of 220 s. They have been used for fine attitude control burns, small AV burns, and momentum management. The 4.4-N thrusters were flight-proven Aerojet P/N MR-111Cs.  $N_2H_4$  was likewise delivered to these thrusters in both pressurized and blow-down modes. The following observations have been obtained by analyzing Figure 7:

- For redundant three-axis attitude control, eight 4.4-N thrusters (A and B) were arranged in double-canted sets of four. It should be emphasized that each of these thrusters was angled at 45°, so the S/C could be controlled without the use of a set of 12 thrusters.

- Two 4.4-N thrusters (S) were used to adjust the velocity in the sunward direction.
- The last two 4.4-N thrusters (P) were employed to adjust the velocity in the opposite direction of the Sun. The P thrusters were located on the S/C  $-y$  side and protruded through the sunshade.
- The P and S thrusters delivered  $\Delta V$  thrust in a different direction from the C-thrusters and LVA by pointing along the S/C's  $+y$  axis and  $-y$  axis.

All potential maneuvers and the thrusters that carry them out are shown in Tables 9 and 10. Figure 7 is used to reference names of thrusters and axes. It must be noted the dual propulsion system was chosen for its great flexibility in  $\Delta V$  range.

## 2.3 Propulsion System Phases and ConOps

MPS had five operational modes: one for Launch phase, one for Cruise phase and three active modes providing small, medium and large  $\Delta V$  maneuvers. Active modes were subdivided into some or all of the following segments: *Settle* (a small burn using 4.4 N thrusters and the auxiliary tank to settle propellant at the bottom of the tanks); *Refill* (to refill the auxiliary tank with fuel from the main tanks); *Main Burn* (to provide most of the maneuver  $\Delta V$ , while smaller thrusters provide for TVC and ACS); *Final Trim* (22 N thrusters provided the remaining  $\Delta V$ ); *Tweak* (on-pulsing firing of the 4.4 N to stabilize attitude before returning the control authority to the reaction wheels)[19]. The five modes consisted of:

- **Launch Mode:** Firstly, the main propellant tanks thermal conditioning was activated, followed by the transition to launch and S/C separation. It continued through fuel-feed manifold evacuation and bleed-in in preparation for the first thruster operation, ending with S/C detumble.
- **MPS Cruise Phase:** MPS temperatures were kept inside the range by heaters, as explained in section 2.2.4, and Ground Segment was notified if a limit was reached.
- **MPS Active Mode-1:** Either 4.4 N or 22 N monopropellant thrusters were used, with fuel supplied from the auxiliary tank operating in blow-down mode. A Mode-1 burn was divided into two segments: main burn and tweak. Thruster catalyst bed heaters were powered-on, the auxiliary tank latch valve was opened and pressure was autonomously verified. Thrusters were fired as required, and then the system entered the tweak segment. Finally, the system was “safed” and attitude control was returned to the S/C reaction control wheels.
- **MPS Active Mode-2:** The 4.4 N (ACS) and 22 N (LVA-TVC) monopropellant thrusters pressure-fed from the main tanks were used. This mode was divided into three segments: settling, main burn, and tweak. Catalyst beds were heated and pressure verified. The settling segment settled propellant in the main tanks by firing the top deck attitude control thrusters (A1, A2, B1, and B2) using fuel from the auxiliary tank in a blow-down mode. During the main burn segment, LVA-TVC thrusters were fired using pressurized and regulated fuel from the main fuel tanks. During the main burn, the main fuel tank outlet latch valves were cycled open and closed so that fuel was used from only one tank at a time, maintaining the center of mass well within the control authority limits of the LVA-TVC thrusters.
- **MPS Active Mode-3:** The bipropellant LVA thruster pressure-fed from the main tanks was used. This mode was divided into five segments: propellant settling, stand-alone auxiliary tank refill, main burn, final trim burn, and tweak. The settling phase readied the system for accessing the main tanks. With the propellant settled, one of the main fuel tank outlet latch valves was opened and the auxiliary tank was refilled. The top-deck 4.4-N thrusters continued to fire during the refill maneuver to keep the main tank settled. LVA thruster was fired. On-pulsing the 22-N (LVA-TVC) thrusters provided for TVC. The 4.4-N attitude control system thrusters provided supplemental attitude control as required. The LVA thruster was shut down and the 22-N thrusters take over the responsibility of completing the remaining  $\Delta V$ . Center-of-mass control was maintained by the main fuel tank outlet latch valve switching at regular intervals. Afterward, the tweak segment was completed using propellant from the auxiliary tank and attitude control was returned to the reaction wheels and the propulsion system was “safed”.

A peculiar element of MPS operations was the periodic refill of the auxiliary tank from the two main fuel tanks. This operational approach was adopted to allow use of a small low-mass auxiliary tank. The use of a dual propulsion system with bipropellant mode for large maneuvers and monopropellant mode for medium to small maneuvers, ACS, and settling segment was recognized as a means to minimize the necessary propellant load. This led to the necessity of a second fuel main tank and the risk of CoM shifting, which was solved by cyclic open-close of the two propellant latch valves as explained above.

### 2.3.1 Propulsion Maneuvers Breakdown

To justify the selected architecture from a reverse engineering perspective, the maneuvers propulsion data collected during Operations were analyzed to find the rationale between the maneuver itself, the entity of the  $\Delta V$  and the MPS Mode. A few of them are shown in Table 11 [14] [12].

Maneuver	Mode	Thrusters	ACS Thrusters	$\Delta V$ [m/s]
Launch Detumble	1	N/A	A&B	0.460
TCM-1	2	C	A&B	17.901
TCM-2	2	C	A&B	4.589
TCM-5	1	S	A&B	1.103
TCM-6	1	P	A&B	0.150
DSM-1	3	LVA	A&B	315.633
TCM-10	1	B	A	1.281

**Table 11:** Maneuvers and Propulsion Modes during Operations.

From Operation data, maneuvers can be generally correlated with propulsion modes and architecture [19]:

**Mode 1:** and in general 4.4 N thrusters were used for Launch Detumble, small TCMs ( $\leq 3$  m/s), CMDs and AMDs. 4.4 N thrusters were also used for ACS in the other active modes;

**Mode 2:** with 22 N thrusters was utilized for larger TCMs, OCM-2 (3-20 m/s);

**Mode 3:** firing the 667-N bipropellant thruster was used for DSMs, MOI and OCM-1.

Regarding Trajectory Correction Maneuvers, the employment of thrusters might be subdivided in terms of burn direction, attitude, and thermal limitations due to the existence of the sunshield, as shown in the table 12 [19].

Thrusters	Type	$\Delta V$ magnitude	$\Delta V$ direction
<b>C-thrusters</b>	22 N LVA-TVC	3 to 20 m/s	Sun-S/C- $\Delta V$ direction angle between 78-102 deg
<b>S-thrusters</b>	4.4 N mounted on sunward side	$\leq 3$ m/s	within 12 deg with respect to Sun-S/C direction
<b>P-thrusters</b>	4.4 N mounted on antisun side	$\leq 3$ m/s	within 12 deg with respect to Sun-S/C direction

**Table 12:** Restriction in burn directions.

Maneuvers with  $\Delta V$  directions outside these restrictions had been performed by either a turn and burn approach if no thermal safety margin was breached, or a less efficient vector components approach combining some of the maneuver types.

## 2.4 Preliminary Sizing

Key onboard components were sized in the context of reverse engineering to verify literature data and explain design choices.

### 2.4.1 Propellant selection and masses

According to planetary satellite data, the nominal dry mass of the S/C can be determined from the payload mass. For a P/L mass of 41 kg, linear regression shows a dry mass, including a 20% system margin, around 480 kg, which is comparable to the actual dry mass of 507.9 kg [7]. The total dry mass is assumed to coincide with the mass of the S/C after the last planned maneuver during the designed mission (so excluding the extension). The mass preceding a maneuver may be calculated by inverting the Tsiolkovkij equation, and hence the amount of propellant discharged to complete that precise maneuver. Starting with the total dry mass at launch, each maneuver was applied, beginning with the most recent (OCM-5) and progressing to the first (Launch Desaturation), to determine the quantity of propellant ejected after each burn. This allowed the amount of propellant utilized for the monopropellant and bipropellant modes of the Propulsion Subsystem to be separated. A margin of 5% on deterministic and of 100% on stochastic  $\Delta V$  was included. By summing up all the masses, it is possible to retrieve an estimated wet mass including margins of 3% to take into account ullage, 2% for residuals (MAR-MAS-080) and 0.5% for the loading uncertainty [16]. The wet mass computed is 999.56 kg. The predicted wet mass is very close to the real value, with a 3.52% relative error compared to the actual wet mass of 1093 kg. After separating the monopropellant from the bipropellant mass, it is possible to calculate the oxidizer and fuel masses from the mixture ratio, which was taken from mission data [7] as  $OF = 0.85$ . In table 13, the computed propellant masses values are compared with the real values.

	$m_{fuel}$ [kg]	$m_{oxidizer}$ [kg]
<b>Computed masses</b>	323.68	224.5
<b>Real masses</b>	365.3	231.6

**Table 13:** Propellant masses comparison.

The relative error between computed and real masses is 11.4 % and 3.1 % respectively for fuel and oxidizer masses. The masses result is slightly underestimated because of the lower estimated dry mass with respect to the real value. The fuel masses are subdivided into the mass allocated for the bipropellant mode of 264 kg and the one for the monopropellant mode of 59.6 kg. Because of its storability, high specific impulse and adequate aging properties hydrazine and nitrogen tetroxide are a popular pair in bipropellant engines. They are hypergolic, have rapid combustion, and have high performance. The capability of hydrazine to decompose exothermically can be also exploited in monopropellant thrusters, making it very convenient in a dual-mode system. On the other hand, hydrazine is extremely toxic, explosive at 50°C and it spontaneously oxidizes in air at ambient temperature. Usually, *OF* maximizing the performances is around 1.34 [20]. The choice of a lower value can be attributed to lowering the temperature in the combustion chamber for cooling reasons. It can be also related to a tank configuration choice: a higher *OF* would have minimized the gap between oxidizer and fuel masses, resulting in the use of two main tanks rather than three, each of which was different in volume, thus producing a configuration problem [18].

#### 2.4.2 Tanks sizing

For MESSENGER, a brand-new, lightweight main propellant tank was created. The tank configuration was made entirely of titanium 6A1-4V that had been solution-treated and aged (STA). The tank had a diameter of about 559 mm and a length of around 1,041 mm. The thickness of the hemispherical domes was roughly 0.5 mm. The thickness of the cylindrical portion was roughly 1.0 mm. Two 178 mm wide, 0.25 mm thick, 6A1-4V titanium baffles were included in each tank design for controlling S/C nutation [18]. Given the results of section 2.4.1, the volumes of the propellant tanks can be retrieved. The auxiliary tank volume is calculated on the basis of this assumption: due to balancing concerns, the total volume of the fuel tanks must be double that of the oxidizer. Therefore, the excess volume of fuel is attributed to the auxiliary tank. The assumption is reasonable since at launch all the tanks are full. Volumes and masses of the tanks computed are in Table 14.

	$V_{\text{tank}}[\text{m}^3]$	$m_{\text{tank}}[\text{kg}]$	$t_{\text{dome}}[\text{mm}]$	$t_{\text{cyl}}[\text{mm}]$	$h_{\text{tank}}[\text{m}]$	$r_{\text{tank}}[\text{m}]$
Main	0.1706	4.7	0.55	1.1	0.85	0.28
Pressurizer	0.1140	7.59	2.4	4.7	0.61	0.3
Auxiliary	0.0124	0.26	-	0.36	-	0.14

Table 14: Tanks properties.

Tank masses are sufficiently close to the real masses of the main, pressurizer, and auxiliary tanks, which are 8, 10, and 2.5 kg, respectively. The main tank mass computed is lower because it does not include baffles for nutation control. Volumes were computed including a margin of 10% [16]. Tanks were sized to hold the pressure computed in section 2.4.3, admitting stress of 380 MPa including a safety factor. Except for the auxiliary tank, all tanks were considered cylindrical with hemispherical domes. Using the real diameter of the tank cylindrical portion, the dome height was tuned such that the estimated tank length was sufficiently close to the real value. For the pressurizer tank, the radius and length were reasonably estimated from the configuration. The auxiliary tank was sized as spherical. Titanium 6A1-4V was chosen for the low density and higher resistance with respect to aluminum, compatible with propellant type, and was proved to be compliant with structural vibration 85 Hz minimum frequency requirement. Different tank shape and configuration concepts were studied during design, varying from the all-spherical tank “oil derrick” approach to the four-equal-length two-different-diameter cylindrical tanks, to the four-equal-diameter two different-length cylindrical tanks, to the finally adopted three-equal-volume cylindrical tank configuration. The oil derrick approach was mass efficient but required a large, and therefore heavy, sunshade. The choice of the three-equal-volume cylindrical tank configuration allowed the three tanks to be mounted to three sides of the S/C structure center box, resulting in improved load transmission [18]. As it is symmetrically positioned with respect to the CoM, the pressurizer tank is believed to be outside the main tanks’ centerline in order to balance the sunshade.

#### 2.4.3 Pressurant gas selection and masses

The pressurizing system of MESSENGER is composed of two parts: pressure fed and blow down. The mass, pressure and volume of the pressurizer for both architectures will be calculated through the reverse sizing procedure.

##### 2.4.3.1 Pressure fed

This architecture was utilized to pressurize the main tanks during active modes 2 and 3. Helium was chosen as a pressurizer because of its low molar mass, which allowed for a lower pressurizer mass to be used while still achieving the desired pressure level. To determine the pressure in the tanks, the standard pressure cascade procedure was followed. The pressure in the tanks is the sum of the chamber pressure and the losses (injector and feeding line). For the injector losses, a value of 30% of the pressure chamber has been chosen based on literature and heritage. As for the feeding lines, losses were calculated assuming a pipe speed of 10 m/s and considering the oxidizer density, which represents the worst-case scenario due to its higher density compared to the fuel. The MESSENGER chamber pressure data is not available, so an assumption must be made. Usually, for in-space propulsion, the chamber pressure varies between 10 and 20 bar. By choosing 11 bar in the

combustion chamber, the results obtained in terms of pressure and mass are shown in Table 15. This choice is reinforced by the fact that by adding the pressure cascade results to the 11 bar, the pressure in the main tanks achieved is 15 bar, which is the same value reported in MESSENGER literature [19]. The initial value of the pressurant is chosen as 10 times the pressure in the tanks, which is a typical value. From the literature, the pressurizer pressure is 232 bar. The difference between this value and the one in Table 15 can be derived from more precise calculations and models utilized in practice.

$V_{\text{press}}[\text{m}^3]$	$m_{\text{press}}[\text{kg}]$	$P_{\text{tank}}[\text{bar}]$	$P_{\text{press}_{\text{in}}}[\text{bar}]$	$P_{\text{press}_{\text{fin}}}[\text{bar}]$
0.11	2.81	15.02	150.20	15.02

**Table 15:** Pressure fed pressurizing system parameters.

The mass of the pressurant already contains the 20% margin suggested by MAR-MAS-90 document. This value is very close to the real one (2.3 kg) [19], the difference is due to the presence of the margin and because it is calculated on the margined value of propellant mass and volume, thus leading to an overestimation. It has also been observed that the pressurant tank is situated far from the sunshield. It has been thought that this decision was made also with the goal of placing the tank in a well-thermally-controlled area to prevent the pressurant from becoming overheated.

#### 2.4.3.2 Blowdown

This architecture was used to pressurize the auxiliary tank, which was mainly used during active mode 1. The pressurizing gas used was helium for the same reasons mentioned before and it was stored in the auxiliary tank, separated from the propellant by a diaphragm. The reverse sizing process is similar to the one outlined in section 2.4.3.1. The only difference is the introduction of the blowdown ratio (B), which is defined as the ratio between initial and final pressurizer pressure. In this case, the value has been calculated by knowing the initial and final pressure from literature [7] and it is equal to 2.54, slightly lower with respect to the common B range of 4-6. The calculations are made under the assumption of isothermal expansion, which corresponds to a slow expansion. Since the discharge is slow in the blowdown system, this hypothesis is valid. The parameters obtained through the reverse sizing are shown in Table 16. It can be seen that the values obtained for initial and final volume are compliant with the dimension of the auxiliary tank calculated in section 2.4.2, in fact, the final volume occupied by the gas is almost equal to the auxiliary tank.

$V_{\text{press}_{\text{in}}}[\text{m}^3]$	$V_{\text{press}_{\text{fin}}}[\text{m}^3]$	$m_{\text{press}}[\text{kg}]$	$P_{\text{press}_{\text{in}}}[\text{bar}]$	$P_{\text{press}_{\text{fin}}}[\text{bar}]$
0.0048	0.0123	0.0184	19.30	7.60

**Table 16:** Blowdown pressurizing system parameters.

The MPS total dry mass, including thrusters, valves, plumbing, secondary structures and 10% margin to account cables, is 74.17 kg, slightly lower than the real value of 81.74 kg due to the lower value of the computed masses of tanks. Power consumption ranges from a minimum of 21.9 W in outer cruise ( $>0.85 \text{ AU}$ ) to a maximum of 95.6 W in inner cruise ( $<0.85 \text{ AU}$ ), which is reasonable due to the more time and maneuvers spent in inner orbital region.

#### 2.4.4 Feeding lines selection

Four pressurization schemes were traded. These designs included single helium tank pressurization (based on NEAR S/C), separate fuel and oxidizer helium tanks, pyro ladder oxidizer tank isolation, and single tank/dual circuit pressurization. Acceptable NTO diffusion prevention, mass efficiency, packaging capabilities, and operational flexibility were used to calculate the figures of merit. Because the fuel and oxidizer tanks shared the same pressurization path, the single helium tank concept, while efficient in terms of mass and packaging, did not provide adequate NTO diffusion protection. Both the separate helium tanks and the pyro-ladder isolation approaches prevented NTO diffusion well, but they were either heavy, required additional packaging capacity, or had restricted operational flexibility. A single helium tank with separate fuel and oxidizer outlets was used as an NTO barrier in this design. In addition, two isolation valves were added to offer cross strapping capabilities for the pressurization system in the case of a high-pressure latch valve or regulator failure. This added system redundancy for relatively little weight. The high and low pressure latch valves, regulators, pyro isolation valves, check valves, filters, fill and drain valves, pressure transducers, bimetallic joints, fittings, and tubing required to control propellant to the system thrusters were all included in the propulsion system integrating components. Regarding the feedlines utilized for attitude thrusters, shorter pipes were designed since they had fewer vacant spots. This prevented extended ignition and extinction transients. A rough diameter sizing of the feeding lines has been performed exploiting Moody chart [20] under the hypothesis of laminar flow. The diameter allowing the 10 m/s feeding velocity and the consequent pressure drop was respectively for fuel and oxidizer over 1 m line length:  $d_f = 2.4\text{mm}$  and  $d_{ox} = 1.2\text{mm}$ . For different lengths, diameter changes as  $d \propto \sqrt{l}$ .

## 3 TTMTC Subsystem

### 3.1 Introduction

The purpose of the design of the communication system was to provide an ongoing, secure data transfer with all the Ground Stations. For S/C control and telemetry transmission, MESSENGER used X-band communication across the Deep Space Network. The primary goals of the telecommunications subsystem were to provide the highest quality and quantity of S/C housekeeping telemetry and scientific data return, to provide S/C command capability, and to provide range tracking data and highly accurate Doppler to precisely determine S/C velocity and position. Furthermore, the RF subsystem was used to study Mercury's internal structure, geology, topography, and gravity. TTMTC design choices were directly correlated to ADCS pointing constraints, TCS temperature restriction, OBDH on-board memory sizing, and EPS critical power consumption.

### 3.2 TTMTC architecture

The MESSENGER RF Telecommunications Subsystem operated in the X-Band frequency range. The frequencies were 7.2 GHz for uplink from GS and 8.4 GHz for downlink from the S/C. The Deep Space Network stations' 34-m and 70-m antennas were used for communication. The RF design was guided by MESSENGER's inner-planet trajectory, because Earth may be in any direction with respect to the S/C. For this reason, high-gain coverage had to be possible in all directions. The RF telecommunications subsystem consisted of four different types of devices [21]:

**General Dynamics Small Deep Space Transponders (SDSTs):** These are instruments used in deep space to communicate with S/C during interplanetary missions. X-Band Redundancy Small Deep Space Transponders (SDSTs) were in charge of receiving and demodulating the RF uplink signal (from Earth to the S/C), generating and modulating the RF downlink signal (from the S/C to Earth), and relaying uplinked ranging and Doppler components, which were used to determine the distance and velocity of the S/C with respect to Earth.

**Solid-State Power Amplifiers (SSPAs):** SSPAs enabled the downlink signal from an SDST to be amplified and routed to the appropriate antenna based on the mission requirements. Each SDST could only have one active downlink channel active at any given time, and the signal from this channel was amplified by two passive hybrid solid-state power amplifiers. The latter might be set to one of four modes: "distributed front", "distributed back", "lumped", and "off". The "distributed" modes of the SSPAs fed the RF downlink signal to either the front or back Phased-Array Antenna. In "distributed" modes, the RF downlink signal was split into eight paths and amplified by eight stick amplifiers, each of which had a four-bit phase shifter, small-signal amplifier, driver amplifier, power amplifier, and isolator. The output power of each stick amplifier was around 4 dBW. Four sticks worked together per SSPA in "distributed" mode, producing a power output of around 10 dBW. The "lumped" mode routed the RF downlink signal to the fanbeam antenna or the LGAs (Low-Gain Antenna) via the two RF switch assemblies. In the "lumped" mode, the amplifier provided a 10 dBW output power for the fanbeam antenna and LGAs.

**Phased-array antennas (PAAs):** The high-gain downlink signal was produced by two phased-array antennas oriented in diametrically opposite directions. Each PAA was capable of electronically steering  $\pm 60^\circ$  in the XY plane of the S/C, as shown in Figure 8. This meant that the antenna could point its signal in various directions without having to physically move the entire antenna. The omnidirectional high-gain coverage was achieved using S/C rotation about the Y axis in conjunction with electronic scanning of the antenna beam.

**Medium- and low-gain antennas (MGA),(LGA):** 2 fanbeam antennas provided medium-gain uplink and downlink capabilities, whereas 4 emispherical low-gain antennas completed the antenna suite. MGA and LGA were typically used as backup or alternative antennas to the high-gain antennas.

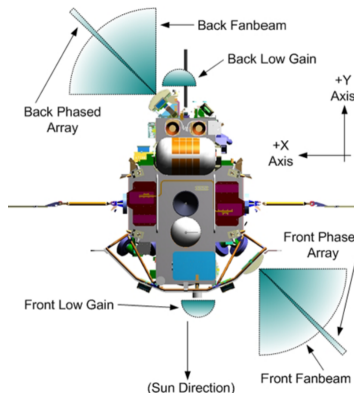


Figure 8: MESSENGER S/C antennas location in body frame.

### 3.3 TTMTC subsystem design rationale

The system was cross-strapped on both sides of the transponders, providing near-full redundancy on both the uplink and downlink, while each of the distributed power amplifiers was dedicated to one phased-array antenna, as in Figure 9. This configuration provided a non-critical degradation in the event of an amplifier-element failure. Even if an entire array failed, there was enough recorder capacity to save orbit-phase science data and downlink those data later using the other array and a revised downlink schedule, similarly as explained in section 3.3.3 for downlink data rate variation in orbit phase [22].

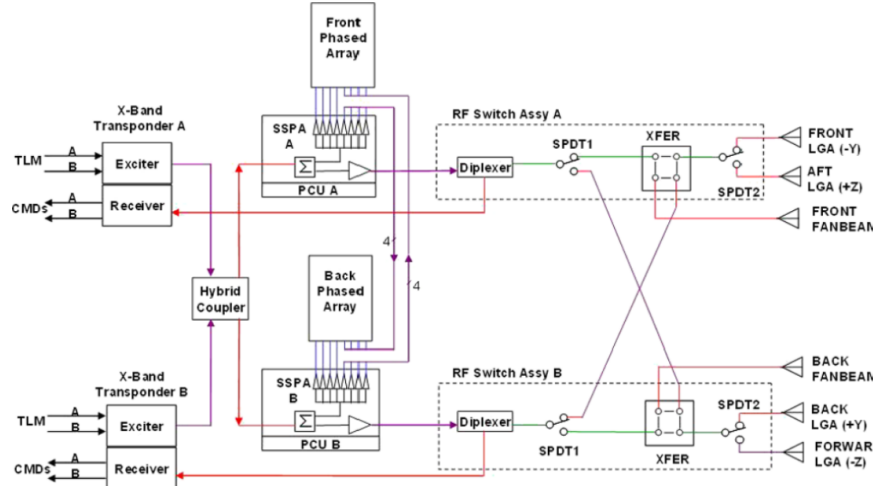


Figure 9: TTMTC architecture block diagram.

#### 3.3.1 Antennas selection, polarization and positioning

The inner planet trajectory of the MESSENGER mission resulted in the need for a high-gain downlink to Earth in all directions around the S/C. This requirement was met by the electronically steerable PAAs. PAAs have had limited application in the deep-space to date but one-dimensional electronically scanned antennas increased reliability, eliminating the use of deployed components, gimbal dish and parabolic antennas that could fail and distort in the extreme thermal environment of Mercury. The thermal environment also precluded the use of active radiative elements for PAAs during uplink, which was not necessary given the low uplink data rate. Despite the sunshade pointing constraint, rotation around the S/C-Sun line was still permitted without violating the constraint, allowing the array scanning requirement to be reduced from a two-dimensional to a one-dimensional scan, which combined with S/C rotation enabled Earth downlink for all Sun-Earth-S/C angles. Additionally, array scanning in the broad beam plane required the least number of cabled connections between the power amplifiers and the array and thus minimizing mass compared to narrow beam plane scanning [22]. Medium-gain and low-gain antennas were used for uplink and low-gain downlink during the cruise phase and emergency. In fact, when the high-gain antenna could not be pointed at the Earth station due to S/C pointing constraints, the medium-gain antenna was used to provide moderate gain or amplification to the signal. The MGA was useful when the S/C was in close proximity to Earth or when it required a wider coverage area. The low-gain antenna was used for communication during the early phase of the mission, such as launch and orbit insertion, or when the S/C was in close proximity to the Earth. The antennas were inherently linearly polarized, but a novel combination of parasitic monopoles and dummy waveguides was developed to create right-hand circular polarization, resulting in a 3 dB improvement in link performance due to the fact that the DSN antennas are circularly polarized. Configuration of the antennas combined their double (front and back) positioning on the S/C with their beamwidth and steerability to guarantee coverage in all directions, in order for uplink and downlink to be available in all nominal and emergency modes, as explained in section 3.4.2. The forward phased array transmitted through an opening in the Sun shade. A radome attached to the sunshade blocked sunlight, had strong RF transmission characteristics across a 45° angle of incidence, and had little performance change over a temperature range of -100 to +300°C [23] [24].

#### 3.3.2 Ground station selection

The Deep Space Network is NASA's international network of massive radio antennas that support interplanetary S/C missions as well as a handful that orbit the Earth. Deep space missions are visible for long periods of time from a large portion of the Earth's surface, and so require few stations. [25] The DSN is made up of three sites that are spread equidistantly across the world, approximately 120 degrees apart in longitude. These sites are at Goldstone, California, near Madrid, Spain and near Canberra, Australia. The strategic placement of these sites permitted constant communication with MESSENGER. As a matter of fact, before a distant S/C dropped below the horizon at one DSN site, another may pick up the signal and carry on communicating. Each facility is situated in semi-mountainous, bowl-shaped terrain to help shield against radio frequency interference. Both 34 m and 70 m DSN antennas were planned to be used during operations. Broadly speaking,

while almost all S/C nominal operations could be conducted on the smaller and less expensive antennas of DSN, during an emergency the use of the largest antennas was crucial because the S/C could have a reduction in power availability, current attitude may have precluded the use of high-gain antennas, and recovering telemetry was critical to assessing the health of the S/C and planning the recovery. Consequently, communication was accomplished with 34 m DSN antennas for all phases. For emergency communications, the antenna configuration supported an LGA uplink and an MGA downlink over the entire mission using the 70 m DSN antennas while maintaining sunshade attitude requirements and 3 dB link margins [26].

### 3.3.3 TTMTC-OBDH interface

An additional constraint on TTMTC subsystem was imposed by the strong variation of the allowable downlink data rate due to the relative position between Earth and Mercury, including the periods of Solar Conjunction. The strategy to address variable data return was to store most data on the S/C Solid-State Recorder during periods when Mercury is far from Earth and to downlink both previously stored and newly acquired data during periods when Mercury is closest to Earth [7]. A data prioritization scheme will assist in managing the downlink process. The amount of data stored on the SSR is able to reach peak usage of 6.6 Gbit in periods of low data rate, which can be considered more than satisfactory, given that the total yearly data return is of 135 Gbit. Considering 6 days longest conjunction during orbital phase [7], in order to occupy 6.6 Gbit in SSR, data acquisition rate was calculated to be 12.73 kbit/s, which is lower than the average data rate of transmission, thus avoiding on-board memory saturation in the period of transmission right after the conjunction.

### 3.3.4 Frequency and band selection

MESSENGER operated in X-Band with 7.2 GHz for uplink and 8.4 GHz for downlink frequencies, which is one of the bands allocated for Deep Space Telecommunications by the ITU [27] and supported by DSN [28]. General characteristics of the X-band are the exceptional performance benefits not available in other bands, such as less susceptibility to rain-induced disruptions, resistance to interference, support of large range of data rates, and the ability to operate with small remote terminals [29].

## 3.4 TTMTC operations

### 3.4.1 Transmission operations

**Cruise phase:** the sunshade was pointed at the Sun, and the direction of the LVA thruster was oriented normal to the S/C-Sun line to accommodate maneuvers in this attitude. Communication was maintained at all times in this fixed attitude by medium-gain and high-gain antenna clusters on the forward and backward sides of the S/C.

**Orbit phase:** rotation about the Sun line was needed to accommodate instrument viewing, since the instrument-view direction was normal to the S/C-Sun line and opposite the LVA. Albeit thermal requirements were always met, high-rate downlink communications were not maintained during those rotation periods. During the data downlink periods, generally scheduled when the S/C was away from periapsis (supposedly because of better Earth-pointing capabilities due to low orbital velocity), the S/C roll axis was controlled so that one of the high-gain antennas could acquire Earth.

All available data regarding data rates and data volumes that will be used for reverse sizing are in Table 17. In orbit phase, daily bit rate will vary from a minimum of 5 kbps to a maximum of over 35 kbps, with an average value of 17.9 kbps. Higher data rates were reached when near Mercury inferior conjunction and periods with zero data rate corresponded to Mercury superior conjunction. The conservative assumption of 6.5 hours of transmission time of the 8 hours coverage (around 1 hour of the coverage period was dedicated to DSN setup) was used [7], leading to 135 Gbit data volume per year in orbital phase. For Cruise and LEOP the same downlink data rates were assumed. Due to the lack of data in literature and in the perspective of reverse engineering, the same principle to calculate data volume of orbital phase was applied to cruise phase [7], assuming two 6.5 hour transmission periods a week. Since LEOP lasts around 6 days, one contact lasting 6.5 hours is assumed to compute data volume. Uplink is at least 31.25 bps in all nominal operations. It is assumed that data volume included both telemetry housekeeping data and scientific P/L data.

Phase	Uplink	Downlink	Coverage	Data Volume
LEOP	>31.25 bps	>1000 bps	24 hours	23.4 Mbit
Cruise	>31.25 bps	>1000 bps	Two 8-hours passes per week	2.43 Gbit per year
Orbit	>31.25 bps	17.9 kbps	One 8-hours passes per day	135 Gbit per year
Emergency	7.8 bps	10 bps	-	-

Table 17: Data rates and data volumes per phase.

The greatest data volume was obtained in Orbit Phase as expected due to the abundance of scientific data with respect to other phases [7] (391 GB for imaging, 41 GB for atmospheric data, 79 GB for geoscience, etc.). Normally, uplink communications

were accomplished through the MGAs and downlink communications were accomplished through the phased-array antennas. During both cruise and orbital operations, periods of solar conjunction precluded communications, during which no events required ground commands. Prior to these times, the S/C was placed into a safe-hold mode. When Sun–Earth–S/C angle was greater than 17 deg, solar interference did not corrupt communications with the S/C [24].

### 3.4.2 Transmission per mode

TTMTC subsystem was strictly correlated to S/C modes, which are briefly outlined below [24]:

**Operational mode:** nominal mode handled recoverable faults. TTMTC operations proceeded as nominal using HGA;

**Safe-hold mode:** mode triggered by serious faults, the sunshade was pointed at the Sun and an MGA was pointed at Earth;

**Earth acquisition mode:** mode triggered by critical faults or by loss of inertial reference. While the sunshade was pointed at the Sun, the S/C was rotated around the Sun line at 2° per minute. Once per revolution, an MGA output swept past the Earth, and a beacon signal was detected on the ground. After observing this signal sweep several times, a command was timed to intercept and stop the rotating S/C when the MGA was Earth pointing.

For either safe hold or Earth acquisition modes, the S/C telecommunication selected the MGA and LGA that were currently facing Earth. Uplink communications were received through both MGA and LGA. If an extended period with no ground communications occurred, the antenna configurations were autonomously alternated. Once the fault was corrected at ground, operational mode was restored.

### 3.4.3 Tracking operations

**Precision Orbit Determination:** the X-band tracking system on the S/C produced line-of-sight velocity and distance measurements of the S/C from Earth by utilizing the SDSTs, which exploited the Doppler effect. The Doppler measurements were derived from the change in carrier frequency. Furthermore, the solar plasma effect and thermal noise were the two main sources of error in Doppler tracking measurements. The tracking data was utilized to detect the S/C's position and velocity, as well as estimate its future position, allowing for instrument targeting and data processing.

**RF Tracking Operations:** during the Mercury's scientific operations, pointing constraints caused the Earth-S/C vector to no longer be in the preferred direction for high-rate data transmission. Therefore, during these periods, any tracking and RS data must be gathered through the use of the more omni-directional low-gain antennas. This configuration significantly lowered the signal-to-noise ratio for tracking measurements.

**Cruise-Phase Calibration Operations:** the RS cruise operations included calibrations and verifications for range and Doppler measurements in order to increase the accuracy of the Doppler data during the nominal phase. These operations sought to improve the precision of the Doppler data and modify the noise models during the orbital mission phase [21].

## 3.5 Preliminary sizing

Reverse engineering analysis was carried out to validate the data reported in the literature. The calculation has been performed only for the most important communication modes: the science downlink and the command uplink, both during the orbital phase. The main focus of the reverse sizing will be the downlink, while for the uplink only the results will be shown. Power budget in worst case for TTMTC ranges from 65.5 W in Cruise, maximum of 110.5 W in Orbit phase and a minimum of 25.4 W during eclipse. Mass budget allocated for Communication was 31.6 kg [7].

### 3.5.1 Space segment

The phased array antenna was chosen for the scientific downlink. The reasons for this choice are explained in section 3.3.1. The input power requirement is required to size the Solid State Power Amplifier (SSPA), and it has been set as 42W based on the literature [23]. The efficiency may be retrieved using this value, and then the transferred power can be computed. The choice of this amplifier can be justified by its light weight and the absence of excessive power levels. The S/C employed two modes for the SSPA: a standard datarate transmission mode known as *half array mode* and a high datarate mode known as *full array mode*. The *half array* utilized only one of the two SSPAs along with half of the phased array. Instead, the *full array* utilized the entire array and both of the SSPAs. This mode allowed an increase of 6dB in EIRP ensuring that transmissions could be successfully performed even under the most challenging conditions [21]. Moving forward with the design, two significant parameters need to be determined: the Bit Error Rate (BER) and the energy per bit to noise power spectral density ratio  $\frac{E_b}{N_0}$ . Both these parameters shall be minimized. To achieve this objective, encoding and modulation techniques are employed. Encoding introduces additional bits to detect errors, but it increases the necessary data rate. On the other hand, modulation aims to transmit data efficiently to reduce the data rate. Therefore, a trade-off must be made to select the optimal parameters for communication purposes. For the BER, a value of  $10^{-5}$  has been selected, which is typical

for science data transmission. The  $\frac{E_b}{N_0}$  value depends on the selected modulation and encoding schemes. In the MESSENGER mission the *turbo-encoding* was utilized, an innovative system that allowed an extra 0.9 dB margin in the RF downlink [7]. Turbo-encoding combines both convolutional coding and Reed Solomon coding, with parameters of  $K = 15$  and a rate of 1/6. This allowed an exceptionally low needed  $\frac{E_b}{N_0}$  value of 1 dB [22], as can be inferred in Figure 10 [30]. As previously mentioned, encoding and modulation techniques affect the data rate through two coefficients. These two values have not been found for the MESSENGER mission, hence an assumption must be made. A value of 2.28 has been assumed for the encoding coefficient. This is a value used for convolutional coding plus RS but for different values of rate and K. Regarding modulation, a value of 2 has been chosen, representing QPSK modulation. It ensures optimal data rate performance and excellent use of spectrum. For the phased array antenna gain a value of 27 dB has been found in the MESSENGER literature [22]. The principal parameters of the space segment in the science downlink can be seen in Table 18.

P <sub>in</sub> [W]	P <sub>tx</sub> [dBW]	G <sub>tx</sub> [dB]	EIRP <sub>half</sub> [dB]	EIRP <sub>full</sub> [dB]
42	10.21	27	36.21	42.21

Table 18: Space segment parameters for science downlink.

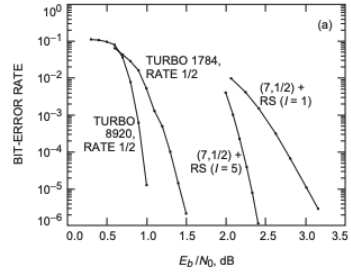


Figure 10: BER and  $\frac{E_b}{N_0}$  with different encodings.

### 3.5.2 Ground segment

MESSENGER utilized the 34m DSN antenna for transmission of science data and nominal uplink, while the 70m antennas for emergency situations. The latter will be involved in the uplink design, which will be discussed in the section 3.5.5. By using a typical value of efficiency coefficient ( $\eta$ ) for the parabolic antennas equal to 0.55, the calculated results are similar to those found in literature (68.2 dB for 34m, 74.5 dB for 70m) [26]. The parameters of both antennas can be seen in Table 19.

Diameter [m]	G [dB]	$\theta$ [deg]
34	65.96	0.068
70	72.23	0.033

Table 19: Ground segment parameters.

### 3.5.3 Losses

Losses in communications between ground antennas and S/C are described below and summed up in Table 20.

**Space losses:** due to signal propagation in space. The average distance between Earth and Mercury (0.61 AU) was used.

**Misalignment losses:** due to the offset pointing between the transmitter and receiver. In this scenario, a pointing accuracy of 0.01° has been considered, with the beamwidth of the 34-meter antenna being 0.068°.

**Atmospheric losses:** due to the interaction of the signal with gases in the atmosphere and the presence of rain. A value of 0.05 dB has been assumed for these losses, which is typical for 8.4 GHz communication,

**Cable losses:** due to losses in optical connections between the components. A value of 1 dB has been assumed.

L <sub>space</sub> [dB]	L <sub>point</sub> [dB]	L <sub>atm</sub> [dB]	L <sub>cable</sub> [dB]
-270.17	-0.26	-0.05	-1

Table 20: Losses.

### 3.5.4 Downlink results

Before discussing the results, it is worth recalling the requirements that the system must satisfy. They are specified in terms of  $\frac{E_b}{N_0}$  and SNR (Signal to Noise Ratio). These values are shown in Table 21.

$\frac{E_b}{N_0}$ min [dB]	SNR min [dB]
2.5	13

**Table 21:** TTMTC requirements.

The  $\frac{E_b}{N_0}$  requirement includes a 1.5 dB margin, which is lower than the typical value of 3 dB but it is aligned with the specification provided in the MESSENGER literature [22]. As for the SNR, the required value for the DSN antenna is 10, with an additional margin of 3 dB. The link budget for the following scenarios is displayed in Table 22: the average data rate and the high data rate. The received power is calculated as the sum of the EIRP, receiver gain and losses determined in the section 3.5.3. Then the  $\frac{E_b}{N_0}$  at the receiver is obtained by subtracting the system noise and the data rate in decibel from the received power. The system noise has been calculated assuming 21 K as temperature, which is a common value for the DSN antenna. The SNR ratio has been computed using a value of 60 deg for the  $\beta$  value and a bandwidth of 500Hz. The  $\beta$  value is common for the downlink, while the bandwidth value has been chosen, due to the lack of information in literature, in order to fulfill the requirements of the SNR and it is in the range of the typical values.

Mode	P <sub>rx</sub> [dB]	$\frac{E_b}{N_0}$ [dB]	SNR[dB]
Average datarate (17.9kbps)			
Half array	-168.31	3.97	13.27
High datarate (35kbps)			
Half array	-168.31	1.06	13.27
Full array	-162.31	7.06	19.27

**Table 22:** Science Downlink Link Budget.

The SNR requirement is met in all circumstances. However, for the  $\frac{E_b}{N_0}$  the situation is different. In the case of the average datarate, it is observed that even the *half array* configuration satisfies the requirements. As for the high datarate, It can be noted that the *half array* configuration is insufficient to transfer the data while ensuring its correctness. Therefore, the utilization of the *full array* configuration is necessary, as mentioned in section 3.5.1. The *full array* mode should be used with caution since it significantly increases power consumption, which is crucial for EPS subsystem.

### 3.5.5 Uplink results

The uplink has been sized using the same general procedure adopted previously for the downlink, but with some minor adjustments to adapt to this new situation. In this case, the DSN antenna is the transmitter and the S/C is the receiver, so the system noise density will be computed assuming 293 K as the S/C temperature. The DSN antenna used is the 34 m one. Its characteristics can be found in Table 19. The X-band frequency employed for the uplink had 7.145 GHz of frequency. The transmitting power used with this type of antennas is 20 kW [26]. Regarding the space segment, a medium-gain fanbeam antenna with a 15 dB peak gain was used [31]. The encoding and the modulation schemes used are assumed to be the same as those in the downlink, as no specific information was found for the uplink. Consequently, the minimum  $\frac{E_b}{N_0}$  value remains unchanged. The datarate is set to 35 bps, compliant with Table 17. The losses encountered are identical to those computed in Table 20, except for the pointing loss. According to literature, the MGA beamwidth is 6° [31], so the pointing accuracy requirement can be assumed equal to 0.1°, resulting in  $L_{point}$  being -0.0033 dB. The SNR calculation employs the same parameters as the downlink scenario. The outcomes of the uplink link budget analysis are presented in Table 23.

P <sub>tx</sub> [dB]	EIRP[dB]	P <sub>rx</sub> [dB]	$\frac{E_b}{N_0}$ [dB]	SNR[dB]
43.01	106.52	-147.26	41.16	23.66

**Table 23:** Uplink Link Budget.

It is evident that the received  $\frac{E_b}{N_0}$  is exceptionally high, providing a substantial margin in relation to the requirements. The cause can be deduced from the use of DSN antennas. These were designed for outer space communication, enabling successful transmission to planets located even farther than Mercury (such as Mars at 1.80 AU and Jupiter at 4.20 AU). Moreover, the transmitting power is enormous (20 kW) compared to the one used by the S/C in downlink (42 W). The use of 70 m antennas further amplifies the  $\frac{E_b}{N_0}$  value (reaching 47.43 dB), thereby reducing the risk of errors in a delicate phase such as the emergency one.

## 4 ADCS Subsystem

### 4.1 Introduction

In order to accomplish survivability in Mercury's harsh environment while maintaining pointing flexibility, the MESSENGER ADCS S/S kept a three-axis-stabilized through a set of appropriate actuators, sensors and algorithms, further analysed in section 4.2. In the main processor, software algorithms coordinated sensor data processing and actuator commands as well as solar panel orientation, electronic steering for the two PAAs, and pivot positioning for the MDIS cameras. EME2000 inertial reference frame and the S/C body frame were the two coordinate systems employed by the ADCS system [32].

### 4.2 ADCS architecture

The ADCS architecture chosen for achieving primary goals will be discussed and justified in this section. The MESSENGER ADCS subsystem's main functions were to maintain and control the S/C attitude during all phases. In the MP, software algorithms coordinated data processing, sensor and actuator control to maintain a three-axis stabilized S/C and to implement desired velocity changes. There were several choices for orienting the S/C sunshade, antennas, thrusters, and research instruments at specific targets. The two solar panels' orientation was also software regulated to maintain a Sun offset angle that produces adequate power at moderate panel temperatures [7].

#### 4.2.1 Attitude determination

##### 4.2.1.1 Sensors

The sensor suite, shown in Figure 11, was made up of:

**Star trackers:** two co-boresighted star trackers positioned on the top deck and pointing out along the -Z axis provided very precise inertial attitude reference. Given that the -Y axis was always pointing to the Sun and the top deck was always opposed to Mercury when P/Ls were working, the -Z axis was pointing at the stars most of the time. The star trackers performed image processing to recognize star patterns, and the attitude solution was output to the flight software in the form of quaternion and rate. Because they were both pointing in the same direction, only one tracker was powered, with the other serving as back-up. The half-angle field of view of the star trackers was 8.2°. An "exclusion zone" angle limit of 30° was defined as will be explained in section 4.3.1 and baffles were included to protect against Mercury stray light. The two star trackers weighed 6.37 kg total. In regular tracking mode, each consumed a maximum of 12.3 W [33].

**IMU:** an inertial measurement unit equipped with four hemispherical resonance gyroscopes (HRGs) and Honeywell QA3000 accelerometers produced S/C rotation rates and accelerations. The S-SIRU included two processor boards for internal redundancy, with the second serving as a cold spare. One processor board and all four gyros were always powered, whereas the four accelerometers were only powered when performing a trajectory correction maneuver (TCM). S-SIRU weighed 6.85 kg and drew a maximum of 32 W when all gyros and accelerometers were turned on [32].

**Sun sensors:** if the primary attitude sensors failed, MESSENGER carried a set of digital Sun sensors (DSSs) to provide Sun-relative attitude knowledge. As illustrated in Figure 11, there were two independent Sun sensor systems, each consisting of a digital Sun sensor electronics (DSSE) box coupled to three sensor heads (DSSHs). Four Sun sensor heads were situated on opposite corners of the sunshade, since it always pointed towards the Sun, and two were on the back of the S/C for possible Sun pointing losses if inertial reference was lost. They were not placed close to each other in order to avoid FOV issues and to scan the entire sky. Due to the harsh environment, the heads were modified, and special filters were created to accommodate the high temperatures and intensity of sunlight near Mercury. The Sun sensors were always powered, providing two independent Sun direction readings every second at all times. These DSS systems weighed 5.93 kg (two boxes and six heads) and consumed 4.2 W [32].

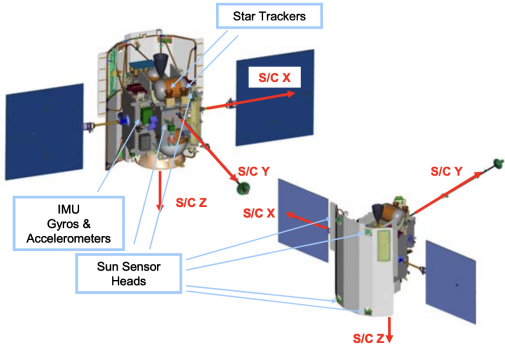


**Figure 11:** MESSENGER Guidance and Control Sensors.

#### 4.2.1.2 Attitude Determination Algorithm

The conversion of the S/C body axes to the EME2000 inertial reference frame served as the representation of attitude. The primary background guidance task computed commands at a rate of 1 Hz, and they were transmitted at the 50 Hz attitude control frequency. The attitude determination block used data from the star tracker and the gyro rate to determine the S/C's attitude and rotation rate. Before that, "sanity" checks on the sensor data were done and individual readings could be rejected in case of excessive noise or deviation from previous readings. An extended Kalman filter algorithm solved for the three attitude error states, three body rate states, four gyro biases, and three relative alignment parameters for the two star trackers (when attitude solutions from both were available) using accepted gyro measurements and the most recent valid star tracker data. When no valid tracker attitude solutions were available, the filter was not run, and attitude was propagated forward in time using any valid gyro rate readings from the latest valid attitude estimate. It must be highlighted that when running TCMs, a simpler filter was utilized to estimate accumulated velocity change from accelerometers [33].

#### 4.2.2 Attitude Control

Due to the high accuracy requested in all modes, the control logic is a 3-axis control, accomplished as described in 4.2.2.1.

##### 4.2.2.1 Actuators

The actuator suite consists of reaction wheels and thrusters, as shown in Figure 12.

**Reaction wheels:** four reaction wheels served as the main actuators to control attitude, located as in Figure 12. These RSI 7-75/601 wheels were specially adapted to have a total mass of 16.61 kg (4.2 kg each) and maximum power consumption of 80 W. All four wheels ran continuously, with a typical total power consumption of 20-30 W. Each wheel could store up to 7.5 Nms of momentum and had a maximum torque of 0.075 Nm. As indicated in Figure 12, the wheels were positioned on the S/C deck behind the sunshade. This kind of actuator was chosen because it allowed for three-axis control for detumbling, disturbance counteraction, and slew maneuvers [7].

**Thrusters:** thrusters in the propulsion system were utilized for attitude control during TCMs and momentum dumps. They may also be used as a backup method for three-axis control if multiple wheels failed. ADCS mono-propellant thrusters include twelve 4-N and four 22-N engines and were coordinated by the flight software through heaters and latch valves. The program also included a series of initiation and abort checks to guarantee correct execution and ranges [7].

**Solar array drive mechanism:** two SADAs were used to rotate the solar panels. These assemblies weighed 7.84 kg (single, internally redundant electronics box and two drives) and used up to 56 W when moving the panels. The drives could spin in two directions about the  $X$  axis via a  $228^\circ$  arc in the  $Y-Z$  plane centered on the  $-Z$  axis, so that the solar panels could be perpendicular to the Sun both in reverse and nominal Sunshield orientation. Panels were rotated in steps of  $0.02^\circ$  increments at a constant rotation rate of  $2^\circ/\text{s}$  (100 steps per second) to maintain the appropriate solar incidence angle on the cell side during all phases [7].

**Phased-array antennas drive mechanism:** the beamwidth (or field-of-view) of the two phased-array antennas was  $12^\circ$  in the  $X-Y$  plane and  $3^\circ$  normal to it. The boresight, centered in this beam, could be guided through a  $120^\circ$  arc. The antennas were positioned with boresights centered in the  $+X$ ,  $+Y$  and  $-X$ ,  $-Y$  quadrants. When necessary, the S/C was rotated about the  $Y$  axis to provide full  $360^\circ$  coverage of the Earth's direction in the  $X-Y$  plane [7].

Considering all the hardware, S/S **mass budget** reached 53.67 kg. Propellant mass for thrusters firings was already included in MPS. **Power budget** ranged from a minimum of 70.3 W in cruise, where only SRP perturbed the S/C, to a maximum of 119.7 W in Orbital phase where SRP increased due to vicinity to the Sun and planetary perturbation became relevant [34].

**Data budget** included all data from sensors, actuators and algorithm results, which supposedly increased in Orbital phase due to the heavily constrained attitude and operations, as explained in section 4.3.1, with respect to Cruise phase.

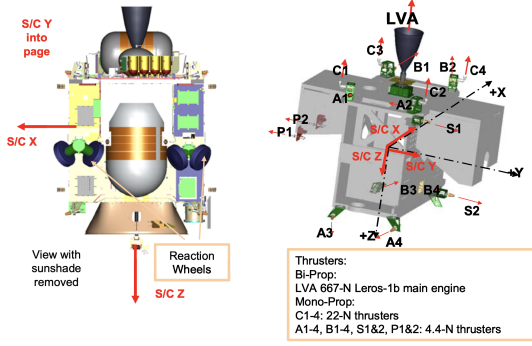


Figure 12: MESSENGER Actuators.

#### 4.2.2.2 Attitude Control Algorithm

In the 50-Hz task, the attitude control block monitored the difference between the actual and desired S/C attitude and rate and attempted to drive the difference to zero by delivering suitable actuator commands. It offered two wheel control algorithms and a single thruster control algorithm. MESSENGER computed wheel torques using a nonlinear control law. As a backup, a more standard time-optimal slew-PID control law was also available. The nonlinear algorithm was chosen as the default for wheel control. A time-optimal slew, was obtained using the slew-PID algorithm by rotating the S/C about an eigenaxis with maximum torque until a control switch line was reached, which was followed by accelerating and decelerating to reduce any overshoot. Once the attitude error fell below the threshold, control was transferred to PID logic. The alternating sign "chattering" of the torque commands could cause undue stress on the wheel hardware and could possibly excite flexible modes. Instead of following a switch line, the nonlinear algorithm eliminated this "chattering" of the commanded torques by modifying their values based on real attitude error and slew rate, with no explicit sign changes, also included a self-adjusting limiter on the proportional and integral attitude error terms. The nonlinear algorithm's primary flaw was the occasional SKI violations in case of turn with non-eigenaxis components, that was reduced through changes in the algorithm, creating a more stable torque command profile. Moreover, when all four wheels were available, the controller kept wheel speeds away from zero, adding up to a net zero torque. Instead, the thruster attitude controller was a normal phase-plane controller. The firing of thrusters was determined by the placement of switch lines in a phase-plane. Each thruster's "line of action" was defined as the direction of the torque supplied to the S/C. The switch line was set so that a thruster would be activated if it reduced either the angle or rate error. The thruster controller was utilized during momentum dumps and TCMs, and if the controller had fewer than three wheels available. The flight software monitored system momentum and could perform momentum dumps autonomously to desaturate the wheels. Passive momentum dumping with solar torque was possible by employing one of the pointing options to automatically change S/C attitude and solar panel orientation to achieve a set momentum target. This feature was employed in orbit to reduce the frequency of momentum dumps caused by thruster firings, which caused small disturbances to the S/C trajectory [35].

### 4.3 Attitude control modes

The modes description, pointing and performance are here described, together with pointing constraints and transition between modes, to justify the chosen ADCS architecture.

#### 4.3.1 Pointing constraints

A few attitude constraints were imposed to protect the S/C components from the intense heat and radiation environment of Mercury. They are listed and described in Table 24 [34].

Constraint	Description	Phases	Effect on ADCS
Sun keep-in (SKI)	Sunshade (-Y axis) oriented towards the Sun to shield internal components from solar heat flux.	Inner Cruise (< 0.85 AU) and Orbital phase.	$\pm 10^\circ$ around Z axis, $\pm 12^\circ$ around the X axis due to size of the sunshield.
"Hot pole" keep-out (HPKO)	The top deck (-Z axis) pointing away from the surface of Mercury to protect the battery and other components from albedo heat flux.	Orbital phase at 200–500 km altitude. During OCM could be temporarily disabled from ground to execute maneuver.	Angle between -Z axis and Nadir is $> 90^\circ$ .
FPAA Thermal Mitigation	Avoid reaching Front PAA operating temperature limit with melting of the soldering and high gain communication loss. FPAA was placed on +Z direction.	Orbital phase during highest thermal input: around $310^\circ$ Mercury true anomaly. To be commanded from ground.	+Z axis must not view the planet during S/C orbit true anomalies from $320^\circ$ to $60^\circ$ , to reduce the view factor to the planet during periaxis passage, also allowing radiators to point deep space.

**Table 24:** Attitude constraints and effect on ADCS.

All modes were designed to satisfy SKI and HPKO constraints at all times. The SKI constraint was the most restrictive: in fact, the commanded attitude was often on the boundary of the SKI zone to obtain the best possible orientation for the science measurements. Another more specific constraint was the star trackers exclusion zone, in which Mercury brightness prevented valid attitude determination, which was solved by placing the star trackers on -Z axis and powering them off when Mercury entered in the  $30^\circ$  exclusion zone in seasonal occurrence, usually while in downlink attitude. Finally, solar panel orientation depended on temperature, power and Sun distance: in particular, Sun offset angle ranged from  $95^\circ$  during the highest thermal input and  $80^\circ$  just after exiting the eclipse for the first two minutes [35].

#### 4.3.2 Attitude pointing and control modes

The simplest solution to satisfy all three constraint was to align the -Y axis to the S/C-to-Sun vector at a positive elevation within the SKI zone, to respect both HPKO and SKI constraints, then to command a S/C body vector to track Mercury Nadir such that FPAA constraint was satisfied. When orbit geometry allowed, it was also possible to define a pseudo-inertial pointing, aligning the +Z axis with a fixed inertial direction and the Sun vector to a specified elevation angle within the SKI zone when S/C orbit true anomaly ranged from  $320^\circ$  to  $60^\circ$ . Since most P/Ls were located in +Z direction, no scientific measurements involving Nadir pointing could be performed [36]. It is now worth discussing the needs that P/Ls applied on S/C orientation: MDIS, MLA, MASCS, and XRS were located inside the adapter ring and needed multiple orientations to collect data from the surface. GRS on the GRNS instrument occasionally also required a specific orientation. Instead, the Spectrometers of MASCS were pointed to view the exosphere around the planet limb. The fields and particles instruments (EPPS, the GRNS and MAG) were able to collect data at any orientation. The only other driver for modes definition was the PAAs pointing for downlink [35]. In order to generate sets of attitudes and commands while satisfying the constraints, a software tool named SciBox was developed. A basic pointing command was set together with an optional scan pattern command alternating fixed-rate rotations. Then the constraints applying in the current phase were specified, and if a violation was detected, the system automatically overrode the command and performed a turn back to a safe attitude [33]. SciBox made use of the pointing options available in the flight software. Common sets of attitude vectors as scenarios shortcut had been bundled together for convenience of the operations team, and are shown below, each representing a fundamental pointing mode. Additionally, two safe modes were defined to handle respectively serious and critical faults [35].

**Plus Z Pointing:** the majority of the instruments were installed on the S/C's instrument deck along the +Z body axis.

By setting the Sun as the secondary target and the secondary body axis as -Y, the +Z axis could be directed at the primary target without jeopardizing Sun safety. This primary target (aimpoint) could be any inertial target (potentially time-varying). Variability in the direction of boresight of each instrument on the deck had been allowed for.

**Nadir Pointing:** this scenario was similar to the one described in Plus Z Pointing, with Nadir as the primary objective.

The user simply needed to specify the instrument utilized for observation.

**MDIS Pointing:** this scenario was used to determine where to point the MDIS camera. In addition to reaching viewing geometries not feasible with fixed boresight devices, the MDIS enabled off-pointing the S/C in order to passively dump collected momentum using SRP. The BRV and ERRV were the -Y axis and S/C-Sun orientation in this situation.

**Double Target Pointing:** by gathering data with one of the fixed boresight instruments and the MDIS imager, the science team was able to satisfy multiple scientific goals. In this situation, a stationary boresight instrument was oriented at its targeted target, and then the scan platform in the MDIS imager was utilized to position its camera at a second target, all while keeping the Sun safe. This attitude was justified by the MDIS instrument team's desire to get images

while viewing geometries were optimized for any of the other fixed-boresight instruments. Sun safety was prioritized in this situation, which always prioritized directing the fixed boresight equipment over the MDIS imager. The reverse hierarchy, which prioritized MDIS targeting over fixed instruments, was rejected.

**Downlink Dump Pointing:** for every orbit, MESSENGER set aside 8 hours to downlink science data. In this situation, one of the two fanbeam antennas had to be oriented at the Earth while keeping the Sun safe. The fanbeam antennas had a  $15^\circ$  by  $4^\circ$  FOV but were electronically steerable along their primary axis up to  $90^\circ$ , thus their coverage nominally spanned a whole quadrant of the  $X-Y$  S/C body plane and extended by  $2^\circ$  above and below this quadrant. Despite the Sun-safety constraint, this antenna design allowed continuous connection with the Earth.

**Limb Pointing/Scans:** S/C aimed an instrument at the central body limb and scanned up and down in the radial direction in these scenarios. This scenario was separated into two parts: one in which the point on the central body surface had to align with the terminator plane, and another in which the point was determined by an azimuth reference in the S/C local horizontal plane. A limb point must meet three conditions: it must lie on the surface of the central body ellipsoid, intersect the S/C lampshade cone, and be in the plane defined by the azimuth angle. Atmospheric scans were obtained by altering the limb height linearly over time and adding this additional term along the radial direction of the current limb point. It should be noted that the limb point did creep along the surface during the scan and that the scan was performed along the radial direction, which is not the surface normal direction for the triaxial ellipsoid [36].

**Safe hold mode:** sunshade was pointed at the Sun and an MAG was pointed at Earth. Safe hold mode required inertial reference defined on board to be performed.

**Earth acquisition mode:** sunshade was pointed at the Sun and the S/C was rotated about the Sun line at  $2^\circ$  per minute. Once per revolution, a MAG swept past the Earth, and a signal was detected on ground. After observing this signal sweep several times, a command was timed to intercept and stop the rotating S/C when the MAG was Earth pointing.

The numerous list of possible pointing modes and the restrictive pointing constraints justified the great flexibility in choice of sensors: if star tracker exclusion zone was entered, attitude was propagated with gyros, and if the primary sensors were to fail, attitude would have relied on Sun sensors, which were crucial to locate the Sun even in case of loss of inertial reference.

#### 4.3.3 Pointing budget and performance parameters

MESSENGER was three-axis stabilized in all pointing modes to constantly satisfy critical pointing constraints. Attitude knowledge was required to be maintained to better than  $0.02^\circ$  and attitude control better than  $0.1^\circ$  at  $1\sigma$  (68.3%) for each axis during normal operations. More specific requirements during orbit phase, particularly referring to respectively P/Ls, sunshield, antenna pointing, are indicated in Table 25. Most values in the Table 25 are taken as general reference for reverse sizing due to the lack of literature values. N/A indicates no influence on the mode's pointing budget [36].

	Plus Z	Nadir	MDIS	Double	Downlink	Limb	Safe-hold	Earth acq.
P/L	APE< $0.1^\circ$ AKE< $0.014^\circ$	APE< $0.1^\circ$ AKE< $0.014^\circ$	$\omega < 0.8^\circ/\text{s}$	APE< $0.1^\circ$ AKE< $0.014^\circ$	N/A	APE< $0.1^\circ$ AKE< $0.014^\circ$	N/A	N/A
TCS	APE< $0.5^\circ$	APE< $0.1^\circ$	APE< $0.1^\circ$	APE< $0.1^\circ$	APE< $0.1^\circ$	APE< $0.1^\circ$	APE< $0.1^\circ$	APE< $0.1^\circ$
TMTC	N/A	N/A	N/A	N/A	APE< $0.01^\circ$	N/A	APE< $0.01^\circ$	N/A

Table 25: Pointing budget per mode and subsystem in Orbital phase.

It can be noted that P/Ls pointing imposed the most knowledge accuracy as expected from the precision required from scientific measurements. Moreover, AKE is in all cases smaller than APE since pointing knowledge was critical to relate scientific measurement with the point of measure. TCS related sunshade pointing was a critical constraint, so it was mandatory to be observed in all modes, including safe modes. P/Ls scientific pointing lost priority during safe modes due to severe/critical faults. During Earth acquisition mode, no minimum performance parameter was set for TTMTTC related antenna pointing, since the mode involves loss of inertial reference. Pointing stability imposed on most instruments was  $\pm 0.003^\circ/\text{s}$  peak-to-peak. Rotation rate under  $0.8^\circ/\text{s}$  can be considered as a general requirement for rotation rate and scan pattern commands. Drift limitation in terms of KDE and PDE can be taken as one order of magnitude less than AKE and APE respectively for a conservative design. Additionally, MDIS cameras pivot platform's rotation rate stayed around  $1.1^\circ/\text{s}$  and AKE <  $0.004^\circ$ . Moreover, solar panels were rotated in steps of  $0.02^\circ$  at a constant rate of  $2^\circ/\text{s}$ . Reaction wheels and thrusters were chosen as actuators since capable of satisfying the pointing budget in all cases, guaranteeing wheels desaturation and back-up control in case of multiple wheels failure. Sensors can be related and sized to the AKE they shall have guaranteed during all modes: star sensors can easily guarantee AKE of  $0.014^\circ$  during all nominal modes being extremely accurate, and so can do the gyro, since the small fraction of time star sensors could not be available due to Mercury entering exclusion zone did not accumulate significant drift. Finally, fine sun sensors could locate the Sun accurately also during safe modes, considering that knowledge can be degraded in case of inconsistency with Sun ephemeris, as explained in section 4.3.4.

#### 4.3.4 Transition between modes

The various pointing options for scientific observation and data transmission can be generally defined as Operational modes. Recoverable faults in non-critical subsystems were handled in Operational mode by turning off the component. Any serious fault affecting a critical S/C subsystem without loss of inertial reference resulted in remedial action (bringing a backup system on-line) and entry into safe-hold mode. The Earth acquisition mode was the lowest safing mode and it was entered in case of loss of inertial reference, for example, when switching between redundant MPs. Recovery from safe hold or Earth acquisition mode required the on-board problem to be diagnosed and corrected by mission operations team. Only ground command could promote back to operational mode. It is possible to identify particular conditions associated with ADCS subsystem triggering request of demotion to safe-hold mode. If the ephemeris data indicating the Sun direction were not consistent with the Sun sensor readings, the precise models were declared invalid, the S/C started using the coarse models as a backup, and demotion to a safe mode was requested to satisfy SKI constraint. Moreover, if CMDs were not commanded from ground, the S/C autonomously executed desaturation (AMD), triggering a safe-hold demotion. Demotion to a safe mode was additionally requested if a constraint violation was detected, for 5 1-Hz cycles for SKI, and for 30 1-Hz cycles for HPKO [34].

### 4.4 Preliminary sizing

In following sections the design process of the ADCS S/S will be outlined. Firstly, a brief overview about the disturbances in the MESSENGER orbit will be given. Subsequently, the focus will be on the design of the reaction wheels and the thrusters.

#### 4.4.1 Perturbations

There are four attitude perturbations that need to be analysed: solar radiation pressure (SRP), gravity gradient (GG), magnetic and aerodynamic disturbance. In the special environment of Mercury some of those had a significant impact on the S/C, while others could be neglected. The value of the disturbances for the MESSENGER mission can be see in Table 26.

**SRP:** the main source of disturbance in the mission due to the significant solar irradiation experienced in the inner cruise. However, this effect could also be exploited to make some slew and desaturation manoeuvres, as explained in section 4.2.2.2. To model this effect, a value of  $9116.4 \text{ W/m}^2$  was used as solar constant at a distance of 0.6 AU. The reflectivity coefficient selection was based on the worst case scenario, corresponding to that of the solar panels, with a value of 0.52 [37]. The distance between the center of solar pressure and the centre of gravity was assumed to be 0.03 m. Since the S/C was quite symmetric from the Sun viewpoint, there is no justification for choosing a higher value. Further explanations will be reported in section 4.4.2. The area exposed to the Sun was calculated including solar panels and the sunshade, modeled as flat plates.

**GG:** the second most intense disturbance. S/C's geometric and mass properties were required in order to define the inertia matrix. The S/C body dimensions were measured to be 1.27 m x 1.42 m x 1.85 m, while the solar panel measured 1.54 m x 1.75 m [38]. The inertia matrix of the whole S/C was calculated by including the S/C body and two flat plates for the solar panels. Each body's inertia matrix was computed at its geometric center and then relocated to the S/C's center using the transport theorem. The masses used for these calculations are 1093 kg for the S/C body , representing the worst case scenario under wet conditions, and 17.06 kg for each solar panel [38]. The maximum deviation for the Z axis from the Nadir ( $\theta$ ) was assumed to be  $12^\circ$ , compliant with the SKI zone requirement, as mentioned in section 4.3.1. GG was characterized by the orbital parameters of the S/C orbit around Mercury.

**Magnetic:** according to literature, the magnetic field of Mercury has a mean value of 300 nT [11]. A value of  $0.01 \text{ Am}^2$  has been used for the internal dipole, which represents a worst case scenario.

**Aerodynamic:** negligible in this case because of the Mercury's thin and rarefied atmosphere.

$T_{\text{SRP}} [\text{Nm}]$	$T_{\text{GG}} [\text{Nm}]$	$T_{\text{magnetic}} [\text{Nm}]$	$T_{\text{aero}} [\text{Nm}]$
$1.44 \times 10^{-5}$	$4.08 \times 10^{-6}$	$3.00 \times 10^{-8}$	-

**Table 26:** Disturbances overview.

It can be noted that the SRP and the GG were the most relevant perturbations during the orbital phase. The magnetic disturbance was several orders of magnitude less than others, so it has been neglected. Only the SRP was present during the interplanetary phase, so the other disturbances that may arise during the flybys were neglected due to their short duration.

#### 4.4.2 Reaction wheels design

The S/C was equipped with a pyramid configuration consisting of four reaction wheels. This configuration evenly distributed the torque such that it was not concentrated in a single point. The RW tip of the pyramid was on the Z axis, thus generating

a torque primarily on this axis, which was thought to be the one that needed more control due to thermal and P/L pointing constraints. RW were located symmetrically with respect to the Z axis, as shown in Figure 12, so that their weight was balanced. RW properties can be seen in Table 27 [7]. To ensure momentum storage, the saturation limit is set based on the value of a single reaction wheel. This is the most conservative, in fact it prevented one wheel to become saturated while the others were continuing to function properly.

$h_{\max}$ [Nms]	$T_{\max}$ [Nm]
7.5	0.075

Table 27: RW parameters.

The objective is to find out how often wheels needed desaturation and assess their capability for conducting slew maneuvers. Firstly, the major disturbances are summed up and a margin of 100% is applied. It was determined that the maximum momentum storage was reached after 4 orbits. Consequently, desaturation occurred approximately every 2 days, similarly to the literature value of 3.5 days as a closest case, considering a momentum threshold of 7 Nms [37]. The disparity between the two values could be attributed to the assumption of considering the wet mass of the S/C. As a matter of fact, while orbiting around Mercury, the S/C was lighter since a substantial amount of fuel was spent in previous phases. Furthermore, the value used for the calculation includes a 100% margin. The fact that the desaturation was not excessively frequent confirms that the S/C was capable of withstanding the disturbances and ensuring the needed pointing accuracy. Moreover, the disturbances were nearly the same in every mode because the S/C attitude was strongly constrained by the SKI and HPKO requirements. For the slew manoeuvre, a rotation by 180° around the Z axis has been analysed, which represents a flip flop manoeuvre. To ensure compliance with the constraints specified in Table 25, a maximum angular velocity of 0.5°/s is chosen. This value not only satisfied the constraint imposed by the MDIS but also provided a comfortable margin. With these requirements, the torque necessary for the slew is calculated to be 0.0495 Nm, which is below the maximum limit allowed by the reaction wheels. Therefore, the maneuver can be executed at this rate without encountering any issues. Figure 13 illustrates the torque needed to realize the manoeuvre in a given time. The horizontal line represents the maximum torque permitted by the reaction wheels, and the vertical line represents the minimum slew time imposed by the maximum speed constraint.

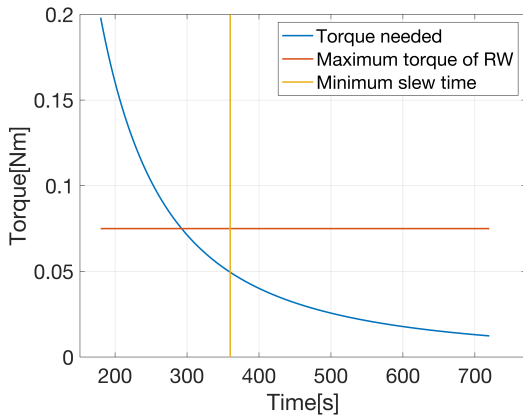


Figure 13: Torque for the slew maneuver as a function of time required.

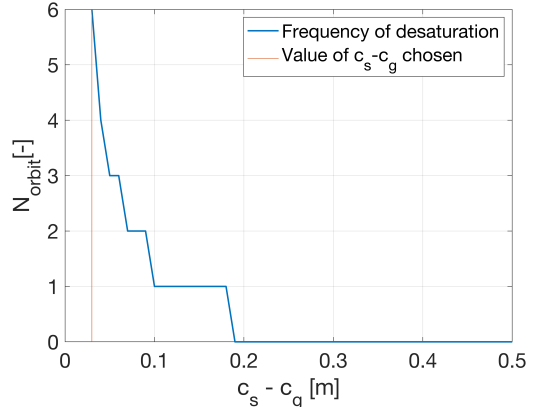


Figure 14: N. orbits to desaturate based on  $c_s - c_g$ .

In the computations explained before, a minimum slew time of 360 s was obtained, resulting in a solution that corresponds to the intersection between the blue and yellow lines depicted in Figure 13. In Figure 14, it can be seen how the number of orbits between each desaturation varies depending on  $c_s - c_g$ . Only SRP disturbance with a 100% margin is considered. This plot supports the hypothesis that the value of 0.03 for  $c_s - c_g$  (vertical line in the plot) corresponds to a frequency of desaturation that is consistent with that seen in the literature. Similar numbers had to be taken into account by MESSENGER engineers at the preliminary design stage, otherwise, the reaction wheels would not have been able to control the S/C since desaturation would have occurred too frequently. If the GG in Figure 14 was considered, the blue line would fall, making the issue worse.

#### 4.4.3 Thrusters design

In the MESSENGER mission, the primary purpose of the thrusters was to desaturate the reaction wheels. However, in the event of one or more reaction wheels failing, the thrusters were capable of fully controlling the S/C. A requested torque could be generated by activating a combination of two thrusters of the A, B or C type. A and B thrusters were able to generate torque around any axis and had the same thrust value of 4.4 N, thus the C thrusters will not be considered in this discussion. In the calculations, it will be assumed that only two thrusters performed the desaturation and the slew. The initial step involves calculating the required time for desaturation. The resulting time is 1.34 s and it is insufficient

compared to the minimum time required for the maneuver, which is typically at least 5 s. This limitation is implemented to avoid extremely short-duration maneuvers that are difficult to execute. By setting the desaturation time as the minimum time, the force required from the thrusters can be calculated. Finally, the mass of propellant necessary for the maneuver has been determined. For the slew maneuver, a similar process has been followed. The force required for the slew is computed, with the force's moment arm corresponding to half of the S/C's width. This not only represents the worst-case scenario as the width is the minimum length, but it also holds physical significance as the flip-flop maneuver is executed around the Z axis. The previously calculated torque for the reaction wheels is used to determine the required torque for the slew. The propellant mass required for the maneuver is estimated by assuming the same duration as computed for the reaction wheels. Finally, to determine the total propellant mass required by the ADCS, the propellant needed for desaturation and maneuvers is summed up. The desaturation manoeuvres are assumed to occur exclusively during the nominal orbital phase (1 year). This assumption is valid because only 6 momentum dumps were done during the interplanetary phase, while during the nominal orbit phase 39 dumps were performed. As for the slew maneuvers, it has been assumed that a minimum of five flip-flop maneuvers were executed throughout the mission, as stated in literature [8]. To provide some margin, a value of eight flip-flop maneuvers has been selected. By considering these factors, the total propellant mass required has been determined. The results of the thrusters sizing are shown in Table 28.

$F_{\text{desat}}[\text{N}]$	$F_{\text{slew}}[\text{N}]$	$m_{\text{desat}}[\text{kg}]$	$m_{\text{slew}}[\text{kg}]$	$m_{\text{tot}}[\text{kg}]$
1.18	0.039	0.0027	0.0065	2.03

**Table 28:** Thruster sizing results.

In Table 28 the force required for desaturation and slew maneuvers, the propellant mass required for a single desaturation and for a single slew maneuver, and the total propellant mass needed to execute these maneuvers throughout the mission are presented. The total mass of propellant corresponded to 3.4% of the mass needed for the monopropellant mode. While this percentage may appear small, it's important to note that this sizing does not take into account the TCM manoeuvres or those conducted by the C thrusters. The CMD manoeuvres needed a  $\Delta V$  which was in the orders of millimeters per second, while the TCM or OCM could be of several meters per second.

## 5 TCS Subsystem

### 5.1 Introduction

The TCS goal was to keep all systems and P/Ls onboard the S/C at their operational temperatures for the duration of the mission. To tackle the engineering difficulty of handling high temperature changes during the cruise and orbital phases of the mission, the S/C design contained a huge sunshade, which was the main TCS solution, but not the only one. The design and configuration of this S/S imposed severe limits on all other S/S, including ADCS and EPS.

### 5.2 TCS Architecture

Because of Mercury's hostile thermal environment, using only a passive control was not an option [39]. Using solely an active control, on the other hand, would have necessitated an exceptionally high power budget for the TCS S/S. As a result, the two approaches were combined, as depicted in [Figure 15](#), and successfully met all thermal challenges encountered.

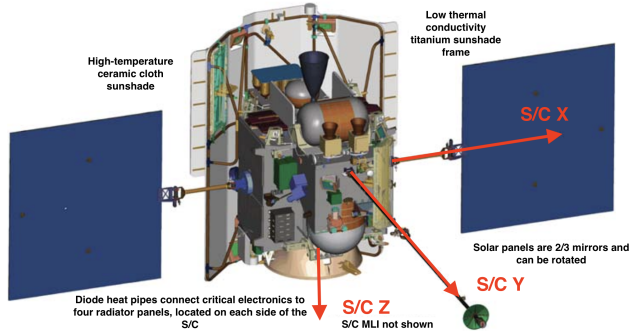


**Figure 15:** MESSENGER S/C with thermal control design highlights [2].

#### 5.2.1 Passive control

##### 5.2.1.1 Sunshade

During the inner cruise and orbital phases, the MESSENGER's thermal design depended on a ceramic-cloth sunshade composed of aluminized Nextel 312-AF 10 and multi-layer aluminized Kapton, characterized by low  $\alpha$ , high  $\varepsilon$  and low conductivity, to protect the S/C from the harsh solar environment of the inner solar system [40]. The ceramic cloth was rated in excess of 1000°C. When Mercury was at its perihelion, the sunshade reached a maximum temperature of 325°C and a 400°C temperature difference existed between the sunshade and the S/C. When oriented with the -Y axis toward the Sun, the sunshade generated a benign thermal environment for the main S/C bus, permitting the use of normal electronics, components, and thermal blanketing materials. The sunshade construction also served to provide support for the high-temperature MLI blanket, and also to support four DSS, one of the PAA and three LGA assemblies and two thrusters.

##### 5.2.1.2 MLI and radiators

Except for radiators and apertures, the S/C electronics were totally covered with MLI, which protected and insulated the core S/C from direct solar radiation while it was within 0.95 AU. Although complete S/C coverage with MLI seemed appealing in terms of heater power and coupled thermal mass, it was not practicable, therefore electronics boxes dissipating more than 20 W had specialized radiators. There were four radiator panels oriented orthogonal to the direction of the Sun, one on each side of the S/C. Radiators kept the attached electronics boxes cool and, along with MLI heat leaks, helped to keep the rest of the S/C at safe temperatures. The battery frame, for example, was thermally insulated from the S/C deck and conductively connected to a space-facing silver-Teflon covered radiator with an area of around  $0.13 \text{ m}^2$ . It should be mentioned that silver-Teflon is a material with exceptionally high emissivity and low absorptivity, making it ideal for use as a radiator [41].

##### 5.2.1.3 Material and configuration solutions

Certain hardware (solar panels, sunshade, phased-array and low-gain antennas, and DSS heads) were constantly exposed to the Sun throughout the mission. These components were designed to operate in the worst-case scenario at Mercury perihelion and during orbits that cross over one of Mercury's hot poles, thus withstanding the temperatures and solar flux input experienced at 0.3 AU [38].

**Sunshade frame:** because the sunshade reached extremely high temperatures, it had to be insulated from the remainder of the S/C. It was accomplished by developing a low thermal conductivity titanium sunshade frame.

**DSS:** high-temperature adhesives, comparable to those on MESSENGER solar arrays, have taken the place of the lower-temperature adhesives used in normal designs. The significantly newer thermal component of the Sun sensor, however, was a specific solar attenuating filter over each head to minimize incident solar intensity by an order of magnitude.

**Antennas:** all Sun-facing antennas were protected by custom-made high-temperature and RF-transparent Nextel radomes. The antenna feed assembly was soldered with SN63, which has a melting temperature of 180°C. The antenna was placed on the -X side of the sunshade. It was theorized that excessive IR induced by heat flux along the -X and lesser +Z directions was trapped between the S/C and sunshade, contributing to an increase in RF connector temperature.

**Solar panels:** the solar panels were designed to withstand solar irradiation at normal incidence at the 0.3 AU perihelion. Thermal control of the solar arrays was achieved by combining a 2:1 packing factor ratio of OSRs to triple-junction GaAs solar cells to reduce panel absorbance, as described in section 5.2.2.3. Off-tilting from the normal Sun direction is used to decrease input heat. The panel substrates were aluminum honeycomb 18 mm thick with RS-3/K13C2U composite face sheets. The graphite-cyanate-ester materials used on the panel face sheets were chosen for their high thermal conductivity. The front cell side of the panel was insulated with 0.05 mm Kapton, which was co-cured with the graphite fiber face sheet. The back face sheet was covered with 30.5 cm × 30.5 cm sheets of co-cured square-shaped aluminized Kapton. The aluminized Kapton was utilized to reduce the absorbance of the solar panel's backside to that of the solar cell-OSR side. Thus solar panels could withstand sunlight with normal incidence to either side during Sun's closest approach. Heat was allowed to diffuse across the face and through the rear of each panel by applying cells and mirrors in alternating parallel rows, enabling steady-state survivability at every Sun angle at any solar distance.

**P/Ls and sensitive components:** During Orbital phase, the S/C was approximately 30 minutes between the Sun and the planet. The sunshade shielded the S/C from direct solar illumination during this time, but the rear of the S/C was exposed to the scorching Mercury surface. Components like the battery and star trackers were placed in such a way that the S/C body blocked a significant section of the planet view, reducing direct radiation from the planet surface. To operate fully during this hot transient period, planet-viewing instruments such as the MDIS required a particular thermal design. The PC board was designed with eight layers with components on both sides. The board was mounted to a 0.125-cm aluminum (6061-T6) housing in twelve places. To connect the heat load directly to the base plate, high-thermal-dissipation components were attached to an aluminum heat sink bonded to the bottom side of the board. The PDU thermal control was a passive thermal conduction architecture, with each electrical slice having an own thermal channel to the heat sink. All PDU circuit boards relied on interior copper layers to transport heat generated by electronic components to the heat sink. A 0.5-mm-thick Choseal 1285 gasket was put between the electronic modules and the heat spreader to improve thermal transfer between the slices and the heat spreader.

## 5.2.2 Active control

### 5.2.2.1 Heaters

MESSENGER relied on heater power to keep components within allowed flight temperature limits. Since almost half of the S/C launch mass was propellant, the propulsion system was the major user of heater power. The temperature of the battery was controlled by two redundant heater circuits, each of which was independently controlled by a single mechanical thermostat. When the S/C was approaching 1 AU in reverse-sunshade orientation, the battery was kept at less than 0°C using trickle charge and a little amount of heater power [42].

### 5.2.2.2 Diode heat pipes

High-power S/C electronics requiring dedicated radiators could not be packaged in the same way as the battery to reduce Mercury-related environmental heating. Instead, these electronic boxes required a unique thermal design to operate during orbital phase. When radiator surfaces were exposed to dayside heating from Mercury, diode heat pipes were employed in both the S/C and imager thermal designs to protect the associated components. In fact, diode heat pipes successfully ceased conducting when the radiator surface became hot and resumed conduction when it cooled, restoring normal thermal regulation. The PSE, PDU, and SAJB, for example, were all temperature controlled by diode heat pipes connected to aluminum honeycomb radiator panels positioned on the +/- X sides of the S/C [38].

### 5.2.2.3 Attitude control

**Sunshade pointing and "flip-flop" maneuver:** When the S/C-Sun distance was less than 0.95 AU, the S/C attitude control oriented the sunshade toward the Sun at all times. When the sunshade was aimed at the Sun but there was no heat from Mercury's surface, high heater power was required. A mission-critical design feature of MESSENGER was the ability of the S/C to be "flipped" so that the anti-Sun side could be illuminated (configured to fly with the sunshade pointed away from the Sun) in order to reduce heater power consumption and allow the use of a smaller size

solar array while maintaining good solar array power margin. This functionality allowed MESSENGER to comfortably work between 0.95 and 1.08 AU and allowed unrestricted outer solar distance flexibility [38].

**Antennas protection:** Because the phased array was not transmitting and the attitude-dependent instruments were not collecting data during the hottest points of the IBS orbits (one of the hot seasons of the S/C orbit), the plan to protect the antenna from damage caused by temperatures above 200°C was to reduce the  $-X$  and  $+Z$  view of the planet during a window around periapsis passage. A roll of 60° S/C around the  $Y$  axis (Sun line) was studied. The  $-X$  and  $+Z$  thermal environments as viewed by the antenna were sufficiently decreased by biasing  $+X$  toward the planet to protect the antenna from thermal damage. During each orbit, the RF off-pointing lasted 25 minutes, successfully attenuating the high heat from Mercury on the antenna while directing the  $+X$  side of the S/C to a near nadir attitude, prompting the  $+X$  diode heat pipe radiator panels to activate [43].

**Solar panels protection:** Thermal management of solar panels was achieved by tilting the panels away from normal incidence with increased solar intensity. As the S/C approached the Sun, the solar arrays were turned to operational angles based on the power thermal model projections. The two solar panels were kept facing the Sun until the panel temperature reached a predetermined level (maximum 150°C). The SADA rotated the panels to keep the temperature at the preset level while still providing the necessary S/C power. As the panel temperature decreased below the limit threshold and more power was required, the panels were turned toward normal incidence. The two S/A wings were rotated to the identical incident Sun-angles in order for them to operate at the same temperature [44].

## 5.3 Thermal environment analysis per phase

### 5.3.1 External heat fluxes

The external heat fluxes encountered by the S/C strongly varied across phases of the mission, and were a fundamental driver of the entire mission design. Consequently, external fluxes are here analyzed per each phase and related to TCS design choices.

**LEOP:** from launch until June 2006, there were prolonged periods when the mission trajectory achieved solar distances  $>0.95$  AU, with heat flux very close to the ones experienced on Earth. The S/C was flown in the reverse-sunshade orientation to reduce heater power usage to nearly zero and allow for large power margins while maintaining component temperatures within their allowable flight limits [44].

**Cruise phase:** during outer cruise phase ( $>0.85$  AU), the S/C experienced similar fluxes with respect to LEOP. The inner cruise phase ( $<0.85$  AU) began when MESSENGER was transitioned into the nominal sunshade-to-Sun orientation due to the decrease in Sun distance and increase of solar flux. The S/C approached the Sun at Mercury perihelion distance a dozen times before orbit insertion, showing stable and satisfying temperatures. No significant albedo or IR radiation was present in deep space due to the absence of planets in vicinity of the S/C, apart from brief fly-bys encounters which were relatively benign when compared with the environments expected during the orbital phase [39].

**Orbit phase:** Mercury's highly eccentric 88 days heliocentric orbit caused the solar flux to vary between  $6467.2\text{ W/m}^2$  at aphelion (0.46 AU) and  $15273.6\text{ W/m}^2$  at perihelion (0.30 AU), respectively 4.7 and 11.1 times the nominal solar constant at Earth. Mercury's surface absorbs between 90% and 94% of the incident solar radiation, reflecting the remaining percentage as albedo flux. Mercury rotates once every 59 days, causing the planet surface temperature to reach steady temperature conditions. Mercury has a high surface emissivity (around 0.93, varying slightly with location), has virtually no atmosphere, causing planet surface temperatures to be very hot on the sunlit side of the planet (up to 451°C at the subsolar point near perihelion) and very cold on the dark side of the planet (-163°C). IR thermal environment is extremely harsh, with significant changes depending on S/C true anomaly, reaching a maximum incident flux of  $5504\text{ W/m}^2$  on  $+Y$  face, almost 12 minutes after periapsis passage, supposedly corresponding to Mercury equator during daylight and its highest surface temperature. Orbital perturbations changed the location of the orbit periapsis relative to the sub-solar point, causing the first hot season, when S/C passed between Mercury and the Sun, in each Mercury year to gradually become hotter, because periapsis moved northward and eventually switched to the dayside of the planet during this season, and the second hot season to become less hot. The orbit average heating values increased slightly with successive Mercury years because of the decrease in orbit period and a general lowering of the periapsis altitude, up to S/C performing OCM resetting the initial orbital parameters [44].

TCS architecture and interfaces with other S/S were designed to be able to adapt to different thermal environments experienced in different phases. Sunshade protected the S/C from solar flux during orbital and inner cruise phase, but its orientation was inverted in outer phase, showing flexibility in managing both cold and hot conditions and strong interaction with ADCS S/S. MLI is used to decouple the internal S/C from the external environment, reducing heat input during hot case and avoiding internal heat irradiated towards deep space in coldest cases. The choice of materials notwithstanding the highest temperatures, as explained in section 5.2.1.3, was another crucial design variable of TCS strongly related to the scorching thermal environment. Solar arrays, sunshade, DSSs, and PAAs have been designed to operate throughout the Mercury year

and also during orbits that cross over one of Mercury's two "hot poles" that face the Sun at Mercury perihelion. Finally, diode heat pipes avoid transmitting external heat to the internal S/C through the radiators when ADCS was not able to point deep space because of pointing constraints and the intense heat fluxes impacting on the radiators [43].

### 5.3.2 Internal heat fluxes

A substantial heat contribution came from the dissipation of internal components. In order to size TCS for worst hot and cold case scenarios, the on-board power dissipation is set equal to the power budget in different phases, shown in [Table 29](#) [38].

Outer cruise	Inner cruise	Orbit	Eclipse > 35 min	Eclipse < 35 min
247.8 W	382.7 W	597.4 W	284.6 W	332.3 W

**Table 29:** Power budget as internal heat dissipation per phase.

The highest internal heat dissipation was reached in Orbit phase for all S/S, especially for P/Ls due to the beginning of scientific phase, and TTMTTC due to higher downlink data volume. Heating power for tanks and propulsion subsystem was a substantial fraction in all phases with a peak in inner cruise due to the higher numbers of maneuvers performed. Least power was dissipated during outer cruise thanks to reverse-sunshade orientation which reduced heaters usage, and to the telemetry-only low data volume to downlink. During eclipses power request was significantly decreased because of the lower power availability and limit in maximum depth of discharge, for all S/S but Guidance and Control, which needed to be fully operative to perform maneuvers and keep the thermally critical attitude constraints. An important contribution to internal heat flux in all phases was heaters. Their utilization was relatively low during outer cruise, but once the sunshade was pointed to the Sun, screening the S/C from solar flux, heaters power became first necessary and then progressively decreased with the hotter environment. For instance, battery heaters duty cycle ranged from 100% at 0.65 AU to 34% at 0.31 AU. The S/C electronics were mounted to the composite structure and, except for radiators and apertures, were completely covered with MLI. Electronics boxes dissipating more than 20 W had dedicated radiators to dissipate internal heat excess into space [42].

## 5.4 Components thermal control and temperature limits

Temperature limits of the most relevant components are listed in [Table 30](#) and compared to the actual performance data during different phases. Temperature limits and eventually related to the adoption of thermal control strategies [43].

Component	Inner Cruise performance [°C]		Outer Cruise performance [°C]		Temperature limits [°C]	
	Hot	Cold	Hot	Cold	Hot	Cold
Case						
MLA	14	-14	15	-13	40	-20
MDIS	-12	-40	-8	-38	50	-48
RW	41	12	53	22	75	-15
IMU	8	-9	24	4	60	-24
DSS (-Y)	144	-35	100	39	190	-75
Tanks	31	14	32	18	60	2
Solar Panels	125	9	22	-4	240	-145
Batteries	-1	-6	1	-5	20	-10
FPAAs (-Y)	46	-55	91	8	155	-90

**Table 30:** Temperature limits and performances per component.

Inner and outer cruise had generally similar temperatures performance for most components since the heat which was provided by the Sun in outer cruise, was compensated by heaters in inner cruise when sunshade was shielding the Sun. The widest temperature limits belonged to components in the -Y face, in the direction of the sunshade, which were expected to undergo the highest heat fluxes, despite being protected respectively by a filter for DSS and a randome for the FPAAs. The most stringent coldest limit belonged to the tanks, which request the most power from heaters to avoid propellant freezing, while the most stringent hottest limit belonged to the battery. Generally, the TCS approach for external components was combining wide temperature range components and materials, configuration choices and attitude constraints as for SKI to point the Sun, HPKO to protect the battery from albedo flux, and FPAAs thermal mitigation attitude. For internal components a combination of heaters and radiators with diode heat pipes allowed to obtain a stable equilibrium temperature, protected from the external fluxes by MLI. TCS power budget of the mission included heaters and thermal sensors, ranging from a minimum of 10.2 W in outer cruise up to a maximum of 62.2 W in inner cruise. The calculated heater power in section 5.5 during cold case is significantly higher, which can be due to the inability of the model to capture local behavior of heaters. Mass budget includes heaters, radiators, diode heat pipes, solar panel and antenna protection, DSS filter and sunshade to a total of 52.2 kg [45].

## 5.5 Preliminary sizing

### 5.5.1 Mononodal analysis

A mononodal analysis was carried out to verify the acceptability of the steady-state temperature reached by the S/C. The battery temperature limits ( $-10^{\circ}\text{C} / 20^{\circ}\text{C}$ ), that can be seen in [Table 30](#), were imposed in this case although the strictest coldest limit is the one of the tanks, which are however controlled by dedicated heaters, whose local effect on tanks cannot be captured by mononodal analysis and would result in a cold case oversizing. No margins were applied to these values as they are taken from after-launch literature, belonging to components that actually flew. The mononodal analysis approximate the S/C to an equivalent sphere. In this model, only the S/C body area has been considered, neglecting the sunshade and the solar panels. A mononodal analysis was performed specifically for the solar panels and will be shown later in this section. The effect of the sunshield is modelled as a reduction in incoming heat flux on the S/C by an estimated amount producing suitable radiators and feasible temperatures. In the hot case the S/C was at the pericenter of the orbit and was subjected to all kinds of heat fluxes: internal heat produced by the components, heat from the Sun, and IR and albedo fluxes coming from the planet. This is an extreme case due to the high IR fluxes from the planet caused by the high planetary temperature, as well as the extreme closeness to the sun (0.4 AU). The numerical values of the incoming heat fluxes can be seen in [Table 31](#).

	$q_{\text{sun}} [\text{W/m}^2]$	$q_{\text{IR}} [\text{W/m}^2]$	$q_{\text{albedo}} [\text{W/m}^2]$	$Q_{\text{internal}} [\text{W}]$
<b>Hot case</b>	8547	1362	730	597.4
<b>Cold case</b>	1367	0	0	247.8

**Table 31:** Heat sources in hot and cold case.

Results are satisfying in both the radiator's area and the temperature reached by the S/C only in the case in which the sunshield is able to block 99.9% of the incoming solar flux, 90% of the albedo flux and 88% of the IR flux, which is a rather strong assumption: therefore the actual effect of the sunshade will be better modeled in section [5.5.2](#). For the S/C,  $\alpha = 0.12$  and  $\varepsilon = 0.03$  were used for Kapton MLI [46], as stated in section [5.2.1.2](#). For the radiators, a value of  $\varepsilon = 0.88$  has been taken for the emissivity, typical for OSRs. The results of the analysis can be seen in [Table 32](#). As for the cold case, after some simulation, it was clear that the worst cold case occurred during the outer cruise phase, where the S/C was at 1 AU and subject only to the internal heat and Sun irradiance. The values of these fluxes can be seen in [Table 31](#). The eclipse does not represent a cold case due to the high IR fluxes of Mercury. Moreover, eclipse could not be obtained when near apoapsis because of high altitudes, which would have significantly decreased fluxes. For the internal heat, it has been considered that all the power budget was dissipated into heat. The results of the cold case can be seen in [Table 33](#).

$T_{\text{S/C}} [\text{C}^{\circ}]$	$A_{\text{radiators}} [\text{m}^2]$
20	3.33

**Table 32:** Parameters in hot case.

$T_{\text{S/C}} [\text{C}^{\circ}]$	$Q_{\text{heaters}} [\text{W}]$
-10	75.11

**Table 33:** Parameters in cold case.

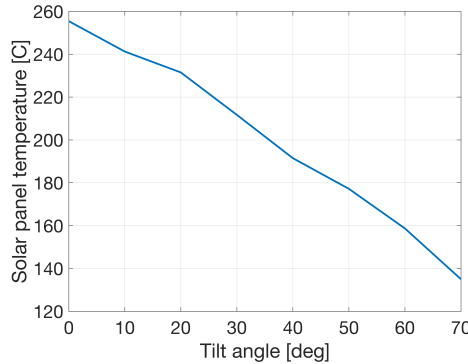


**Figure 16:** Solar panel temperatures as function of the tilt angle.

Solar panels were modeled as flat plates. Their optical properties have been calculated by a weighted average of the Kapton and OSR properties [47], as stated in section [5.2.1.3](#). The heat sources are the same of the S/C hot case; the only difference is that the internal heat has been calculated with the power needed by the S/C and the efficiency of the solar cells. An important difference with respect to the S/C node is that the solar panel could rotate to reduce the incoming flux and cool down, this possibility has been included in the model and the outcomes can be seen in [Figure 16](#). When the solar panel was

at  $0^\circ$  the temperatures were higher than the admissible stated in [Table 30](#). When the temperatures became too high the solar panel progressively tilted the front face away from the Sun to cool down. Between  $60^\circ$  and  $70^\circ$ , which was the typical tilting angle used throughout the Orbital phase, the temperatures were in the operative range for the mission, under  $150^\circ\text{C}$  [38].

### 5.5.2 Multinodal analysis

Since mononodal thermal model is by nature unable to fully capture the thermal behavior of the sunshade and its interactions with the S/C bus, a multinodal model analysis, shown in [Figure 17](#) and [Figure 18](#), was performed to better analyse the joint action of the adopted control strategies. The model consists of four nodes: the sunshade and the two solar arrays as flat panels, and the main bus as a sphere. All nodes are connected through conduction from the sunshade and solar arrays to the bus by the structural support made of titanium to prevent the huge fluxes impacting on the extended surfaces to reach the S/C. View factors with Mercury are calculated considering S/C at periapsis and the planet as an homogeneous sphere.

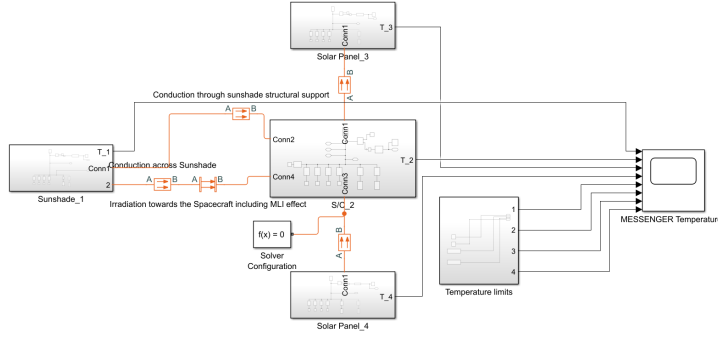


**Figure 17:** Overview of the Simulink model.

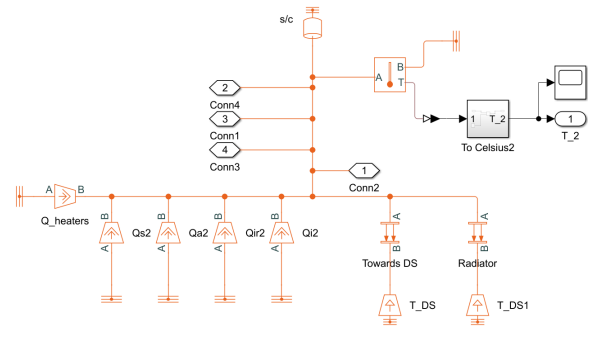


**Figure 18:** Nodes modelization in Simulink.

The interaction between sunshade and S/C bus is additionally modeled through a conductive resistance simulating heat across the sunshade reaching its internal surface, which irradiates supposedly 70% of heat towards the S/C bus. To decrease thermal input on the bus, the internal surface is supposed covered by a low emissivity coating. The heat reaching the S/C is then ultimately decreased by the presence of MLI. Since the model allows a better characterization than mononodal analysis, an even worse hot case scenario was analyzed: maximum Sun heat flux at Mercury perihelion (0.3 AU) equal to  $15273.6\text{W/m}^2$ , maximum IR flux of  $4307.45\text{ W/m}^2$  and maximum albedo factor of 10%, the whole maximum power budget dissipated on board. The same cold case scenario of mononodal model was considered. Results are shown in [Table 34](#).

	$T_{\text{sunshade}}[\text{ }^\circ\text{C}]$	$T_{\text{S/C}}[\text{ }^\circ\text{C}]$	$T_{\text{arrays}}[\text{ }^\circ\text{C}]$	$A_{\text{radiators}}[\text{m}^2]$	$Q_{\text{heaters}}[\text{W}]$
<b>Upper limit</b>	310	20	225	$< A_{\text{tot}}$	$< P_{\text{input}}$
<b>Hot case</b>	305	15	210	5.5	0
<b>Lower limit</b>	-200	-10	-145	$< A_{\text{tot}}$	$< P_{\text{input}}$
<b>Cold case</b>	-170	-10	40	5.5	69

**Table 34:** Results for both the hot and cold cases.

Temperature limits are respected in both cases with feasible radiators area and heaters power. Radiators area is less than half area of the S/C and heaters power falls within the power input of 490 W from solar arrays when summed up with the current power budget of 247.8 W requested by components [42]. In hot case, sunshade and MLI contribute both in reducing the heat flux by optical properties, with sunshade additionally reducing the input towards the S/C by resistance across its thickness. Four radiators with  $\varepsilon = 0.88$ , corresponding to Silver Teflon coating, are used to radiate in deep space internal dissipation and the residual external heat penetrating across the MLI. Because of the steady state behavior, in hot case it was necessary that all radiators point deep space: ADCS thermal constraints allowed radiators to point deep space during Orbital phase always but when near Mercury periapsis, when directly facing the planet. Temperatures of solar arrays resulted acceptable for offset angle of  $70^\circ$ , which corresponds to the one adopted during the highest thermal input. Radiators were located in the  $-Z$  and  $\pm X$  directions, as the  $+Y$  and  $+Z$  directions were not desirable locations for radiators because of higher incident IR fluxes. Cold case simulates outer cruise phase at 1 AU, during which S/C sunshade was in anti-sunward direction. The only possibility to maintain suitable temperatures in cold case according to the model is by exposing a radiator to the Sun: because of the diode heat pipe, no heat would enter the S/C through the radiator and it is sufficient that it is not pointed towards deep space. This cannot be accomplished with anti-sunward sunshade. Furthermore, the attitude analyzed would cause the impossibility of pointing solar arrays at the Sun with no power production. Therefore, the model must be reconsidered including local behavior of components with the strictest temperature ranges, employing local heaters for coldest scenarios and located near radiators for hottest cases [34].

## 6 EPS Subsystem

### 6.1 Introduction

The goal of MESSENGER EPS S/S was to generate, control, regulate, distribute and store power on-board for the S/C's various purposes and functionalities in a wide range of situations and substantial solar distance variations. EPS strongly interfaced both with TCS, given the huge solar fluxes, and AOCS for solar panels orientation. EPS was also critical for all other S/S for the power request from the many components that comprised the S/C power budget.

### 6.2 EPS Architecture

The power system was designed to support around 390 W of load power near Earth and 640 W during Mercury orbit [7]. The large solar distance variations imposed severe requirements on EPS architecture and design. PPT topology with a strong heritage to TIMED mission EPS was chosen. EPS was made up of two solar array panels as the primary source, a battery as a secondary source for power during eclipses, a PSE, a PDU, a Solar Array Junction Box, and a Solar Array Drive Assembly. EPS main components are shown in Figure 19 and they are discussed here, along with the rationale for the chosen design.

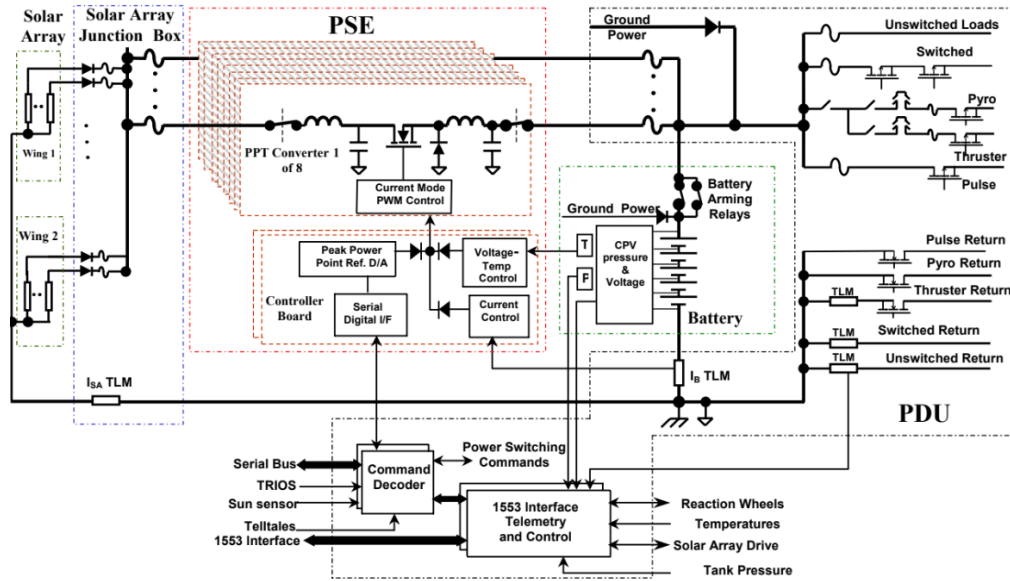


Figure 19: EPS architecture block diagram [3].

**Solar arrays:** consisted of two deployed single-panel wings. Each panel was 1.54 m wide and 1.75 m long. The panel substrates were 18-mm thick aluminum honeycomb with RS-3/K13C2U composite face sheets. The face-sheets were 0.6-mm thick with local 0.5-mm doublers to increment mechanical strength [48]. The panels were articulated using a single-axis solar array drive actuator to limit their temperature and at the same time provide the required power. Rotation was commanded either by ground or by the IEM on-board processor. The large solar distance variations imposed severe requirements on the design. The operating maximum-power-point voltage was projected to range between 45 and 100 V, not incorporating transient voltages expected on the solar array during eclipse departure or abnormalities in orbital phase that were characterized during testing. The solar cells were 0.14-mm thick, 3 cm by 4 cm triple junction cells with a minimum efficiency of 28%. The cells used a standard one-Sun cell top metallization grid design. The cover glass on each cell was 0.15-mm-thick cerium-doped microsheet, CMG type, with magnesium fluoride anti-reflective coating. The cover glass was bonded to the cells with standard DC93-500 transparent adhesive. The solar cell strings were placed between OSR with a ratio of 1:2 to reduce absorbance. The array strings were isolated with de-coupling diodes to protect them from the expected high temperatures. Each string had 36 cells. The strings run parallel to the +X axis with one string per row. To minimize the magnetic field induced by the currents in the strings, adjacent strings were placed with alternating current polarity, and the strings were back wired such that each string return ran under its cells. Cells were tested to high UV at high temperatures showing resistance to degradation. Radiation damage on the solar cells was caused predominantly by solar flare protons. The estimated total dosage was  $4 \times 10^{14}$  equivalent 1 MeV/cm<sup>2</sup> electrons. Aluminized Kapton was used to lower the absorbance of the backside of the solar panel to a level comparable to the solar cell-OSR side to ensure panel survival solar illumination with normal incidence to either side at the closest approach to the Sun. High-temperature wires were used and routed along the titanium boom to connectors at the SADAs, wrapped with MLI. The mass of the solar array panels was 34.12 kg [49].

**Battery:** consisted of Nickel-Hydrogen CPV cells, capable of supporting the required 8-year mission life. The battery chassis was electrically insulated from the S/C structure and connected to the ground through two parallel  $20\text{ k}\Omega$  resistors. The battery cells were designed to minimize the induced magnetic fields. Approximately 300 eclipses were expected during the one-year Mercury orbit phase, with 60 minutes maximum duration. During eclipses, power was managed to ensure that there was enough reserve battery energy to recover from any attitude aberration. The maximum DOD expected during Mercury orbital operations was approximately 55%. The DOD from launch to Sun acquisition was 18%. To minimize overall S/C weight, the battery did not support the full S/C load during predicted eclipses, and therefore load management was planned. Primary battery charge (C) control was ampere-hour integration Charge-to-Discharge (C/D) ratio control performed by flight software within the IEM. The battery was charged at a high rate with available solar array power until battery SoC reached 90%. Commands from the IEM then lowered battery charge current to C/10. When the selected C/D ratio was reached, the IEM commanded the charge current to a ground selectable C/100 or C/150 trickle charge rate. Battery voltage was controlled to preset safe levels with temperature-compensated voltage (V/T) limits that were implemented in the hardware. Whenever the battery voltage reached the V/T limit, battery charge current would taper. This battery charge control technique reduced battery overcharge and associated heat dissipation and extended battery life. The battery package included vessels with calibrated strain gauge pressure transducers. The voltage of each CPV was monitored. Bypass switches were placed across each CPV to eliminate the potential of a single-point failure caused by an open circuit of a pressure vessel. In the event of a cell open-circuit failure, small diodes provided a current path to blow a fusing element in the activating coil of the bypass switch providing protection against an open-cell fault for both charge and discharge operation. Its weight was 24.5 kg, and its size was 36.6 cm x 22.83 cm x 49.17 cm.

**PSE:** contained eight buck-type PPT converter modules, each designed to process around 130 W up to a maximum of 800 W of output power. Four analog control loops for PPT, battery V/T limit, battery current limit, and maximum battery voltage ran simultaneously. The dominant signal drove the PPT converters. When the load and battery recharge power demand exceeded solar array power capabilities, the IEM recursively selected the solar array operating voltage that would generate maximum power. The tracking was performed by adjusting the solar array reference voltage to the buck converters. The output of the buck converters was clamped to the battery voltage. The control loop of the buck converters varied the duty cycle to maintain the input voltage from the solar array wings to the reference value set by the IEM MP. The PSE size was 29. cm x 20. cm x 17.2 cm including thermal vias, and weighted 8.55 kg.

**SAJB:** contained the isolation diodes in series with each string of the two solar array panels, the current shunt resistor of each wing, the PPT module solar array side fuses, and solar array voltage telemetry buffer resistors. The fuses placed in series with each string inside the SAJB protected the PPT modules' input and output fuses in case of a short-circuit in one of the string isolation diodes during the fault condition when the battery voltage was higher than the solar array voltage. This condition could occur during a S/C attitude anomaly when the S/C was closest to the Sun and the solar panels were pointed normally to the Sun. The box dimensions were 16.9 cm x 25.1 cm x 6.38 cm (with the thermal vias), and the weight was 1.48 kg.

**PDU:** contained the circuitry for the S/C pyrotechnic firing control, power distribution switching, load current and voltage monitoring, fuses, external relay switching, reaction wheel relay selects, power system relays, IMU reconfiguration relays, IEM select relays, solar array drives, propulsion thruster firing control, and propulsion latch valve control. There were two sides of the PDU (A and B), and each side of the PDU could command all circuitry. The commands to control the PDU under normal circumstances were uplinked through a IEM MP. In the case of a fault on an MP, an asynchronous serial bus could reconfigure the MP and the PDUs. Solid-state, radiation-hardened, power Metal Oxide Semiconductor Field Effect Transistors (MOSFETs) have been selected for power switching distribution. The load switches consisted of two P-channel MOSFETs in series to allow for high-side switching and to ensure the capability to turn off a load even with a failure in one of its MOSFETs [50]. Each of the 58 loads had independent A-and B-side current and voltage monitoring, and the S/C main power bus was protected from load faults by redundant FM-12 type solid-body fuses. Telemetry that was collected by the PDU consisted of external relay statuses, load currents, load voltages, battery and solar array currents, solar array and battery temperatures, solar array voltages, reaction wheel speeds, propulsion tank and battery pressures, solar array position, S/C temperature, S/C load current, and DSS information. All telemetry interfaced with A and B sides of the PDU. The PDU dimensions were 23.4 cm x 22.6 cm x 35.2 cm (with the thermal vias), and the weight was 12.81 kg.

Solar cells were chosen for their efficiency and resistance to degradation. Nominal bus voltage was 28 V and could vary between 20 and 35 V depending on battery state, which are standardized values for power demand under 2 kW. The bus was fully regulated to isolate the battery from the variations of the solar array voltage and current characteristics and also to maximize the solar array power output over the highly varying operating conditions of the mission. PPT was used for power regulation, suitable for a high number of cycles and with high flexibility to address very diverse operating conditions, thus not causing oscillation on the bus and eliminating lock-up risk. PPT was disabled in case of a "last ditch" state, involving particular conditions in battery operations, which are fully explained in subsection 6.4. Regarding the choice of the battery,

load management was preferred to a battery with higher capacity to reduce mass on board. Resistance to single failures, radiations, thermal fluxes experienced in the vicinity of the Sun, and induced magnetic fields during the whole lifetime were common important features of the design of each single component.

### 6.3 Power Budget

In order to justify the selected EPS architecture and to perform a reverse preliminary sizing, the power budget is presented in [Table 35](#). The power requirement per S/S is compared to the power generated by solar arrays during sunlight or the battery DOD during eclipse. Outer cruise power budget corresponds to Sun distance of 1.0765 AU. The power input from solar arrays in orbital phase was limited by EPS electronics output capability of 800 W.

S/S	Outer cruise	Inner cruise	Orbit phase	Eclipse >35 min	Eclipse <35 min
P/Ls	13.2	15.4	95.1	42.6	58.9
IEM	32.7	34.2	33.5	30.2	30.2
EPS	25.6	25.6	105.6	20.9	20.9
TTMTC	65.5	65.5	110.5	22.8	25.4
GNC	70.3	70.3	119.7	119.7	119.7
TCS	10.2	62.2	58.4	10	23.8
PS	21.9	95.6	74.6	34	47.8
Harness	3.7	7.6	12	4.4	5.5
<b>Total</b>	<b>247.8</b>	<b>382.7</b>	<b>597.4</b>	<b>284.6</b>	<b>332.2</b>
<b>S/A power input</b>	<b>490</b>	<b>528.2</b>	<b>720</b>	-	-
<b>Max DOD</b>	-	-	-	<b>55%</b>	<b>36%</b>
<b>Power margin</b>	<b>49%</b>	<b>28%</b>	<b>17%</b>	-	-

**Table 35:** Power budget per phase in Watt [7].

The highest power requested was reached in orbital phase for all S/S, especially for P/Ls due to the beginning of scientific phase, and TTMTC due to higher downlink data volume. The outer cruise required the least power because of the reverse-sunshade orientation, which lowered heaters usage, and the telemetry-only low data volume to downlink. Power availability was significantly reduced during eclipses due to the limited DOD provided by the batteries and the use of the load management approach for all S/S, except Guidance and Control, which needed to be fully operational to perform maneuvers and maintain the thermally critical attitude constraint. As expected, DOD was greater for longer eclipses despite the lower power requested because of the longer time without power input from the solar arrays, which increased dramatically in phases closer to the Sun, despite the panel being tilted to lessen heat loads.

### 6.4 Operational profiles and available sources

It is now possible to characterize the operational behavior of the primary and secondary on-board sources. Solar cells characteristic power-voltage curve is shown in [Figure 20](#), obtained through on-ground and in-flight testing and normalized at 28°C. The large Sun distances covered by the S/C exposed the solar cells to a wide thermal range: generally, for the higher temperatures envisaged during the mission, it is conceivable to detect notably lower open-circuit voltage and a little higher short-circuit current, resulting in a steeper initial quasi-linear increase in power and a lower maximum power at lower voltage. The evolution of the battery SoC while discharging and recharging respectively during and after eclipse is presented in [Figure 21](#). It is possible to detect a decrease in charge rate once the battery has reached 90%, as conducted by IEM to safeguard the battery, and eventually a trickle charge rate during the full charge phase. The shown maximum DOD respected the limitation imposed during eclipses longer than 35 minutes.

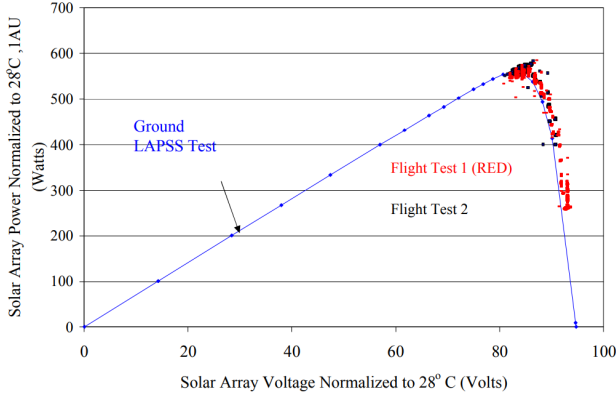


**Figure 20:** Solar panel power over voltage characteristic curve normalized at 28°C [3].

The maximum DOD for a battery is heavily influenced by the number of cycles. The allowed number of cycles for  $NiH_2$  with a DOD of 55% (for long eclipses) is in the order of  $10^4$ . The number of cycles would be slightly higher with a maximum DOD of 36% (for short eclipses), which might have been deemed an acceptable choice considering that around 300 eclipses were expected in the orbital phase. Additionally, the characteristic power-voltage curve of the solar cells strongly varied with illumination. The offset angle caused the incident solar flux to decrease approximately according to a cosine law, reducing both power production and thermal radiation input. Without changing the Sun offset angle, for higher solar flux experienced at lower Sun distances, an increase in short-circuit current and a decrease in open-circuit voltage could be observed. When decreasing the distance from the Sun, the light variation effect on the curve is summed up with an increase in temperature and a change in the Sun offset angle according to thermal and power requirement conditions. This high variability of the power curve made it necessary to employ PPT to locate the maximum power point and maximize power production in highly varying conditions, which was a mission driver for MESSENGER. The solar array Sun-offset angles were adjusted about 15 times a year as MESSENGER's solar distance changed. An example of the sun-offset limits and planned solar array position updates for solar distance for the first six months of 2009 (before 3rd Mercury fly-by) are shown in Figure 22. It can be noticed that because of the higher incidence power at low offset angles, the variations in Sun offset angle were limited by the temperature limits of the solar arrays. Due to the considerably larger distances to the Sun reached during the S/C's heliocentric orbit prior to the third Mercury fly-by, the thermal limit of the offset angle was driven to zero. Because the normal S/C power consumption was much lower than 800 W, the maximum output limit of PSE, the priority in selecting the position was to keep closer to the upper power boundary to maximize power availability while obeying the temperature limitations with a larger margin. The nominal Sun offset angle operational zone, which varies with Sun distance, is displayed Figure 23. It is restricted between the maximum array temperature at low angles and the minimum power production to fulfill loads. The high increase in thermal limit was caused by higher solar fluxes reducing Sun distance, whereas the relaxation of the limit power generation can be attributed to a reduction in heaters power, which was required in the early inner cruise, due to the start of validity of the SKI sunshade-pointing constraint for ADCS S/S.

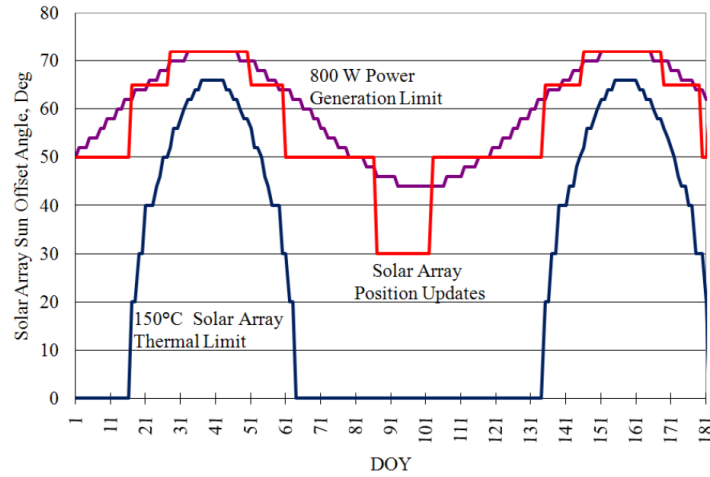


**Figure 22:** Available and requested power during the mission [4].

A crucial element of the design was the preference for a load management method over a heavier, higher capacity battery, as explained in subsection 6.2. The operational constraints on battery management included keeping the discharge current below 14.5 A and the battery SoC above 40%. Since the normal operating level during high-activity events with all of the

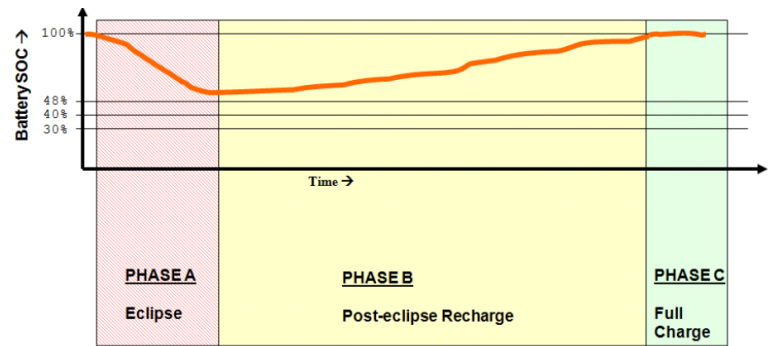


**Figure 21:** Battery SoC evolution during and after eclipse [4].

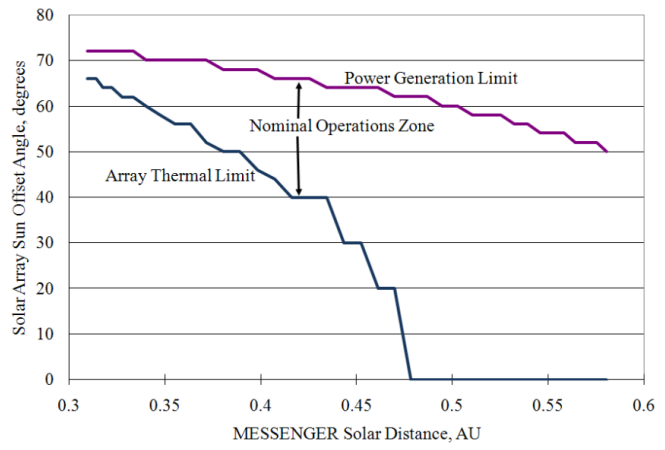


**Figure 23:** Limitations and operational zone of Sun offset angle with mission timeline [4].

instruments active was between 15 A and 16 A, the 14.5 A requirement meant the battery could not carry the entire S/C load, so power-downs were required. The 40% state-of-charge limit provided a 10% margin over a 30% state-of-charge limit where the system would have entered a "last ditch" state, based on the assumption that the S/C had lost knowledge of its position and had gotten off-pointed. It set the operating voltage of the system at a predefined level instead of allowing PPT. Then it powered down heaters, commanded the G&C system to no longer use the ephemeris files, reset the MP, switched the remote terminal for the PDU and PSE, and placed the S/C into Earth-acquisition mode. During events when the solar arrays could provide power for long amounts of time, such as 60 minutes eclipses, the SoC limit became an issue and power-downs were required to not trigger the "last ditch" state. Initially, the S/C load was managed by turning off or changing set points for heaters. The power-down was substantially larger for longer activities, where the battery SoC rule became a worry, involving instruments and communication devices as well.

## 6.5 Preliminary sizing

Below, preliminary reverse sizing is performed to justify the chosen architecture and design strategies. They are then compared with the actual parameters from mission literature. As outlined in [subsection 6.3](#), the maximum power requested during daylight and the longest eclipse in orbital phase are considered to size the battery and the solar arrays. Orbital period is 12 hours, of which maximum 60 minutes are spent in eclipse. The mean Sun irradiance along Mercury's orbit is considered for reverse sizing, with a value of  $I_0 = 9116.4 \text{ W/m}^2$

### 6.5.1 Solar array sizing

The power requested from solar arrays was calculated using maximum power demand both in sunlight and eclipse. As previously explained in [subsection 6.2](#), PPT was used for power control because of the high variability of illumination and thermal conditions, despite its lower efficiency, which was set according to literature at  $X_d = 0.80$  and  $X_e = 0.60$  in sunlight and eclipse respectively. The efficiency at the BOL was set to the minimum value of  $\epsilon_{BOL} = 28\%$  to provide a worst case scenario in power production, which was additionally worsen by sizing in EOL conditions. In fact, degradation of the cells considering the mission lifetime of 8 years has been accounted. In particular, for *GaAs* solar cells employed in the mission [51], the *dpy* factor was set to 0.0375 /year, while the inherent degradation, commonly ranging between 0.49 and 0.88 according to literature, was considered as the worst case ( $I_D = 0.49$ ) due to the hazardous radiation fields experienced in the interplanetary environment and at low distances from the Sun. The power was also limited by solar panels tilting to reduce temperatures in the harsh thermal environment, with a maximum offset angle corresponding to power production worst case of  $\theta = 70^\circ$ . The required area of the cells to obtain the needed power as a function of the  $\theta$  angle can be seen in [Figure 24](#).

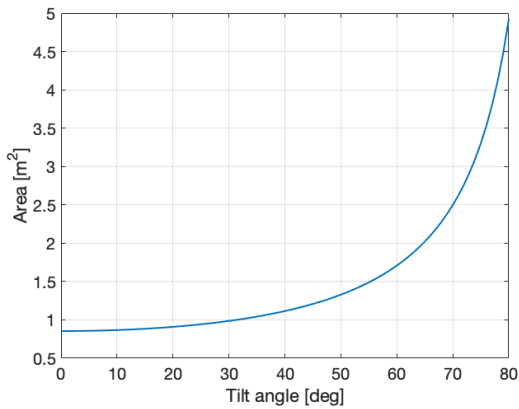


**Figure 24:** Required area as a function of  $\theta$ .

Moreover, the surface of the arrays was covered by OSR to reduce absorptivity, in ratio of 2:1 with the cells, which has been taken into consideration when calculating the total area and mass of the solar arrays. By looking at [Figure 24](#), which considers only the cell's area, just  $2.50 \text{ m}^2$  were needed when considering an offset angle of  $70^\circ$ . In [Table 36](#), results of sizing are shown and compared to actual mission values. Due to the adoption of worst-case conditions in sizing, the area of the solar arrays is slightly larger than the real value, as expected. Since solar arrays were made of multiple materials for cell functioning, structural integrity and thermal protection, a mean density was estimated in the perspective of reverse engineering and used to compute the sizing mass.

P <sub>req</sub> [W]	A <sub>SA</sub> [m <sup>2</sup> ]	A <sub>SA_real</sub> [m <sup>2</sup> ]	m <sub>SA</sub> [kg]	m <sub>SA_real</sub> [kg]
786.87	7.49	5.39	47.43	34.12

**Table 36:** Results of preliminary solar array sizing.

Sizing is additionally refined by calculating the number of solar cells to form the active power production area, which was 1/3 of the total array area. As a matter of fact, the rest was occupied by OSR. Considering the cells surface equal to the literature value of  $3 \text{ cm} \times 4 \text{ cm}$ , 2082 cells are calculated to be required. A common value for the voltage of the single cell was considered and set equal to 2.5 V. The bus voltage of  $28 \text{ V} \pm 6 \text{ V}$  is a standard value for power load less than 2 kW, which was the case of MESSENGER mission. To obtain such a voltage, cells need to be put in series to sum up the single cell voltage of 2.5 V: solar cells shall be organized in series of 12 producing an actual system voltage of 30 V. This configuration leads to adjustment of the total number of cells to 2088, and of the total solar array area to  $7.5 \text{ m}^2$ . The latter is divided between the two panels. Sizing calculations are fully compatible with the justification for the adopted design, regulation and control strategy provided in subsection 6.2.

### 6.5.2 Battery sizing

The battery sizing will produce as output the capacity, mass and volume of the battery. This necessitates understanding of the properties of the battery cell. In the MESSENGER mission, only one 23 Ah  $\text{Ni} - \text{H}_2$  battery was present [45]. This kind of battery has been preferred due to its higher specific energy and longer life [52]. In fact, the DOD had a value of 55%, typical for long mission duration [3]. To calculate the capacity required by the batteries a couple of parameters must be defined. The eclipse time was set at 60 minutes since it represented a worst case scenario, as stated in subsection 6.2. The power needed in eclipse was 284.6 W, as mentioned in Table 35. The efficiency of the battery has been taken as 85%, which is a common value for  $\text{Ni} - \text{H}_2$ . The results of the sizing can be appreciated in Table 37, along with the real one for comparison.

$C_{\text{batt}} [\text{Ah}]$	$C_{\text{batt,real}} [\text{Ah}]$	$m_{\text{batt}} [\text{Kg}]$	$m_{\text{batt,real}} [\text{Kg}]$	$V_{\text{batt}} [\text{dm}^3]$
21.74	23	10.15	24.5	12.18

Table 37: Battery sizing results.

Regarding the capacity, the computed value is highly satisfying compared to the real one. In fact, the battery was dimensioned with a lower capacity than needed to save mass, as already outlined in subsection 6.2. Instead, there is a considerable difference in the mass. This could be caused by the fact that the sizing accounts only for the mass of the part of the battery that accumulates energy, neglecting various cables or containers, that in the case of MESSENGER were used. The sizing can be refined, taking into account the voltages of the single cells used and computing the cells needed in series to achieve the desired system voltage. Subsequently, the number of strings needed to have the desired capacity is computed. For the single cell voltage, a value of 2.50 V has been chosen. This value is slightly greater than is typical for these types of cells, but it is justified by the specific configuration used in the MESSENGER mission. The cells were arranged following a CPV configuration that allows this particular  $V_{cell}$  value [47]. The packing factor chosen was 0.90 because it's a typical value [47], while the capacity of the cell is a "degree of freedom" of the problem. Results are presented in Table 37, showing higher similarity to the real mission value in terms of capacity.

$C_{\text{batt,refined}} [\text{Ah}]$	$C_{\text{batt,real}} [\text{Ah}]$	$N_{\text{series}} [-]$	$N_{\text{parallel}} [-]$
22.18	23	12	23

Table 38: Refined battery sizing results.

The results are obtained setting 1 Ah as single cell voltage as design degree of freedom, obtaining satisfying results with respect to available mission literature values.

### 6.5.3 EPS mass, power and data budgets

The real total mass of the EPS S/S is 93.9 kg, including all components described in subsection 6.2. Considering the calculated masses by preliminary sizing, including the 20% system margin, 111.4 kg must have been initially allocated for EPS S/S. The mass of the cables is equal to 27.85 kg, which is 25% of the total calculated EPS mass. Total EPS power request ranged from a 25.6 W in cruise to a maximum of 105.6 W in orbital phase due to the higher power input to be regulated, controlled and distributed, with a consumption of 20.9 W in eclipse. Data budget included measurement of voltages, current, SoC, charge/discharge rate and temperatures through suitable sensors, as well as the data from PPT modules, switches, monitoring, relays, electrical interfaces, and commands both from ground and from IEMs.

### 6.5.4 Positioning of components and pointing requirements

Solar arrays consisted of two deployed single-panel wings connected to the  $\pm X$  sides of the S/C bus via structural support, and they could be rotated around the same axis through electrical motors to point the Sun with different offset angles. It allowed temperature and power regulation of the arrays in different Sun distances and conditions. Regarding the battery, it

was originally packaged on the top deck and farthest from the sunshade, which was the final location of the helium tank. Thermal simulation of orbit phase operation showed that the battery transient temperature excursion during sub-solar and near sub-solar orbits would have exceeded the battery's maximum allowable temperature limit. As a direct result of this thermal analysis, the battery and helium tank were switched, and the battery was packaged directly behind the sunshade and above main fuel tank. The battery imposed to the AOCS S/S the HPKO pointing constraint, according to which the top deck (-Z axis) had to point away from the surface of Mercury to protect the battery and other components from albedo heat flux.

## 7 Configuration

### 7.1 Introduction

MESSENGER's configuration included the design of internal and external components distribution, vehicle structure, shape and appendages. It had a close working relationship with structure design due to the necessity to assure loads and mechanical characteristics, all S/S thermal, FOV and pointing needs, as well as launcher adapter design and fairing constraints.

### 7.2 Vehicle shape and appendages distribution

Vehicle shape design was correlated to the structural characteristic of the S/C. The integrated structure, visible in [Figure 25](#), implemented four large vertical panels to support the two fuel tanks, the oxidizer tank, and the plumbing panel. Being equal in volume, the three tanks were implemented in two double H compartments. The composite panels thickness was reduced by transferring tank support loads to the corner of the structure. A thin, copper conductive ground plane was placed over the composite panels to improve conductivity for grounding. A rigid center column was implemented to transfer loads into the aluminum adapter, compatible with the Delta II interface. The adapter was bolted to the aft ends of the four vertical panels making up the center column [\[7\]](#). Three composite panels covered the top of each fuel tank and were used as mounting areas for S/C electronics. A three-piece composite-sandwich bottom-deck panel added stiffness and packaging area for the P/Ls. A single top-deck panel, also acting as a radiator, mounted the LVA thruster, small thrusters, helium and auxiliary fuel tanks, star trackers, and battery. Two side radiator panels completed the box structure and added shear stiffness. The very short, direct load paths in this stiff-box arrangement resulted in a compact low-mass primary structure ( $1.27\text{ m} \times 0.71\text{ m} \times 1.05\text{ m}$ ), providing sufficient panel and deck area for all components [\[53\]](#). The S/C appendages included sunshade, MAG and solar arrays. The sunshade protected the S/C from the huge solar fluxes at Mercury, and it was supported by a welded 3Al-2.5V titanium-tube assembly to be thermally isolated from the S/C. Because of power requests and S/C bus shadowing by sunshade, solar arrays were mounted on deployable surfaces and were thermally isolated from the S/C body by arms of titanium tubing as well to limitate thermal fluxes. The MAG needed deployment to avoid disturbance by the S/C residual magnetic dipole [\[54\]](#).

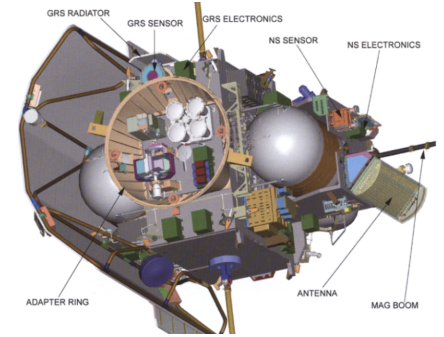


**Figure 25:** View of the S/C bottom deck, including the launch adapter ring.

panels completed the box structure and added shear stiffness. The very short, direct load paths in this stiff-box arrangement resulted in a compact low-mass primary structure ( $1.27\text{ m} \times 0.71\text{ m} \times 1.05\text{ m}$ ), providing sufficient panel and deck area for all components [\[53\]](#). The S/C appendages included sunshade, MAG and solar arrays. The sunshade protected the S/C from the huge solar fluxes at Mercury, and it was supported by a welded 3Al-2.5V titanium-tube assembly to be thermally isolated from the S/C. Because of power requests and S/C bus shadowing by sunshade, solar arrays were mounted on deployable surfaces and were thermally isolated from the S/C body by arms of titanium tubing as well to limitate thermal fluxes. The MAG needed deployment to avoid disturbance by the S/C residual magnetic dipole [\[54\]](#).

### 7.3 Configuration inside the fairing and launcher interface

The S/C "packed" configuration was designed considering the launcher available dynamic envelope as well as the mission requirements. With the composite structure designed to channel all loads into the center column, a square-to-round adapter was necessary to match up with the launch vehicle's separation clamp band interface. The adapter was a 6061-T651 aluminum flange, bolted to the aft ends of the four vertical panels, making up the center column. During launch, tank loads and deck loads were carried directly into the adapter from the vertical panels. The adapter was designed to distribute the loads evenly from the corners of the center column to the round interface. The forward adapter flange was slotted between each bolt to accommodate the thermal expansion mismatch between the adapter and the S/C structure. Locating the LVA thruster on the S/C top deck resulted in a short, mass-efficient adapter. The free space inside the adapter provided a convenient mounting deck for the majority of the P/Ls: MDIS, MLA, MASCS and XRS were mounted inside the adapter ring, including the pivoted platform. The other P/Ls were mounted outside the ring on the same deck. A consequence of this configuration was that the S/C propulsion system had to be launched upside down, requiring the propellant tank outlets to be located in the upward direction during launch, meaning that the pressurization gas would be adjacent to the tank outlet. This in turn prevented the use of screen-type propellant management devices in the main tanks [\[7\]](#). Deployment mechanisms were implemented for the solar arrays and the magnetometer to match the limited available space in the fairing. During the launch, the solar arrays were supported using a ball-and-socket center hold down and four 'V'-flexure joints per wing. A pyrotechnic-release mechanism preloaded each panel against the fittings. The solar array hinges were located at each end of the arms connecting the panels to the core structure. The panels were released first and allowed to over-travel and settle. The 3.6 m MAG boom was separated into two segments with one hinge between the S/C structure and the first segment and the other between the two segments. The pyrotechnic, cable-cutter-release mechanism preloaded the boom against the S/C prior to deployment, which took place similarly to the panels. After deployment, all six hinge lines were pinned in place to prevent hinge rotation during maneuvers using the LVA [\[54\]](#).

### 7.4 External configuration

Some critical pieces of the various S/S, including the thrusters and reaction wheels, as well as some components of EPS and TCS, were located outside the S/C. This section will explain the rationale for the placement of all elements.

#### 7.4.1 Propulsion Subsystem

**Thrusters:** the S/C was equipped with 16 thrusters organized into 5 modules (A, B, C, P, S). The primary maneuvers were carried out by the main bipropellant engine (LVA), which was positioned along the  $-Z$  axis. Eight 4.4-N thrusters (named A and B) were stacked in double-canted groups of four, with each thruster tilted at  $45^\circ$ , to achieve redundant three-axis attitude control. The type A and B thrusters were deliberately placed to deliver force along all axes. Because of this layout, the S/C could be controlled without the usage of a set of 12 thrusters. The C thrusters were four 22-N monopropellant LVA-thrust vector control (TVC) thrusters that were utilized for main thrust burns and lesser velocity adjustments. They produce forces in the  $+Z$  direction. The S thrusters were employed to change the velocity in the sunward direction, while the P thrusters did the opposite. The latter protruded from the sunshade [7].

#### 7.4.2 Tracking Telemetry & Telecommand Subsystem

**Antennas:** the MESSENGER mission necessitated a high-gain link with Earth in all directions around the S/C, which was achieved with electronically steerable PAAs. Boresights were located in the  $+X$ ,  $+Y$  and  $-X$ ,  $-Y$  quadrants for the antennas. Medium-gain and low-gain antennas were employed for uplink and low-gain downlink communications during the cruise phase and in emergencies. Complete coverage in all directions was secured by strategically putting all antennas in the front and back of the S/C and leveraging their beamwidth and ability to steer. This design made uplink and downlink communications available in both normal and emergency conditions [7].

#### 7.4.3 Electric Power Subsystem

**Solar Panels:** the solar arrays were made up of two independent panel wings that were deployed and structurally linked to the  $\pm X$  sides of the S/C bus. These arrays used electric motors to spin around a common axis, allowing them to be oriented at varied offset angles toward the Sun. This feature aided array temperature and power regulation in a variety of solar distances and situations [7].

**Battery:** The battery was originally packaged on the top deck, farthest from the sunshade, where the helium tank was eventually installed. The battery's transient temperature excursion during sub-solar and near-sub-solar orbits would have surpassed the battery's maximum permissible temperature limit, according to thermal simulations of orbit phase operation. Therefore, the batteries and helium tank were switched, and the battery was housed just below the sunshade and above the primary fuel tank. The battery imposed the HPKO pointing restriction on the AOCS S/S.

#### 7.4.4 Thermal Control Subsystem

**Sunshade:** MESSENGER relied on a ceramic-cloth sunshade as part of its thermal design during the inner cruise and orbital stages. When directed towards the Sun, the sunshade is positioned in the  $-Y$  direction and gives complete coverage to the S/C. Its principal function was to control temperature levels within operational limits. Furthermore, the sunshade's design included a support assembly for the high-temperature MLI blanket as well as four DSS, one PAA, three LGA assemblies, and two thrusters [53].

**MLI and Radiators:** the S/C electronics were totally encased in MLI, with the exception of radiators and apertures. This MLI was designed to protect and insulate the S/C's critical components from direct solar radiation within 0.95 AU. The S/C featured four radiator panels, one on each side, positioned perpendicular to the Sun's direction. These radiator panels were critical in keeping the electronic boxes attached to them at ideal temperatures. The radiators, together with the regulated heat leaks from the MLI, contributed to the overall thermal management of the S/C, ensuring that the remaining S/C components remained within safe temperature limits [7].

#### 7.4.5 Attitude Determination & Control Subsystem

**Reaction wheels:** four RWs were used as primary actuators to regulate the S/C's attitude. They were in a pyramid configuration, with the tip on the  $Z$  axis. RWs were located symmetrically with respect to the  $Z$  axis so that their weight was balanced. These RWs were mounted on the S/C deck beneath the sunshade and were equally spaced so that torque would not be concentrated in a critical point [7].

**Star Trackers & Sun Sensors:** two co-boresighted star trackers pointing out along the  $-Z$  axis on the upper deck, as depicted in Figure 26, supplied highly fine inertial attitude reference. Given that the S/C's  $-Y$  axis was continually oriented towards the Sun and the top deck stayed oriented away from Mercury during the functioning of the P/L instruments, it may be assumed that the  $-Z$  axis was primarily aligned with the stars for the majority of the mission [7]. Since the sunshade always faced the Sun, four Sun sensor heads were placed on its opposing corners, and two more were placed on the back of the S/C to account for potential Sun pointing losses in case that the inertial reference system was lost. To avoid FOV problems and to be able to scan the entire sky, they were not placed close to one another.

**Magnetometer:** a three-axis, ring-core, fluxgate magnetometer was used. To minimize interference with the onboard electronics, the MAG sensor head was mounted on a lightweight, 3.6 m carbon-fiber boom that extended in the anti-sunward direction. Because the sensor may protrude from the shadow of the S/C when the pointing was close to the permissible off-Sun limits, it had its own sunshade [7].

## 7.5 Internal configuration

Some important elements are placed inside the lightweight composite structure of the S/C, such as the fuel and oxygen main tanks, along with some components of the EPS and OBDH systems. This section will give an insight into the placement and engineering strategies of these elements.

**Tanks:** the S/C had a configuration with three tanks positioned along the  $Y$  axis referred to the body reference frame, visible in Figure 26. In particular, the two fuel tanks were located in the  $+Y$  and  $-Y$  direction, while the oxidizer tank was positioned in the reference frame center. The main propellant tanks were symmetrically positioned about the centerline of the S/C in order to keep the CM under control during maneuvers. Four titanium struts were utilized to offer lateral support for the tanks. The pressurizer tank, which was symmetrically positioned relative to the CM, was situated off the centerline of the main tanks to balance the sunshade. The propellant mass fraction of the S/C at launch was 54%, so the propellant location significantly affected the CM. The absence of diaphragms in the main fuel tanks and oxidizer tank permitted unrestricted movement of the propellant within each tank. Consequently, the positioning of the propellant inside the tanks introduced the highest level of uncertainty in the CM determination. To address this uncertainty, the CM was calculated for various worst-case positions and fill levels for each tank, thereby establishing a range for the expected CM location. If the propellant collected at the outlet of the tank while the auxiliary tank was being filled, there was a noticeable shift in  $-Z$  direction. On the other hand, if the propellant in the main fuel/oxidizer tanks moved towards the top end ( $+Z$  direction) while the auxiliary tank was almost empty, it represented the most unfavorable situation for an  $+Z$  CM offset. Likewise, a similar examination can be carried out to identify the most unfavorable CM offsets along the  $X$  and  $Y$  axes. The main cause for a CM displacement during the mission was thruster usage during the DSM and TCM events. Simulations showed that LVA thruster firings longer than 10 seconds moved the propellant masses against the tank outlets, resulting in a negative offset along the  $-Z$  direction. Similar effects were observed for longer C thruster firings and A/B thruster combinations with net  $+Z$  thrust [7].

**IEM:** the IEM served as the central control component for the entire S/C. To ensure reliability, there were two IEM units onboard for redundancy. The IEM included various elements such as a DC-DC power converter board, the SSR, the MP, an interface board, and the FPP. Designing the IEM presented numerous challenges due to the S/C's strict mass constraints, harsh thermal conditions, and unique composite construction. To reduce weight and costs, the aluminum chassis of the IEM module was created using a casting process. In fact, the entire module weighs only 5.87 kg. The S/C was made of graphite/cynate ester, a composite material that has a significantly different CTE compared to aluminum. This CTE mismatch could create excessive stresses on the mounting inserts during thermal cycles, potentially leading to structural failure. To solve this problem, slip joints were employed to absorb the CTE mismatch. The front and the back covers of the chassis were made using a magnesium sheet to further reduce weight. However, the S/C deck's lightweight shell material has low thermal conductivity, making it unable to effectively dissipate the heat generated within the IEM. To overcome this challenge, heat pipes were connected from the thermal vias to radiators, which release heat into space. From the structural point of view, care has been taken to tailor the board frequencies to be distinct from the chassis frequencies to avoid resonance [55].

**PDU:** the PDU was responsible for managing the electrical network of the S/C. Also in this case, the weight reduction was a strong driver in the design. This design included the usage of printed circuits and a compact interconnection scheme. The main challenge in achieving weight reduction was maintaining system reliability. The PDU was composed of five boards and the total weight was about 12.5 kg. To ensure both thermal dissipation and structural support, each circuit was bolted to the chassis using a modular design. An epoxy resin has been added to the sides of the board to raise the resonance frequency above 150 Hz. This resin also enhanced the thermal transfer between the circuit and the chassis. The chassis was realized using the magnesium alloy ZK60A-T5. To achieve high density packing, electronic components were mounted on both sides of the boards. The coupling between the PDU and the composite structures had the same issue as described in the IEM. As a result, slip joints were used to remedy this issue. Each electronic module had its own thermal channel to the radiator through diode heat pipes. Special thermal vias were created to direct waste heat away from the electronics and into the heat pipes. The PDU was installed on the  $-X$  face, and its radiators were always oriented orthogonally to the Sun, allowing waste heat to be vented into space. Due to the low electrical conductivity of the S/C, electrical conductive tapes were also utilized for electrical grounding [56].

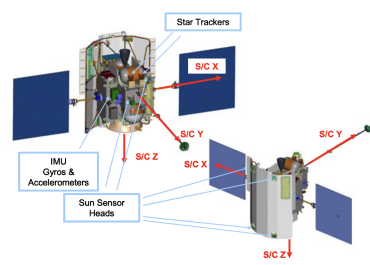


Figure 26: S/C axes and sensors position.

## 8 On-Board Data Handling subsystem

### 8.1 Introduction

The OBDH S/S was designed to carry and store data between the various electronics units as well as the ground segment via the TTMTCS/S. It also interacted heavily with P/Ls for scientific data, G&C flight software, and all S/S supplying data via sensors. The OBC, OBSW, and DH strategy were the focal points of the OBDH S/S.

### 8.2 OBDH Architecture

Some characteristics of the mission became drivers for OBDH architecture and flight software design. Firstly, as a deep space mission, MESSENGER low communication data rates necessitated the use of an SSR capable of storing a vast collection of scientific data, as well as a picture compression approach to conserve SSR space and downlink bandwidth. Secondly, G&C software was influenced by strict pointing constraints, like SKI and HPKO, to avoid S/C loss due to overheating. Finally, solar conjunctions disrupted connection with Earth for extended periods of time, necessitating the inclusion of a rule-based autonomy system capable of monitoring for faults and taking corrective action [7].

#### 8.2.1 On-board computer and OBDH adopted bus

The MESSENGER flight computer consisted of an IEM, implementing command and data handling, guidance and control, and fault protection functions. A second unit was implemented on-board for redundancy, with its MP typically remaining unpowered due to MESSENGER mission power constraints and not serving as a "hot spare". The FPPs in both IEMs were powered continuously. The IEM design was partitioned into five daughter cards, a backplane, and a chassis, as depicted in Figure 27. The OBDH bus adopted was the MIL-STD 1553 serial bus [54], often used on S/C platforms, working on 1 Mbit/s fixed data throughput and Command/Response transaction type. The internal architecture is explained further below [57].

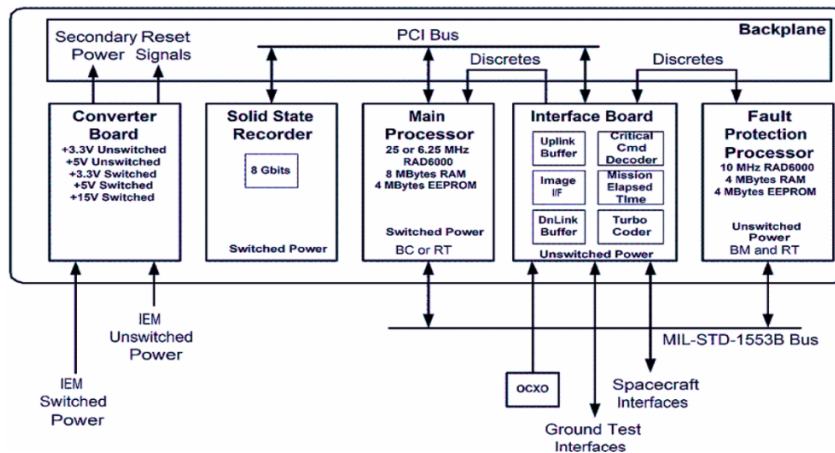


Figure 27: IEM architecture and interfaces [5].

**Main Processor:** it was a RAD6000 processor which ran custom-written C code that performed most of the major functions on the S/C. Each of the two redundant IEM had an MP and the system only allowed one IEM to be both the Bus Controller and the Command and Data Handling unit at the same time. The main processor functionalities were:

- Processing ground commands, both real-time and sequenced, and routing commands to S/S and P/L units;
- Downlink of all telemetry, some generated within the MP and some received from other units via CCSDS protocol;
- Processing of sensor data to determine S/C attitude and processing onboard ephemerides;
- Attitude control and propulsive maneuvers execution through closed-loop control, using accelerometer-based  $\Delta V$  accumulation and gyro-based attitude monitoring;
- Determination of the optimal operating state of solar arrays, monitoring battery SoC and recharge rates;
- MIL-STD 1553 data bus control, running a file system for onboard data storage and managing the SSR, onboard file playback using the CCSDS, and image compression before downlink to Earth;
- Propellant tank temperatures control through closed-loop temperature monitoring and heater commanding.

The MP operated at 25 MHz [57]. The MP was populated with 8 Mbytes of Random Access Memory and 4 Mbytes of Electrically Erasable Programmable Read-Only Memory. The MP in the second redundant IEM was configured to be a Remote Terminal and it was normally left powered off as a cold spare. Typically, it was powered only for periodic updates to non-volatile memory space [57].

**Fault Protection Processor:** the second RAD6000 processor, operating as a MIL-STD 1553 Bus Monitor, performed independent fault detection and protection functions for the S/C. It monitored the MP and most of the other units on the S/C for health and safety. The FPP had the authority to switch to redundant units, including the redundant MP. The FPP software ran a Reverse Polish Notation rule evaluation engine. 270 autonomy rules were evaluated at 1 Hz to determine if a limit had been violated or if a state had changed from healthy to unhealthy. If an error persisted for a pre-programmed duration, the rule would trip and execute a series of relative time commands to address the issue. The rules monitored telemetry from all S/S but took only a handful of different actions. The system was designed to either: switch to a redundant unit, enter one of two demoted modes (Safe-Hold for serious faults or Earth-acquisition mode in case of inertial reference loss), or power down the faulted unit. The FPP board operated at 10 MHz and was populated with 4 Mbytes each of RAM and EEPROM. Single-bit errors in RAM and EEPROM were corrected.

**Solid State Recorder:** it implemented 8 Gbits of memory with upscreened commercial SDRAM. The memory was arranged as 20 nibbles of 80-bit words with 64 bits of user data and 16 bits of error code correction data. Each nibble in error was corrected. Memory contents were kept after an IEM reset but were lost if the IEM switching power was turned off.

**Interface Card:** it performed critical command decoding, the uplink receipt and downlink framing hardware. The SSR and interface card communicated with the MP via an internal Peripheral Component Interconnect bus.

**Converter board:** a secondary power conversion unit was integrated.

**Oven-Controlled Crystal Oscillator:** it was the IEM companion unit, utilized to give precise onboard timing. This unit was not located within the IEM chassis, but rather outside of it.

Three of the five daughter cards (MP, FPP and SRR) communicated over a 32-bit PCI bus operating at 25 MHz. These boards were specified to be as generic as possible, incorporating a few features that would be mission-unique so that their specifications could be generated as early as possible. The VxWorks operating system was selected on the basis of its proven performance in various space missions, including Mars Pathfinder and the Mars Exploration Rovers.

### 8.2.2 Data handling strategy

Data storage was managed using an on-board file system rather than a raw partition technique. It was owing to the system's image management system and its severe downlink restrictions. This necessitated various changes. Flight systems were added to collect data into files and independently pick these files for downlinking. To secure data delivery, CFDP was chosen as an FTP-like protocol for file transfer. To receive the files and post-process the data, software was installed on ground segment[6].

**On-board file system:** to maximize the return of science data and to store and compress images, it was decided to manage the SSR using a file system. This enabled the software to read files containing uncompressed images in SSR, apply a compression algorithm, and store the smaller file back to the SSR until downlink without saturation. The file system allowed multiple usages of the same memory areas for science data, compressed images or S/C HK data.

**CCSDS File Delivery Protocol:** a new standard for the transmission of file data was used, which was essentially a process that transferred a file between S/C and the ground system using a guaranteed data delivery protocol with handshaking between the flight and ground CFDP clients to retransmit pieces of a file lost due to data dropouts, rather than entire images or files, maximizing science data downlink. When the S/C was nominal, CFDP commands could be transmitted to delete the unnecessary contingency files, freeing up valuable SSR space and downlink bandwidth for science data.

**Automated File Playback:** to simplify the management of the flight file system and CFDP, the flight software implemented an automatic SSR playback process. A prioritized directory structure was created for the storage of science and HK files. The playback manager was enabled by command at the start of data transmission and began transmitting the data with the highest priority first. Large volumes of HK data were saved in low-priority directories during long periods of no transmission so that the ground team could then promote those files to a higher priority and downlink them.

**Autonomy:** given the important requirement to maintain a Sun-pointing attitude and the awareness that MESSENGER would be without Earth communication for extended periods of time, a complex autonomous system was built into the flight software. Each second, relevant engineering telemetry data was captured and stored in an onboard data collection buffer. Autonomy rules, expressed in reverse polish notation, were uploaded to the S/C. Each rule had conditional logic in the premise to check data values in the DCB. Every second, a rule evaluation engine in the flight software processed each rule. A stored command sequence was executed for each rule that evaluated "TRUE" to take corrective action. This rule feature enabled the autonomous system to respond to errors by switching to a backup flight processor, switching to a backup star tracker, and cutting off power loads if a low voltage condition occurred.

**Guidance & Control:** The MESSENGER flight software incorporated advanced G&C attitude estimation and control algorithms. The software not only maintained a three-axis stabilized Sun-pointing attitude, but it also offered a variety of pointing options to make sensor operations easier while in orbit around Mercury. It also regulated the propulsion system and fuel flow in tanks to assist thruster maneuvers, rotated the solar panels to optimize power and temperature, a phased array antenna to keep it pointed at Earth, and an optical pivot platform in the MDIS instrument.

### 8.2.3 Data flow architecture

The MESSENGER flight computer collected data from P/Ls, including MDIS, GRNS, MAG, MASCS, EPPS and XRS [53]. With the exception of MDIS, instruments flowed their data in the form of CCSDS data packets through the Data Processing Unit and then across the MIL-STD 1553 bus to the MP. The flight program generated files including both scientific and housekeeping data once it was received by the MP. The files were then automatically picked for downlink using the priority-based algorithm and prepared for transmission using the CFDP, both discussed in section 8.2.2, and then sent to the ground. The ground program used CFDP to recreate the files, then processed them before sending them to the operations data repository and the Science Operations Center. Through interaction with both the flight and ground systems, the MESSENGER S/C operations team controlled the overall processing of these files. Data flow is illustrated in Figure 28.

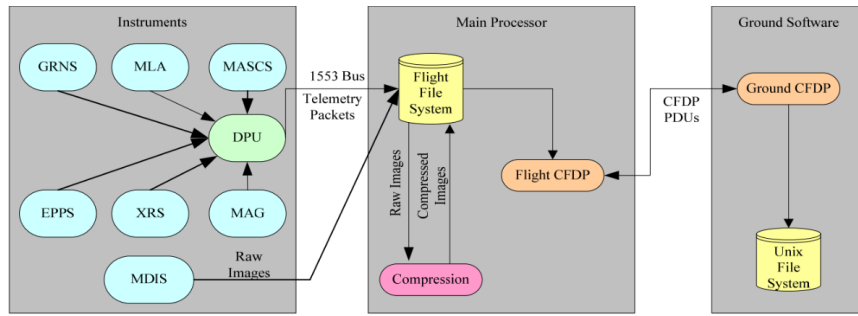


**Figure 28:** MESSENGER instrument data flow with corresponding mirrored CFDP and file storage [6].

The MDIS picture data were sent to the MP in 64-kilobyte blocks over a high-speed interface. When the first block of data was received, a file was opened on the SSR and the data was stored into the file using a Direct Memory Access transfer. The flight program would compress available photos previously saved on the SSR at a point specified by the operations crew. The majority of P/Ls were connected to the MP via a common bus and DPU, but the inclusion of other connections from MDIS and HK data to the MP allegedly led to the adopted bus being a hybrid centralized-federated bus [5].

## 8.3 OBDH reverse sizing

A reverse sizing was performed to justify the selection of the MP and memory, RAM, EEPROM, and SSR dimensions.

### 8.3.1 OBC sizing

The sizing of the On-Board Computer involves determining the number of instructions the processor needed to execute in one second, as well as determining the appropriate sizes of the RAM and ROM memory. The RAM stores both data and code, while the ROM only contains code. Accurate estimation of these values requires a comprehensive understanding of all the S/S of the S/C. It is necessary to estimate the amount of code and data used by each function, along with the instructions per second required to perform the task. A function represents an action performed by a S/S, such as attitude determination or power control. The scientific data generated by the P/L and stored in the SSR will be discussed in section 8.3.2. It has been assumed that every P/L had its own processor, so they will not impact in the KIPS calculation. A representation of all the functions and the respective values for the sizing can be seen in Figure 29. The KIPS, data, code and typical frequency values were sourced from literature [47]. The acquisition frequency is usually the same as the typical frequency, but it may vary for certain S/S, as explained below.

ADCSS							OS														
Components	Nb	Code [words]	Data [words]	Typical KIPS	Typical freq [Hz]	Acquisition freq [Hz]	KIPS	Components	Nb	Code [words]	Data [words]	Typical KIPS	Typical freq [Hz]	Acquisition freq [Hz]	KIPS						
RW	4	1000	300	5	2	50	125	Complex autonomy	1	15000	10000	20	10	10	20						
Star cameras	2	2000	15000	2	0,01	1	200	Fault monitors	1	4000	1000	15	5	5	15						
IMU	1	800	500	9	10	10	9	Fault correction	1	2000	10000	5	5	5	5						
Digital sun sensors	6	500	100	1	1	1	1	Kalman filter	1	8000	1000	80	0,01	0,01	80						
Thruster Control	16	600	400	1,2	2	50	30	Executive	1	3500	2000	60	10	10	60						
Kinematic Integration	1	2000	200	15	10	1	1,5	Run time Kernel	1	8000	4000	60	10	10	60						
Error Determination	1	1000	100	12	10	1	1,2	I/O device handlers	1	2000	700	50	5	1	10						
Complex Ephemeris	1	3500	2500	4	0,5	1	8	Diagnostic and test	1	700	400	0,5	0,1	1	5						
Orbit Propagation	1	13000	4000	20	1	1	20	Math utilities	1	1200	200	0,5	0,1	1	5						
<hr/>																					
PS							EPS														
Components	Nb	Code [words]	Data [words]	Typical KIPS	Typical freq [Hz]	Acquisition freq [Hz]	KIPS	Components	Nb	Code [words]	Data [words]	Typical KIPS	Typical freq [Hz]	Acquisition freq [Hz]	KIPS						
645-N bipropellant thruster	1	1200	1500	5	0,1	0,1	5	Power voltage control	1	1200	500	5	1	0,1	0,5						
Tank control valve	10	800	1500	3	0,1	1	30	Power current control	1	1200	500	5	1	0,1	0,5						
Tank pressure sensor	10	800	1500	3	0,1	1	30	<hr/>													
<hr/>																					
TT&C							TCS														
Components	Nb	Code [words]	Data [words]	Typical KIPS	Typical freq [Hz]	Acquisition freq [Hz]	KIPS	Components	Nb	Code [words]	Data [words]	Typical KIPS	Typical freq [Hz]	Acquisition freq [Hz]	KIPS						
Transponders	2	1000	4000	7	10	10	7	Thermal control	1	800	1500	3	0,1	1	30						

**Figure 29:** Functions for every S/S.

The following assumptions have been made during the reverse sizing process:

- Attitude determination tasks for the ADCS were set to a frequency of 1 Hz, while attitude control tasks were set to 50 Hz, as indicated in literature [58]. The thrusters considered are only those used for attitude control, while the bipropellant engine is considered in the propulsion subsystem;
- In the PS, the specifications for the bipropellant thruster align with typical values for main engines. It is assumed that each of the 5 tanks (2 fuel tanks, 1 oxidizer tank, and 1 auxiliary tank) had redundant control valves and pressure sensors. The frequency of the valves and sensor has been increased due to the high number of thrusters on the S/C, necessitating frequent monitoring to minimize the risk of failures;
- For TCS, the frequency was increased to minimize the risk of failure as this S/S held critical importance for the mission.

Two modes were tested to determine the required processor and memory for the reverse sizing analysis. The first mode, referred to as the *Communication mode*, involved activating all S/S except for the PS. It was assumed that during communication operations, the bipropellant system would not be utilized, as it is primarily used for DSM and TCM rather than for small attitude adjustments. The second mode, known as the *Manouevring mode*, activated all the S/S except for the TTMT. Exploiting the results shown in Figure 30 and Table 40, it was determined that the *Maneuvering mode* placed the highest demand on the system, and thus it was considered for the sizing analysis. A safety margin of 400% was applied to ensure sufficient resources. The processor used on board was a RAD 6000, with its specification shown in Table 39 [7] [47]. For this processor, the word length is 32 bits. The reverse sizing results for both modes are shown in Table 40.

	<b>ADCS</b>	<b>EPS</b>	<b>PS</b>	<b>TCS</b>	<b>TT&amp;C</b>	<b>OS</b>	<b>TOT</b>
<b>Communication</b>	1	1	0	1	1	1	
throughput [KIPS]	1425,7	1	0	30	14	260	1730,7
<b>margined [KIPS]</b>	<b>7128,5</b>	<b>5</b>	<b>0</b>	<b>150</b>	<b>70</b>	<b>1300</b>	<b>8653,5</b>
Code [words]	79900	2400	0	800	2000	44400	<b>129500</b>
<b>margined [words]</b>	<b>399500</b>	<b>12000</b>	<b>0</b>	<b>4000</b>	<b>10000</b>	<b>222000</b>	<b>647500</b>
Data [words]	53200	1000	0	1500	8000	29300	<b>93000</b>
<b>margined [words]</b>	<b>266000</b>	<b>5000</b>	<b>0</b>	<b>7500</b>	<b>40000</b>	<b>146500</b>	<b>465000</b>
<b>Maneuvering</b>	1	1	1	1	0	1	1
throughput [KIPS]	1425,7	1	605	30	0	260	2321,7
<b>margined [KIPS]</b>	<b>7128,5</b>	<b>5</b>	<b>3025</b>	<b>150</b>	<b>0</b>	<b>1300</b>	<b>11608,5</b>
Code [words]	79900	2400	17200	800	0	44400	<b>144700</b>
<b>margined [words]</b>	<b>399500</b>	<b>12000</b>	<b>86000</b>	<b>4000</b>	<b>0</b>	<b>222000</b>	<b>723500</b>
Data [words]	53200	1000	31500	1500	0	29300	<b>116500</b>
<b>margined [words]</b>	<b>266000</b>	<b>5000</b>	<b>157500</b>	<b>7500</b>	<b>0</b>	<b>146500</b>	<b>582500</b>

**Figure 30:** Calculation of KIPS and words of memory needed by both analysed modes.

Freq. [Mhz]	RAM [Mb]	ROM [Mb]	MIPS
25	8	4	10 to 20

**Table 39:** RAD 6000 Specifications.

	RAM [Mb]	ROM [Mb]	MIPS
Communication	4.45	2.59	8.65
Manoeuvering	5.22	2.89	11.61

**Table 40:** Reverse sizing results for both modes.

The selection of the chosen processor is justified by the successful fulfillment of all imposed requirements through the reverse sizing process. Furthermore, the decision of this specific processor over other options is supported by its high radiation hardness (100 KRad) and long flight heritage [7]. The sizing analysis also considers the fault processor, which is responsible for handling a portion of the calculations delegated by the main processor during the mission. The latter has only 4 Mb of RAM and ROM, so it does not respect the RAM requirement. However, this discrepancy arises due to the high margins (400%) applied. In reality, the fault processor did only a small part of the calculations.

### 8.3.2 SSR sizing

The SSR sizing consists in calculating the memory capacity needed to store all the data generated by the P/L. An approximate estimation of the daily data production for each P/L has been used [59]. The outcomes of this analysis can be seen in Table 41.

Produced data [Mb]	Margined data [Mb]	Memory available [Gb]	Maximum accumulation [days]
9.17	45.85	1	22.33

**Table 41:** SSR reverse sizing.

The data presented in Table 41 represents the daily data produced by all the P/Ls. The "maximum accumulation" value indicates the number of days it would take to fill the memory completely without performing any downlinking. However, the data is retained for up to 40 days during the operation. The difference can be explained by a number of factors, including

the use of a 400% margin or the likelihood that the data created by the MDIS indicated in literature [59] does not account for image compression and merely shows the raw data produced.

## References

- [1] Peter D Bedini. Messenger mission overview. *SCIENCE*, 131, 2007.
- [2] George Dakermanji Carl S. Engelbrecht James C. Leary, Richard F. Conde. The messenger spacecraft. *Springer Science*, 2007.
- [3] J. Jenkins L. Kennedy D. Temkin G. Dakermanji, C. Person. The messenger spacecraft power system design and early mission performance. 2005.
- [4] Kimberly J. Ord and Kenneth E. Hibbard. Messenger power and thermal systems operations. 2010.
- [5] Eric J. Finnegan Michael V. Paul. Messenger - a highly constrained mission to the innermost planet. *The Johns Hopkins University Applied Physics Laboratory*, 2008.
- [6] Christopher J. Krupiarz M. Annette Mirantes J. Doug Reid David A. Artis, Brian K. Heggestad. Messenger: Flight software design for a deep space mission. *The Johns Hopkins University Applied Physics Laboratory*, 2007.
- [7] James C Leary, Richard F Conde, George Dakermanji, Carl S Engelbrecht, Carl J Ercol, Karl B Fielhauer, David G Grant, Theodore J Hartka, Tracy A Hill, Stephen E Jaskulek, et al. The messenger spacecraft. *The MESSENGER Mission to Mercury*, pages 187–217, 2007.
- [8] Mark E Holdridge et al. Launch and early operation of the messenger mission. *Space science reviews*, 2007.
- [9] Sean C Solomon et al. The messenger mission to mercury: Scientific objectives and implementation. *Planetary and Space Science*, 2001.
- [10] Scott M. Hull. End of mission considerations. 2013.
- [11] Sean C Solomon, Ralph L McNutt, et al. Messenger mission overview. *Space Science Reviews*, 131:3–39, 2007.
- [12] James V McAdams, David W Dunham, Robert W Farquhar, Anthony H Taylor, and BG Williams. Trajectory design and maneuver strategy for the messenger mission to mercury. *Journal of spacecraft and rockets*, 2006.
- [13] A. H. Taylor B. J. Williams J.V. McAdams, R. W. Farquhar. Messenger mission design and navigation. *Space science reviews*, 2007.
- [14] NASA. Messenger mission design. <https://messenger.jhuapl.edu/About/Mission-Design.html>.
- [15] C.T. Russell D.L Domingue. *The MESSENGER Mission to Mercury*. Springer, 2007.
- [16] ESA ESTEC. Margin philosophy for science assessment studies. *ESA UNCLASSIFIED*, 2012.
- [17] Howard D. Curtis. *Orbital mechanics for engineering students*. Butterworth-Heinemann, 2014.
- [18] Samuel Wiley, Katherine Dommer, and Larry Mosher. Design and development of the messenger propulsion system. In *39th AIAA/ASME/SAE/ASEE Joint Propulsion Conference and Exhibit*, page 5078, 2003.
- [19] Samuel Wiley, Katie Dommer, Carl Engelbrecht, and Robin Vaughan. Messenger propulsion system flight performance. In *42nd AIAA/ASME/SAE/ASEE Joint Propulsion Conference & Exhibit*, page 4689, 2006.
- [20] George P Sutton and Oscar Biblarz. *Rocket propulsion elements*. John Wiley & Sons, 2016.
- [21] Dipak K Srinivasan, Mark E Perry, Karl B Fielhauer, David E Smith, and Maria T Zuber. The radio frequency subsystem and radio science on the messenger mission. *Space Science Reviews*, 131:557–571, 2007.
- [22] Andrew G Santo, Robert E Gold, Ralph L McNutt Jr, Sean C Solomon, Carl J Ercol, Robert W Farquhar, Theodore J Hartka, Jason E Jenkins, James V McAdams, Larry E Mosher, et al. The messenger mission to mercury: spacecraft and mission design. *Planetary and Space Science*, 49(14-15):1481–1500, 2001.
- [23] Robert E Wallis and Sheng Cheng. Phased-array antenna system for the messenger deep space mission. In *2001 IEEE Aerospace Conference Proceedings (Cat. No. 01TH8542)*, volume 1, pages 1–41. IEEE, 2001.
- [24] Richard F. Conde George Dakermanji Carl J. Ercol Karl B. Fielhauer David G. Grant Theodore J. Hartka T. Adrian Hill Steven E. Jaskulek James V. McAdams M. Annette Mirantes David F. Persons Robin M. Vaughan, James C. Leary. Return to mercury: The messenger spacecraft and mission. 2006.
- [25] NASA. About the dsn [https://www.nasa.gov/directorates/heo/scan/services/networks/deep\\_space\\_network/about](https://www.nasa.gov/directorates/heo/scan/services/networks/deep_space_network/about).

- [26] Timothy Cornish. 34-m and 70-m command. 2014.
- [27] Electronic Communications Committee (ECC). The european table of frequency allocations and application in the frequency range: 8.3 khz to 3000 ghz (eca table). 2020.
- [28] Deep Space Network. 201 - frequency and channel assignments. 2014.
- [29] Airbus. X-band for mission critical communications <https://airbus-ds-gs.com/wp-content/uploads/2020/04/X-Band-brochure.pdf>.
- [30] K Andrews, V Stanton, S Dolinar, V Chen, J Berner, and F Pollara. Turbo-decoder implementation for the deep space network. *The Interplanetary Network Progress Report, IPN Progress Report*, pages 42–148, 2002.
- [31] Perry M Malouf and Robert E Wallis. The medium-gain antenna of the messenger spacecraft. *Microwave Journal*, 48(10), 2005.
- [32] Hongxing S. Shapiro David R. Haley Robin M. Vaughan, Daniel J. O’Shaughnessy. The messenger spacecraft guidance and control system.
- [33] Daniel J. O’Shaughnessy Robin M. Vaughan. Spacecraft pointing for science observations for messenger’s venus flyby 2 and mercury flyby 1.
- [34] Daniel J. O’Shaughnessy Sarah H. Flanigan, Robin M. Vaughan. Guidance and control of the messenger spacecraft in the mercury orbital environment.
- [35] Robin Vaughan Daniel O’Shaughnessy. Messenger spacecraft pointing options.
- [36] Sarah H. Flanigan Daniel J. O’Shaughnessy. Messenger spacecraft pointing performance during the mission’s mercury orbital phase.
- [37] Robin M Vaughan, David R Haley, Daniel J O’Shaughnessy, and Hongxing S Shapiro. Momentum management for the messenger mission. *Advances in the Astronautical Sciences*, 109:1139–1158, 2002.
- [38] Carl Ercol, George Dakermanji, and Binh Le. The messenger spacecraft power subsystem thermal design and early mission performance. In *4th International Energy Conversion Engineering Conference and Exhibit (IECEC)*, page 4144, 2006.
- [39] Carl J. Ercol G. Allan Holtzman, Shawn M. Begley. Return to mercury: An overview of the messenger spacecraft thermal environmental predictions and analysis process. *45th International Conference on Environmental Systems*, 2015.
- [40] George Dakermanji C. Jack Ercol and Binh Le. The messenger spacecraft power subsystem thermal design and early mission performance. *4th International Energy Conversion Engineering Conference and Exhibit (IECEC)*, 2006.
- [41] H. Gary Pippin. Analysis of silverized teflon thermal control material flown on the long duration exposure facility. *NASA Contractor Report 4663*, 1995.
- [42] Kimberly J. Ord and Kenneth E. Hibbard. Messenger power and thermal systems operations. *The Johns Hopkins University Applied Physics Laboratory*, 2010.
- [43] C. Jack Ercol. Return to mercury: An overview of the messenger spacecraft thermal control system design and up-to-date flight performance. *The Johns Hopkins University Applied Physics Laboratory, Laurel, MD 20723-6099*, 2008.
- [44] Shawn M. Begley C. Jack Ercol and G. Allan Holtzman. Return to mercury: An overview of the messenger spacecraft thermal control system design and update on orbital flight performance. *The Johns Hopkins University Applied Physics Laboratory, Laurel, TFAWS2012-PT-03*, 2008.
- [45] RalphL. McNutt Sean C. Solomonb Carl J. Ercola. Andrew G. Santoa, Robert E. Golda. The messenger mission to mercury: spacecraft and mission design. *Planetary and Space Science* 49, 2001.
- [46] David G Gilmore, David G Gilmore, and Martin Donabedian. *Spacecraft thermal control handbook*, volume 1. Aerospace Press El Segundo, CA, 2002.
- [47] Wiley J Larson, James Richard Wertz, et al. *Space mission analysis and design*, volume 3. Springer, 1992.
- [48] C. J. Ercol G. Dakermanji, J. Jenkins. The messenger spacecraft solar array design and early mission performance. 2006.
- [49] George Dakermanji C. Jack Ercol and Binh Le. The messenger spacecraft power subsystem thermal design and early mission performance. 2006.

- [50] Larry R. Kennedy George Dakermanji Binh Q. Le, Sharon X. Ling and Sean C. Laughery. The messenger power distribution unit packaging design. 2004.
- [51] Michael Buckley Donald Savage. Launch press kit - august. 2004.
- [52] Thomas Y. Yi James D. Dunlop, Gopalakrishna M. Rao. Nasa handbook for nickel-hydrogen batteries. 1993.
- [53] Robert E. Gold James C. Leary the MESSENGER Team Ralph L. McNutt Jr., Sean C. Solomon. The messenger mission to mercury: Development history and early mission status. *Advances in Space research*, 38:564—571, 2005.
- [54] Ralph L. McNutt Sean C. Solomon Carl J. Ercol Andrew G. Santo, Robert E. Gold et al. The messenger mission to mercury: spacecraft and mission design. *Planetary and Space Science*, 49:1481—1500, 2001.
- [55] Sharon X Ling, Richard F Conde, and Binh Q Le. A lightweight integrated electronics module (iem) packaging design for the messenger spacecraft. In *Proceedings. The 21st Digital Avionics Systems Conference*, volume 2, pages 9B4—9B4. IEEE, 2002.
- [56] Binh Q Le, Sharon X Ling, Larry R Kennedy, George Dakermanji, and Sean C Laughery. The messenger power distribution unit packaging design. In *Proceedings. The 21st Digital Avionics Systems Conference*, volume 2, pages 9B3—9B3. IEEE, 2002.
- [57] Andrew B. Calloway Constantine M. Frangos Brian K. Heggestad Douglas B. Holland William C. Stratton Christopher J. Krupiarz, David A. Artis. File-based data processing on messenger. *Acta Astronautica*, 59:1071–1078, 2005.
- [58] Robin M Vaughan, Daniel J O'Shaughnessy, Hongxing S Shapiro, and David R Haley. The messenger spacecraft guidance and control system. In *NASA 2005 Flight Mechanics Symposium*, pages 18–20, 2005.
- [59] Robert E Gold, Sean C Solomon, Ralph L McNutt Jr, Andrew G Santo, James B Abshire, Mario H Acuña, Robert S Afzal, Brian J Anderson, G Bruce Andrews, Peter D Bedini, et al. The messenger mission to mercury: scientific payload. *Planetary and Space Science*, 49(14-15):1467–1479, 2001.